Phil. Trans. R. Soc. Lond. A **321**, 277–303 (1987) [277]
Printed in Great Britain

THE EROSION AND DEFORMATION OF POLYETHYLENE BY SOLID-PARTICLE IMPACT

BY S. M. WALLEY AND J. E. FIELD
Physics and Chemistry of Solids, Cavendish Laboratory, Madingley Road, Cambridge CB3 0HE, U.K.

(*Communicated by D. Tabor, F.R.S. – Received* 16 *September* 1985)

[Plates 1–14]

CONTENTS

In recent years, polyethylene (PE) has found increasing use in applications involving impact and erosion. This paper describes a detailed study of the properties of PE subjected to solid particle impact. Flat discs of the material were eroded by sieved sand (300–600 μm) accelerated by using an air blast rig in which the important variables of velocity, angle and mass flux rate are accurately controllable and

measurable. Scanning electron microscopy of lightly eroded specimens enabled four basic crater types to be identified: smooth, ploughed, cut, and dented. The proportions of each were established over a range of angles. Long time erosion experiments were conducted in which the flux rate for each angle was adjusted to keep the number of impacts per unit time constant. The dimensionless erosion parameter, ϵ (mass lost per unit mass of erodent that has struck) was computed by using the rate of mass loss when steady-state erosion had been established. Most erosion was found to occur at an angle of 20–30°, the mass loss becoming zero at around 80°. An analysis by D. R. Andrews is presented, showing that the flux rates used in these experiments are well below those needed to cause wear by thermal mechanisms, and this was confirmed by changing the flux rate: mass loss increased in proportion. Macroscopic particles were used to model sand grain impacts, spheres for rounded particles and square plates for sharp ones. A range of techniques was used in this study including high-speed photography (framing speed of 5×10^4 s^{-1}), scanning electron microscopy, and moiré methods (both in-plane and out-of-plane). A deformation map was constructed for steel sphere impacts giving the type of crater to be expected at a given angle and speed. It was observed that sand grains required much lower speeds at a given angle to produce a given crater type. High-speed photography enabled mass-loss mechanisms for single-particle impact to be identified. These were the drawing-out of filaments and the machining-out of chips. Quantitative data on kinetic energy losses were obtained, and these, combined with moiré methods that gave the sizes of deformed zones, enabled an estimate of the temperature rise per impact to be made (25 K).

1. Introduction

The erosion of bulk organic polymers by solid-particle impact has received little attention compared to metals and ceramics (Schmitt 1980), but their increasing use in pipelines carrying gases, liquids, and solids in suspension makes it important to study their erosion properties (Bragaw 1979; Meldt 1982).

Two main types of erosion behaviour have been identified (Finnie *et al.* 1967), depending on whether wear is greatest at angles of impingement around 20–30° (ductile metals) or 90° (brittle solids). The sort of behaviour a system exhibits at a given temperature may depend on the particle size (Sheldon & Finnie 1966) and on the particle shape (Cousens & Hutchings 1983). Tilly (1969*a*, *b*) found that nylon and polypropylene (PP) showed ductile behaviour, but recent work by Söderberg *et al.* (1981) has shown that certain polymers such as polymethylmethacrylate (PMMA) erode like inorganic glasses. The work reported here shows that polyethylene (PE) belongs to the ductile class, although with important differences from metals.

The motive for this research stemmed from the use of PE piping in gas distribution pipes and fittings in the U.K. and elsewhere (Benjamin 1980). The research reported here was part of wider background studies of PE material properties and aimed to investigate the susceptibility of PE material to erosion damage by particles of iron oxide and sand in the engineering environment. For example, these particles may occur in parts of the old gas distribution network, which was constructed from grey cast iron, as a result of the production of town gas. At present, the usual operating gas velocities are below that necessary for particle entrainment and the possibility of migration and erosion damage. However, in addition to gas distribution, PE piping is increasingly being used for water supply, drainage systems, and a variety of other industrial applications when fluids, slurries, or particulate matter are transported (Meldt 1982). Our research makes it possible to assess the flow conditions that could be tolerated before erosion became important.

Two methods of study were chosen. The first was the standard technique of using small flat specimens and determining how the dimensionless erosion parameter, ϵ (mass of material removed per unit mass of erodent that has struck) varies with the angle, α, and speed of attack v_i (note that in erosion, α is defined so that normal impact is 90°). Some work was also performed on the effect of the flux rate, ϕ (mass of erodent striking unit area in unit time). The second method was the study of single impacts, making extensive use of high-speed photography and scanning electron microscopy (SEM) to identify damage mechanisms (for their use with metals see for example, Hutchings *et al.* 1976; Timothy & Hutchings, 1981; Andrews & Field 1982*a*, *b*; Hutchings 1982).

2. Experimental

(*a*) *Multiple-particle erosion apparatus*

The investigation of ϵ was carried out by using a multiparticle erosion apparatus of the sand-blast type (figure 1; see also Andrews *et al.* 1983).

The essential features of the rig relevant to this work are as follows. (*a*) The flux rate, ϕ, of erodent is accurately controllable up to a value of 25 kg m^{-2} s^{-1} by means of an electrically driven grooved turntable. (*b*) The particle speed can be altered by changing the gas pressure applied to the sand hopper and to the start of the acceleration barrel. The velocity range that can be covered by using a tube 25 mm (1 in) in diameter, 4 m in length is *ca.* 5–40 m s^{-1}, and this has been found to be independent of ϕ. (*c*) Up to 250 kg of erodent can be stored in the hopper, allowing experiments of several hours duration to be performed. (*d*) Specimens with a diameter of 12 mm can be positioned accurately in angled holders close to the end of the barrel. Still photographs showed that under these conditions the angular spread at the specimen position was no more than 5° at 5 mm from the beam axis (Andrews & Horsfield 1983). (*e*) Those parts of the particle injection system where the flow of gas and sand has to be turned through an angle are made of soft, polymeric tubes. This means that virtually no comminution of the erodent occurs, i.e. the particle-size distribution at the target is the same as that put into the hopper. Typical lifetimes for these tubes under the most severe wear conditions achievable with the rig are 3–4 h. This then is the practical upper limit to our continuous erosion experiments. (*f*) The specimen chamber has windows for viewing and photography. Air and sand are extracted from it as fast as they arrive by means of a powerful pump.

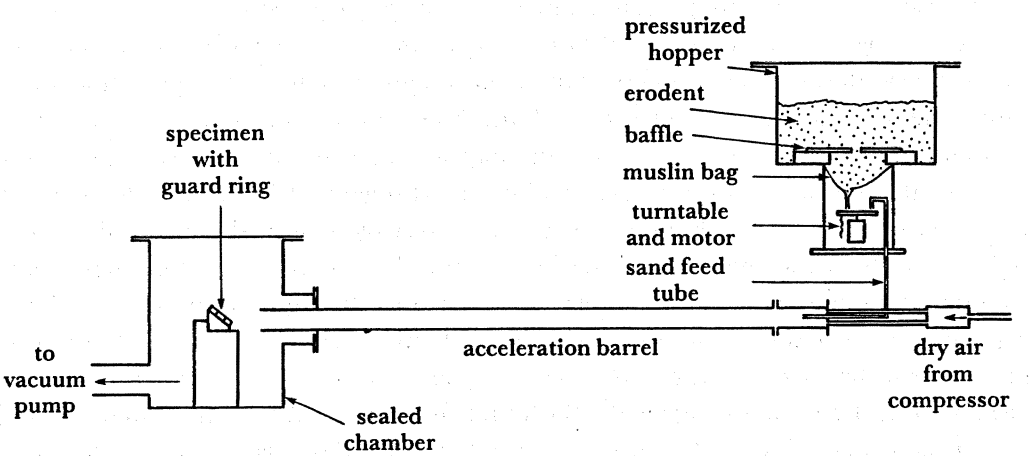

FIGURE 1. Schematic diagram of the multiparticle erosion apparatus (not to scale).

(*b*) *Single-particle impact*

Macroscopic single particles were projected at specimens by using laboratory gas-guns. Spherical particles were fired from a cylindrical (Hutchings & Winter 1975) and square plates from a rectangular bore gun (Hutchings *et al.* 1977). A schematic diagram of the system, showing ancillary equipment for measuring particle speed and for performing high-speed photography is given in figure 2.

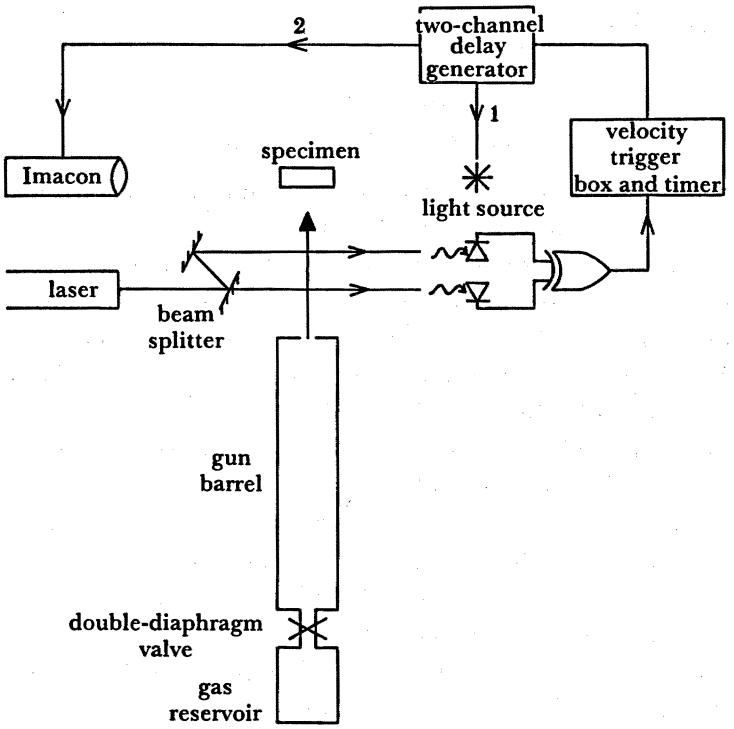

FIGURE 2. Schematic diagram of the single-particle erosion apparatus (not to scale).

Projectiles are carried down the barrel by using a sabot, which is accelerated by the expansion of gas from the reservoir through a valve. The speed attainable depends upon three factors. (*a*) It increases with reservoir pressure, but (*b*) for a given pressure, helium gives a higher speed than nitrogen (Hutchings & Winter 1975), and (*c*) a valve with an opening time commensurate with the acceleration time in the barrel gives a lower final speed than one whose opening time is much less (Andrews 1983*a*). Solenoid valves (opening times of a few milliseconds) are useful up to *ca.* 100 m s^{-1}, but for speeds greater than this (up to *ca.* 360 m s^{-1}) bursting metal foils are used in a double-diaphragm arrangement (Hutchings & Winter 1975).

At the end of the barrel, the sabot is brought to rest by a stop, the projectile carrying on through a hole to strike the target. The impact speed is measured in free flight using two photodiodes illuminated by a split laser beam passing through the gun axis. High-speed photographic sequences were obtained with a Hadland Image Converter Camera (Imacon). Because the gun firing speed varies by a few percent from shot to shot for a given pressure, and because it is desirable to trigger the flash and the camera at the time when the projectile is entering the field of view, P. H. Pope (of this laboratory) designed an electronic system that

uses velocity and position information to set the trigger pulse. By using this device, the photographic success rate was raised from *ca.* 30% (using position information only) to *ca.* 90% (Walley 1983).

(*c*) *Properties of* PE

The PE used in this study is gas-pipe grade material. It is required by the British Gas Corporation (BGC) to meet their standard BGC/PS/PL2. This specifies that it shall have (*a*) a medium to high density; (*b*) a yellow pigment uniformly dispersed within it (for identification purposes); (*c*) a yield strength of 14–15 MPa (if medium density) or 18–19 MPa (if high density); (*d*) an ultimate elongation of 350–500%; and (*e*) an induction temperature for decomposition greater than 500 K. This material was supplied to us by the BGC in the form of hot-pressed sheets 5 mm thick. We measured the mechanical and thermal properties thought to be relevant to erosion, and these are set out in table 1.

TABLE 1. MEASURED MECHANICAL AND THERMAL PROPERTIES OF THE PE

property	value	comments
density	940 kg m^{-3}	MDPE range
compressive uniaxial yield stresses, σ_y, and strains, ϵ_y, at various strain rates ($\dot{\epsilon}$)	σ_y = 15–17.5 MPa ϵ_y = 0.05–0.12	$\dot{\epsilon} \approx 10^{-3}$ s^{-1} achieved in an Instron mechanical testing machine
	σ_y = 37 MPa ϵ_y = 0.16	$\dot{\epsilon} \approx 10^{+2}$ s^{-1} achieved in a drop-weight machine (see, for example, Swallowe & Field 1982)
	σ_y = 45 MPa ϵ_y = not deducible	$\dot{\epsilon} \approx 10^{+4}$ s^{-1} achieved in a direct Impact Kolsky bar (see, for example, Gorham 1979)
specific heat	2.5 J g^{-1} K^{-1} 3.6 J g^{-1} K^{-1}	T = 300 K, T = 375 K, measured on a Perkin Elmer differential scanning calorimeter (DSC)
latent heat of fusion	180±10 J g^{-1}	measured on a Mettler DSC 30
bulk melting temperature	395 K	
crystallinity	62±2%	taking the latent heat of fusion of 100% crystalline PE as 290 J g^{-1} (Gaur & Wunderlich 1981)
number average molecular mass $\overline{M}_n$	23000	measured at RAPRA (U.K.) by using gel permeation chromatography (GPC)
mass average molecular mass $\overline{M}_w$	153000	

(*d*) *Erodent for multiparticle erosion studies*

Quartz sand sieved into the linear size range 300–600 μm was obtained from the David Ball Company. Its average two-dimensional roundness R was measured as being about 0.5 (Andrews 1980), where R is a dimensionless quantity and is defined for a single particle as

$$R = \sum_{i=1}^{N} r_i / N R_I, \tag{1}$$

where the r_i are the radii of the corners, N the number of corners, and R_I the radius of the largest inscribable circle. Since their linear size spans a factor of 2, their mass range varies over an order of magnitude. However, their mean mass was found to be 190 μg, calculated from the mass of about 100 grains.

3. Results of multi-particle erosion experiments

(*a*) *Scanning electron microscope study*

PE specimens were exposed for about 1 s at various angles to a very low flux of the erodent at 36 ± 6 m s^{-1}. This gave surfaces with very few overlapping impact sites, enabling statistics on the crater sizes and types to be compiled. These measurements were performed by using a Cambridge Stereoscan 250 mark II SEM after first depositing an aluminium film on the specimens from a hot filament under vacuum. It was found that the craters could be classified into four types: (*a*) smooth; (*b*) ploughed; (*c*) cut; (*d*) sharply dented. Inevitably some craters were difficult to classify unambiguously, but clear examples of the four types are given in figure 3, plate 1.

It can be seen from table 2 that the proportion of impacts that involve substantial material displacement (ploughing and cutting) is high at low angles (particularly 20° and 30°). So on the basis of the model of ductile polymer erosion proposed by Engel *et al.* (1981), that involves the formation of loops of polymer and their snagging by subsequently impacting particles, we would expect most erosion to occur around 20–30°. Even so, it can be seen that a small fraction of impacts at high angles ($> 60°$) produce this type of deformation. It should be noted that considerable care was taken to ensure that only sand that was accelerated down the barrel struck the specimens. This was achieved by thoroughly extracting the sand from the chamber between each run. Some craters had their projected areas measured by printing electron micrographs, cutting out the crater shapes, and weighing them. The values obtained are given in table 3. It can be seen that crater sizes do not vary significantly above an angle of impact of 40°. Note also the large variation in area for a given angle due to the random orientation of the irregularly shaped grains on impact and their size distribution.

(*b*) *Long-time erosion*

The form of erosion versus angle curve was determined by using the 300–600 μm sieved sand at a speed of impact of 36 ± 6 m s^{-1}. The flux rate, ϕ, for each angle was set so that the average number of impacts per unit time per unit area was the same. Explicitly

$$\phi_2/\phi_1 = \sin\alpha_1/\sin\alpha_2, \tag{2}$$

where $\phi_{1,2}$ is the flux rate (kg m^{-2} s^{-1}) at angle $\alpha_{1,2}$. This was done so as to be able to separate the angular dependence of erosion from the flux rate dependence, For these experiments, the mass flow resolved normal to the specimen surface was set at 3.5 ± 0.05 kg m^{-2} s^{-1}

Mass loss was determined by weighing the specimen at the beginning and end of a run. The alternative, and experimentally quicker, method of cumulatively eroding single samples (taking them out, weighing them and putting them back) was tried at low speeds (figure 4). The two techniques were found to be consistent within experimental error at intermediate speeds (28 ± 4 m s^{-1}) but gave different results at a lower speed (20 ± 3 m s^{-1}). Because it was thought possible that the interruption of bombardment for the period necessary to perform weighing

TABLE 2. PERCENTAGE OF CRATER TYPES FOR VARIOUS ANGLES OF IMPINGEMENT

angle/deg	smooth	ploughed	cut	sharply dented	total examined
10	45	30	11	14	222
20	28	43	22	7	129
30	42	40	5	13	222
40	62	21	4	13	232
50	68	14	5	13	229
60	80	7	4	9	313
70	90	6	0	4	260
80	86	3	1	10	120
90	90	5	0	5	132

TABLE 3. CRATER SIZES

angle/deg	number measured	mean μm^2	standard deviation μm^2	smallest μm^2	largest μm^2
10	14	6800	5600	1200	21000
20	10	16000	7800	8600	32000
30	13	15500	5400	9800	28000
40	17	17000	6000	7000	34000
50	16	23500	13000	8900	60000
60	20	29500	14000	11500	71000
70	12	23000	7900	9100	33000
80	12	22000	8900	10500	41000
90	11	32500	15000	6100	53000

(*ca.* 10 min) might allow the surface to recover viscoelastically, and hence perhaps change its susceptibility to erosion, the quicker method was not adopted.

A stainless-steel guard ring was used to protect the specimen sides, but because the specimens were prepared by using a punch, the top circumferential edge was curved. It was noted that the portion of this edge facing into the flow when the angle of impingement was low showed mass deposition, which is characteristic of high-angle erosion. However, the area affected was less than 4% of the total (Greenaway 1982) and hence not significant.

Figure 5 presents the curves of mass loss against time for 12 mm diameter PE specimens. The weighing balance used is accurate to 50 μg, so the error in each point (2 weighings) is 0.1 mg. Note that the time needed for mass loss to start (the incubation time) is large, particularly at high angles. The mass-loss rate never became positive for $\alpha = 80°$, even after three hours of bombardment, although the rate of mass gain kept decreasing. It is implausible that sand grains could go on piling up on the surface for ever. What almost certainly happens is that the process saturates.

It should be emphasized that the mass-change values plotted are the difference between the net mass of sand deposited and the mass of polymer lost. It is conceivable that PE is lost before the mass-loss rate becomes steady, and that saturation would be a dynamic equilibrium. Note also that the linear part of the curve of mass loss against time often extends below the time axis implying that steady-state erosion is established before the specimens' masses have decreased (positive mass loss). Thus there are two possible definitions of the incubation time: the first is the time for the mass-loss rate to become linear, the second is the time for the mass loss to return to zero. We chose the second definition because our data for low values of α were

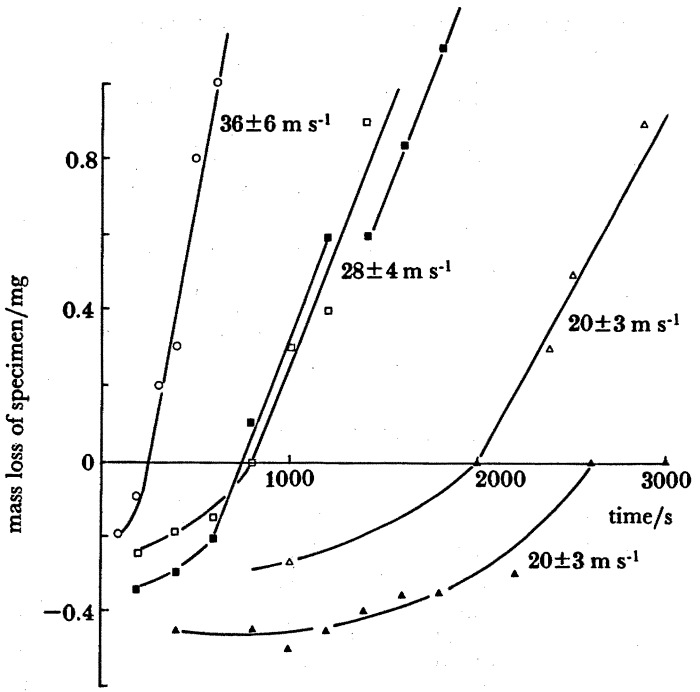

FIGURE 4. Graph of mass loss against time for 12 mm diameter PE specimens eroded at 30° for various impact speeds and at a flux rate normal to the specimen surface of 3.5 kg m^{-2} s^{-1}. The solid symbols give the mass loss for specimens eroded in a 'stop start' manner, i.e. eroded, taken out and weighed, put back and eroded again. The open symbols are the mass losses of *different* specimens eroded for the given times. Mass gains due to embedment of erodent are represented here (and in figure 5) as negative mass losses.

not accurate enough at short times to use the first definition. Mass gains were accompanied by darkening of the surface as small particles of sand became embedded. The maximum size of the embedded particles was measured as 50 μm, i.e. smaller than the original grains. It is not known whether comminution occurred on impact or by subsequent impacts. Typical steady-state eroded surfaces are shown in figure 6, plate 2.

In calculating ϵ for each angle, it was decided to ignore the mass of erodent that struck the specimens before the steady state was attained. This is because incubation times are a substantial proportion of the experimental time but a minute fraction of the service lifetime of a component made from PE. Thus it was felt that the only meaningful definition of $\epsilon(\alpha)$ enabling its values to be valid for long times (assuming no change in mechanism occurs) is

$$\epsilon(\alpha) = \dot{m}(\alpha)/A\phi(\alpha), \tag{3}$$

where $\dot{m}(\alpha)$ is the steady-state mass-loss rate at a given angle, $\phi(\alpha)$ the sand-flux rate (adjusted to keep the mass impacting the surface per unit time the same for all angles), and A the specimen surface area. By using this definition, the curve of figure 7 was constructed from the data of figure 5.

DESCRIPTION OF PLATE 1

FIGURE 3. Examples of single-impact sites formed by 300–600 μm sieved sand travelling at 36±6 m s^{-1}. The scale bars represent 40 μm. (*a*) Smooth crater, $\alpha = 20°$ from right to left. (*b*) Ploughed crater, $\alpha = 40°$ from left to right. (*c*) Cut craters, $\alpha = 20°$ from right to left. (*d*) Sharp dent, $\alpha = 40°$ from left to right. Potential: 20 kV in all cases.

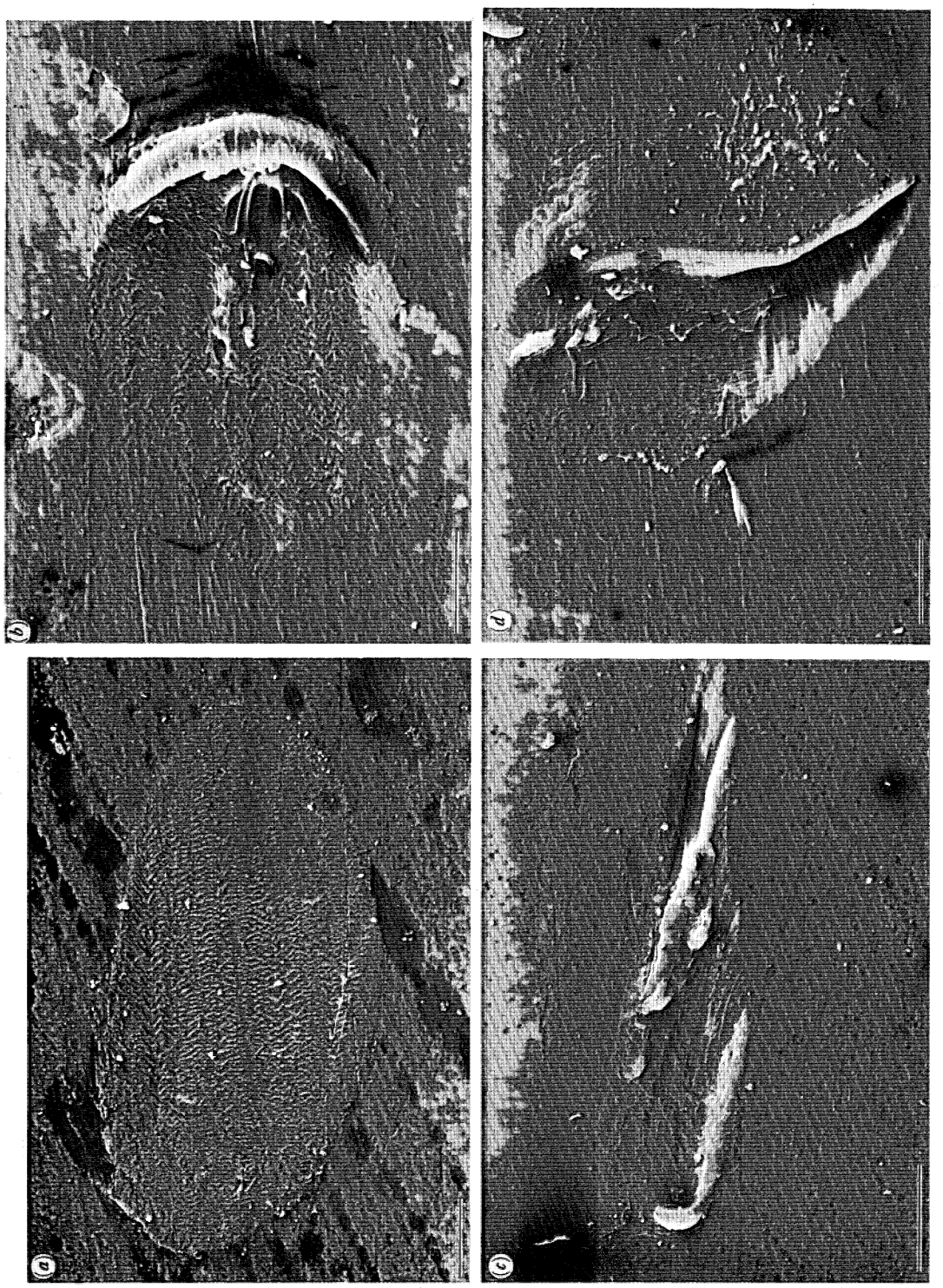

FIGURE 3. For description see opposite.

(*Facing p.* 284)

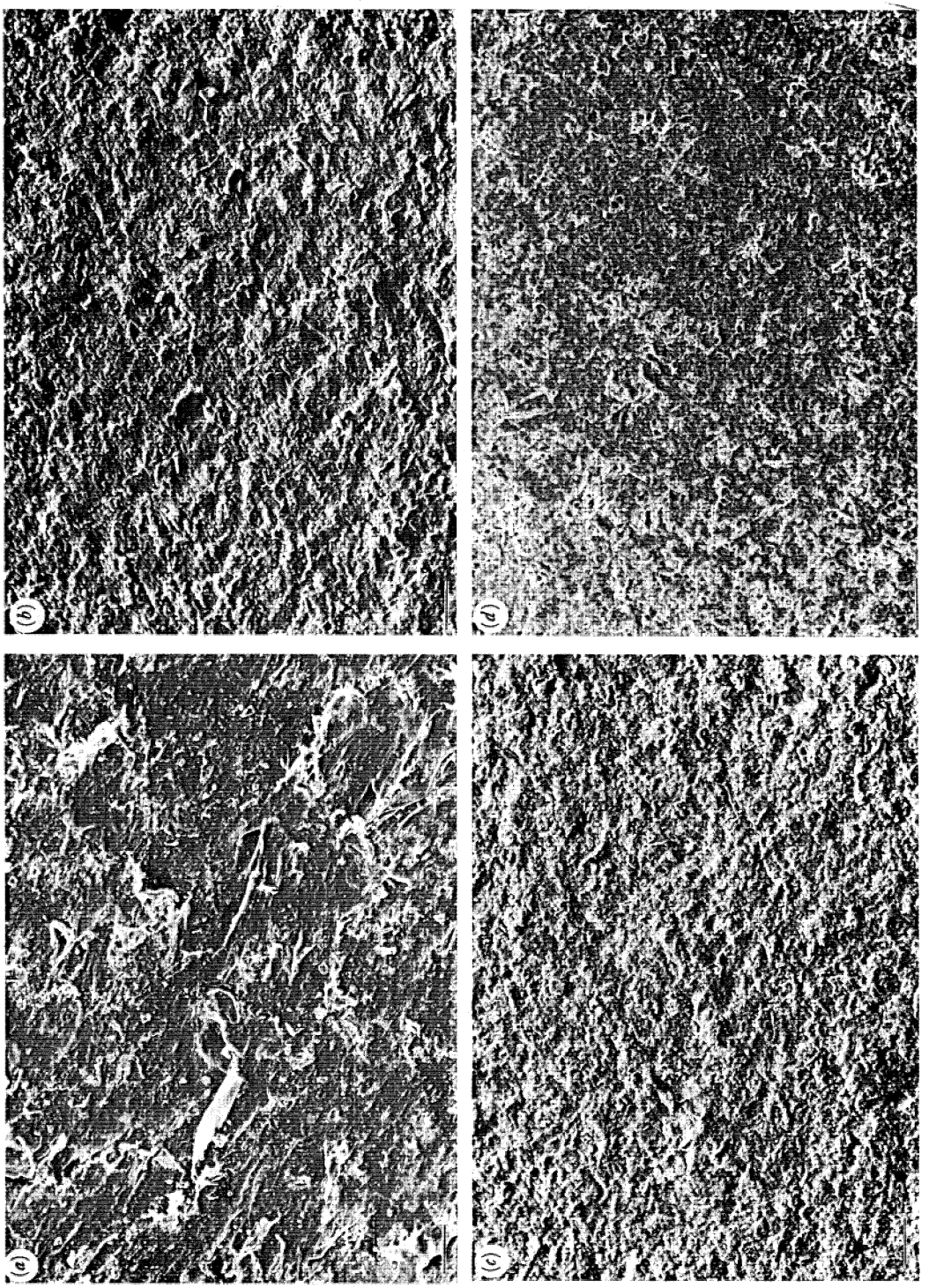

FIGURE 6. For description see opposite.

Description of plate 2

Figure 6. Electron micrographs of steady-state erosion surfaces produced by 300–600 μm sand at 36 ± 6 m s^{-1}. (*a*) $\alpha = 20°$, $t = 400$ s, scale bar represents 100 μm. (*b*) $\alpha = 40°$, $t = 700$ s, scale bar represents 200 μm. (*c*) $\alpha = 40°$, $t = 2000$ s, scale bar represents 200 μm. (*d*) $\alpha = 80°$, $t = 3000$ s, scale bar represents 100 μm. Potential: 20 kV in all cases.

Description of plates 3 and 4

Figure 9. Examples of the types of craters mapped in figure 8. The pictures are electron micrographs unless otherwise stated. Diameters refer to the spheres. (*a*) Smooth. 2 mm diameter, impact from right to left: $v_i = 150$ m s^{-1}, $\alpha = 15°$. (*b*) Banded. 2 mm diameter, impact from right to left: $v_i = 260$ m s^{-1}, $\alpha = 10°$. (*c*) Banded. 2 mm diameter, 10 kV, impact from right to left: $v_i = 190$ m s^{-1}, $\alpha = 15°$. Note the impression of the bands on the material indicating relaxation has occurred. (*d*) Intermediate between banded and lipped. 8 mm diameter, impact from left to right: $v_i = 190$ m s^{-1}, $\alpha = 23°$. Optical picture. (*e*) Lipped crater. 4 mm diameter, impact from left to right: $v_i = 150$ m s^{-1}, $\alpha = 27°$. Optical picture. (*f*) Penetration. 4 mm diameter, impact from left to right: $v_i = 180$ m s^{-1}, $\alpha = 70°$. Optical picture. (*g*) Embedment. 4 mm diameter, 20 kV, impact from left to right: $v_i = 288$ m s^{-1}, $\alpha = 35°$. (See also figure 14.) (*h*) Embedment. 2 mm diameter, 20 kV, impact from left to right: $v_i = 260$ m s^{-1}, $\alpha = 70°$.

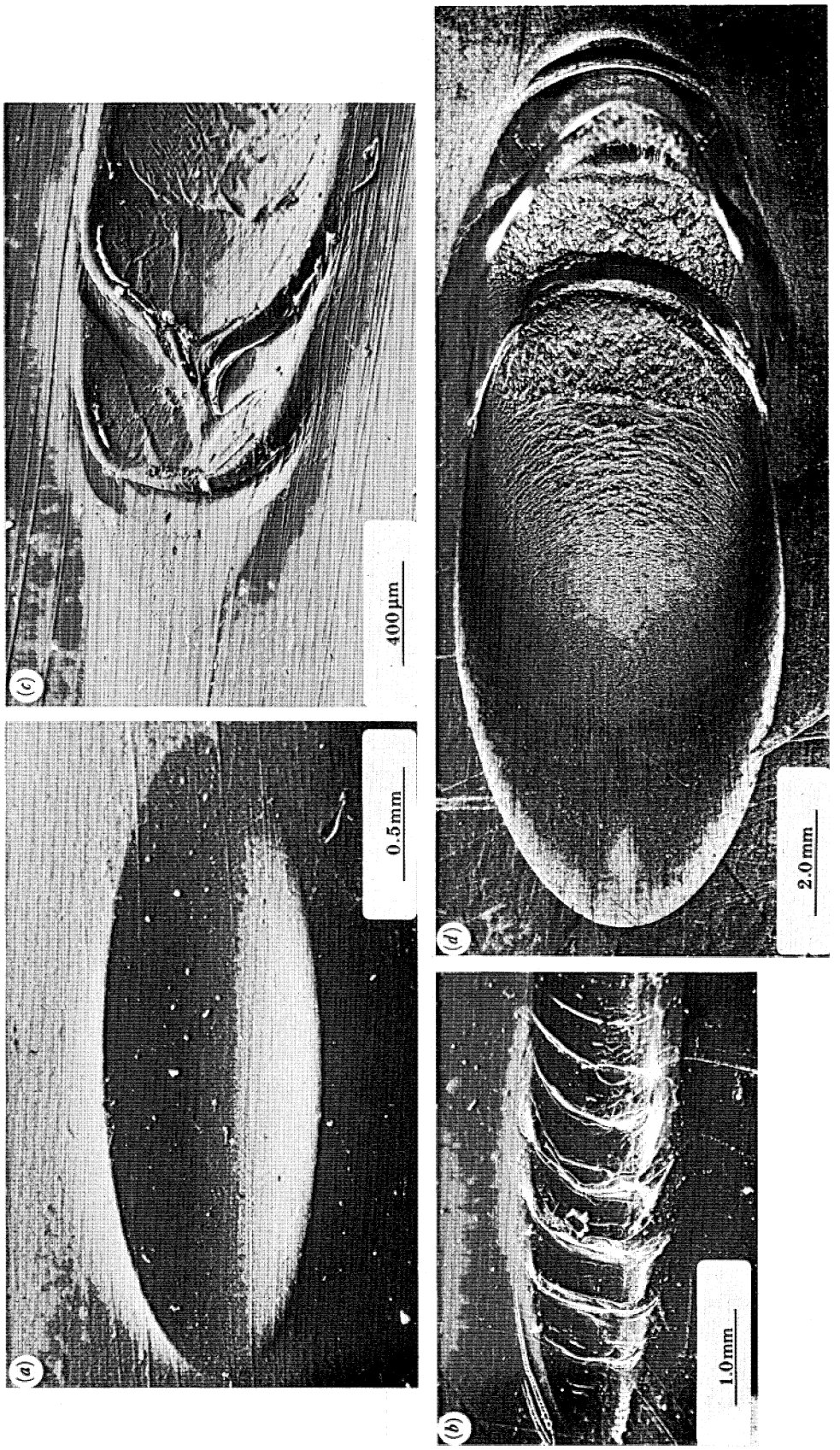

FIGURE 9*a–d*. For description see opposite plate 2.

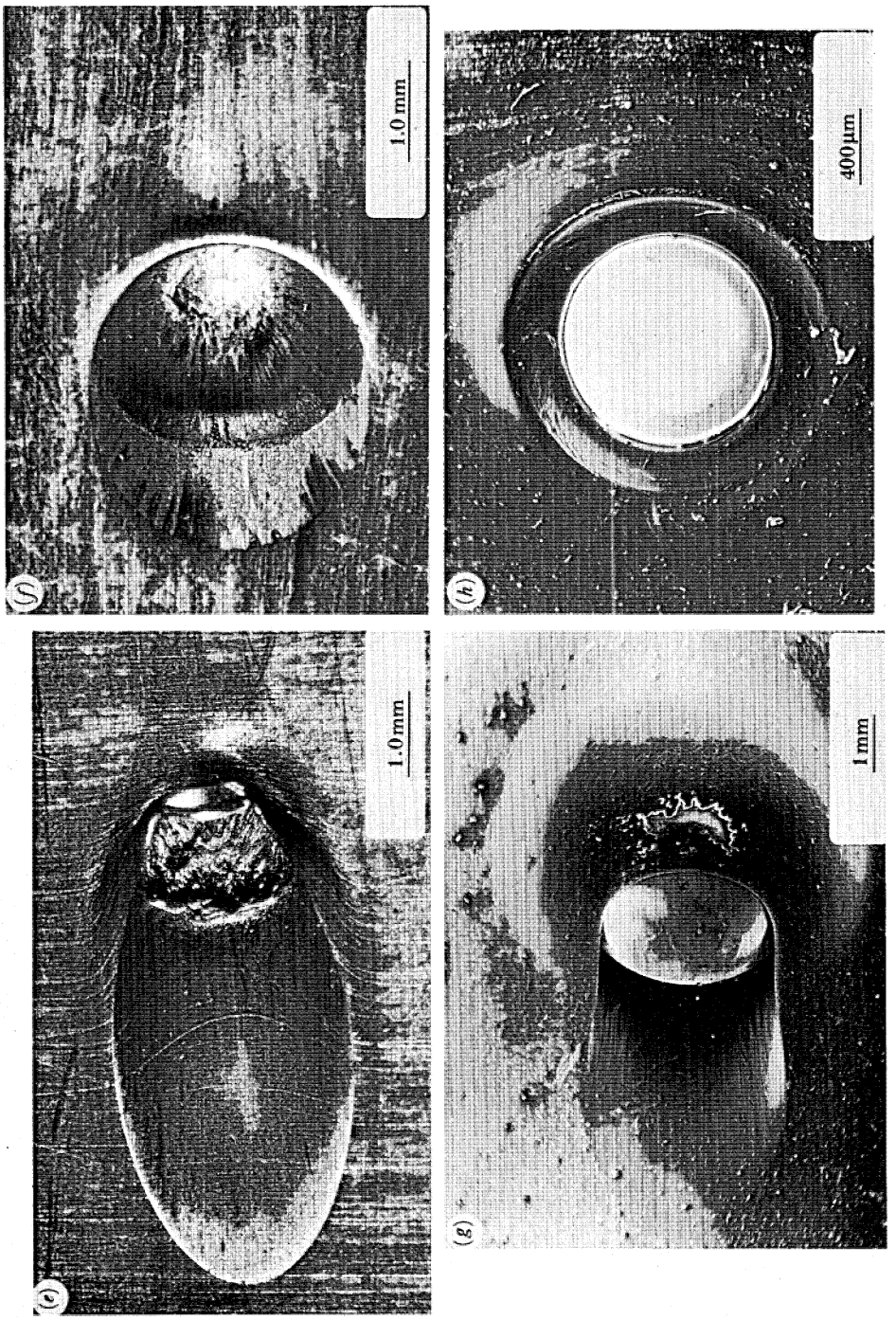

FIGURE 9*e–h*. For description see opposite plate 2.

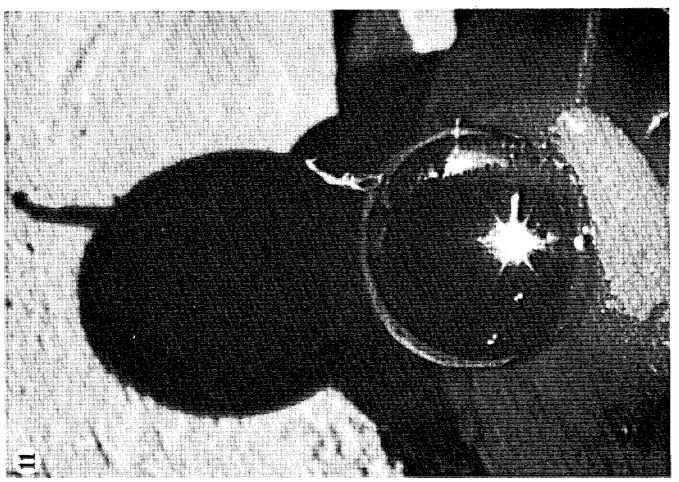

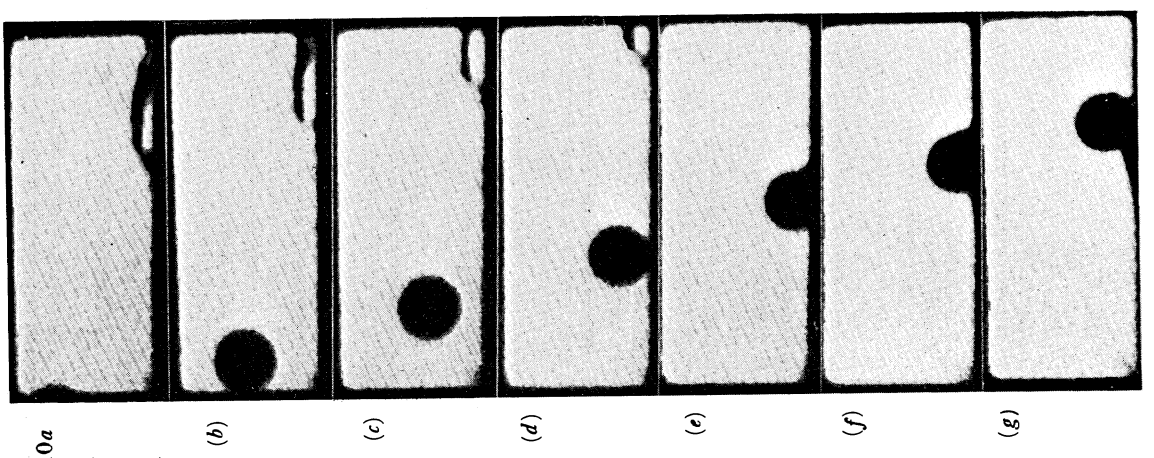

FIGURES 10 AND 11. For description see opposite.

DESCRIPTION OF PLATE 5

FIGURE 10. Frames (*a*)–(*l*), impact and rebound of a 4 mm diameter steel sphere that draws out a single filament. Interframe time: 19 μs. $v_i = 192$ m s^{-1}, $\alpha = 25°$; $v_r = 114$ m s^{-1}, $\beta = 27°$. Frames (*m*)–(*n*), last two frames of an impact that drew out two filaments. Interframe time: 17 μs. Sphere diameter: 5 mm. $v_i = 170 \pm 15$ m s^{-1}, $\alpha = 37°$; $v_r = 63 \pm 3$ m s^{-1}, $\beta = 47.5°$.

FIGURE 11. Optical picture of a filament that remained attached to a sphere after impact (ball diameter 5 mm). A shadow of the ball and filament appears in the background. $v_i = 170 \pm 15$ m s^{-1}, $\alpha = 36° \pm 4°$; $v_r = 64$ m s^{-1}, $\beta = 40°$.

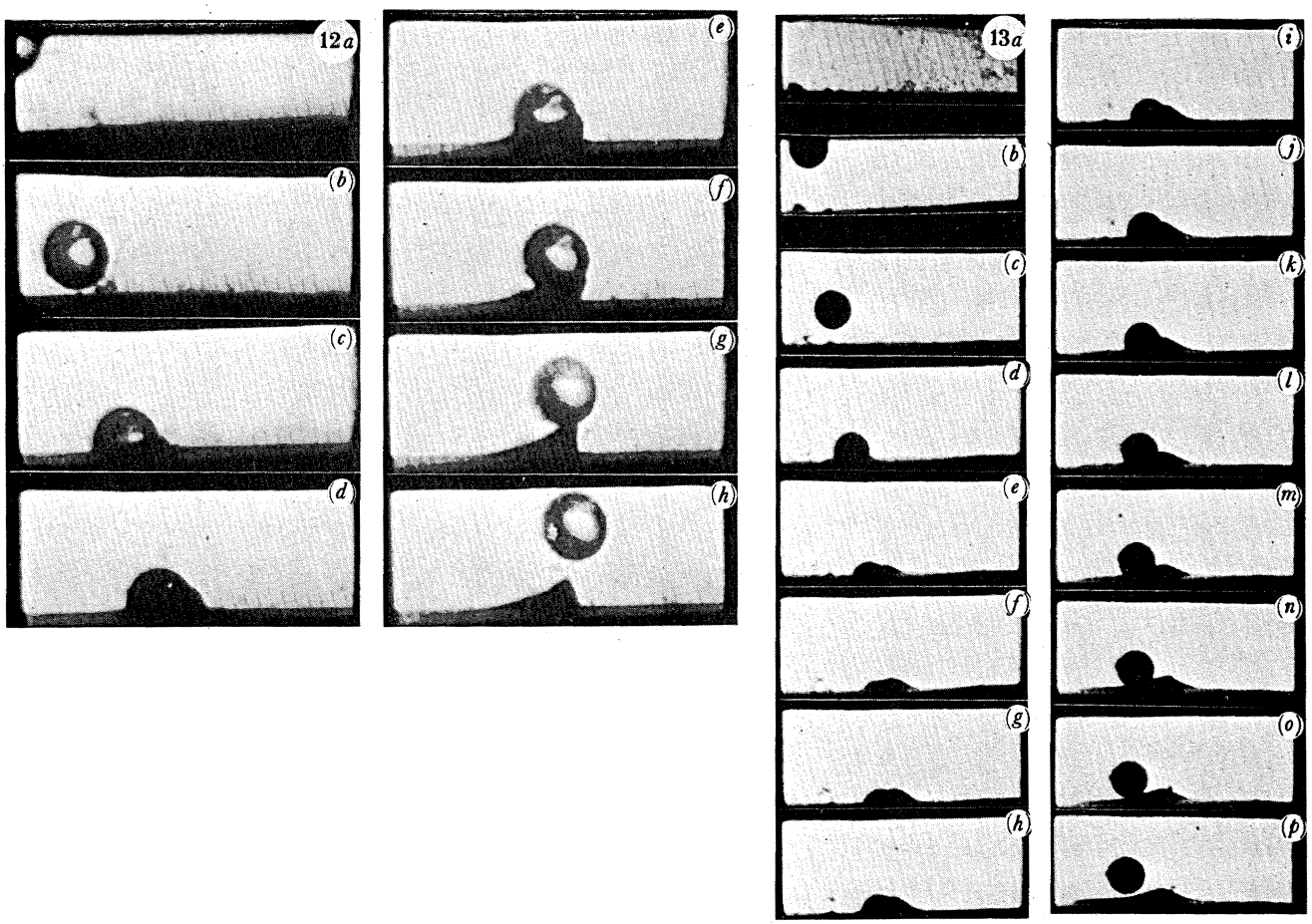

FIGURE 12. Impact and rebound of a 5 mm-diameter glass sphere. Note the rapid spring back of the lip material between frames (*e*) and (*g*). Interframe time: 17 μs. $v_i = 280$ m s^{-1}, $\alpha = 30°$; $v_r = 100 \pm 3$ m s^{-1}, $\beta = 54° \pm 2°$.

FIGURE 13. Penetrative impact by a 4 mm diameter steel sphere. Note that the ball comes out backwards. Interframe time: 17 μs. $v_i = 203 \pm 10$ m s^{-1}, $\alpha = 51.5° \pm 0.5°$; $v_r = 24$ m s^{-1}, $\beta = 135°$.

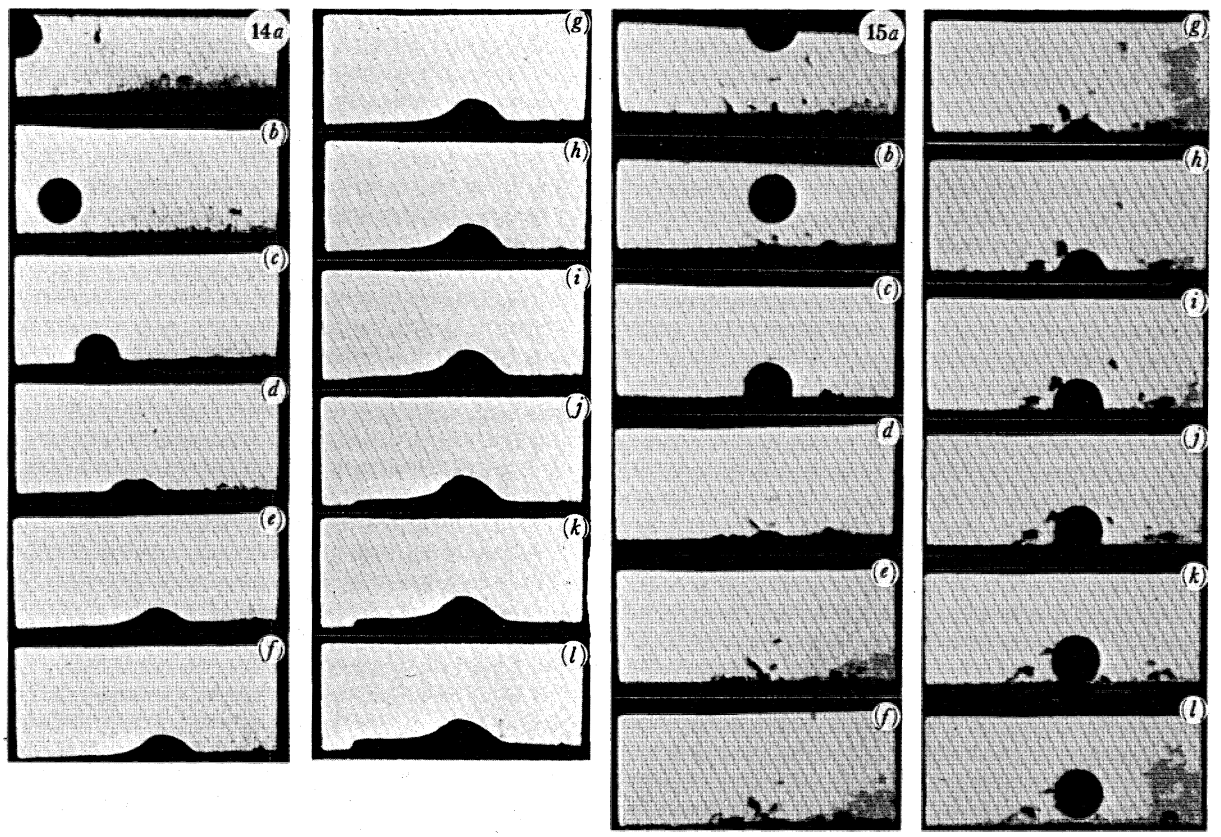

FIGURE 14. Example of embedment by a 4 mm diameter steel sphere. Interframe time: 17 μs. See also figure 9*g*. $v_i = 288$ m s^{-1}, $\alpha = 35°$.

FIGURE 15. Normal impact by a 4 mm diameter steel sphere where the ball rebounds even after entering to a depth greater than its diameter. Interframe time: 17 μs. 10 mm thick specimen. $v_i = 194$ m s^{-1}, $v_r = 45$ m s^{-1}.

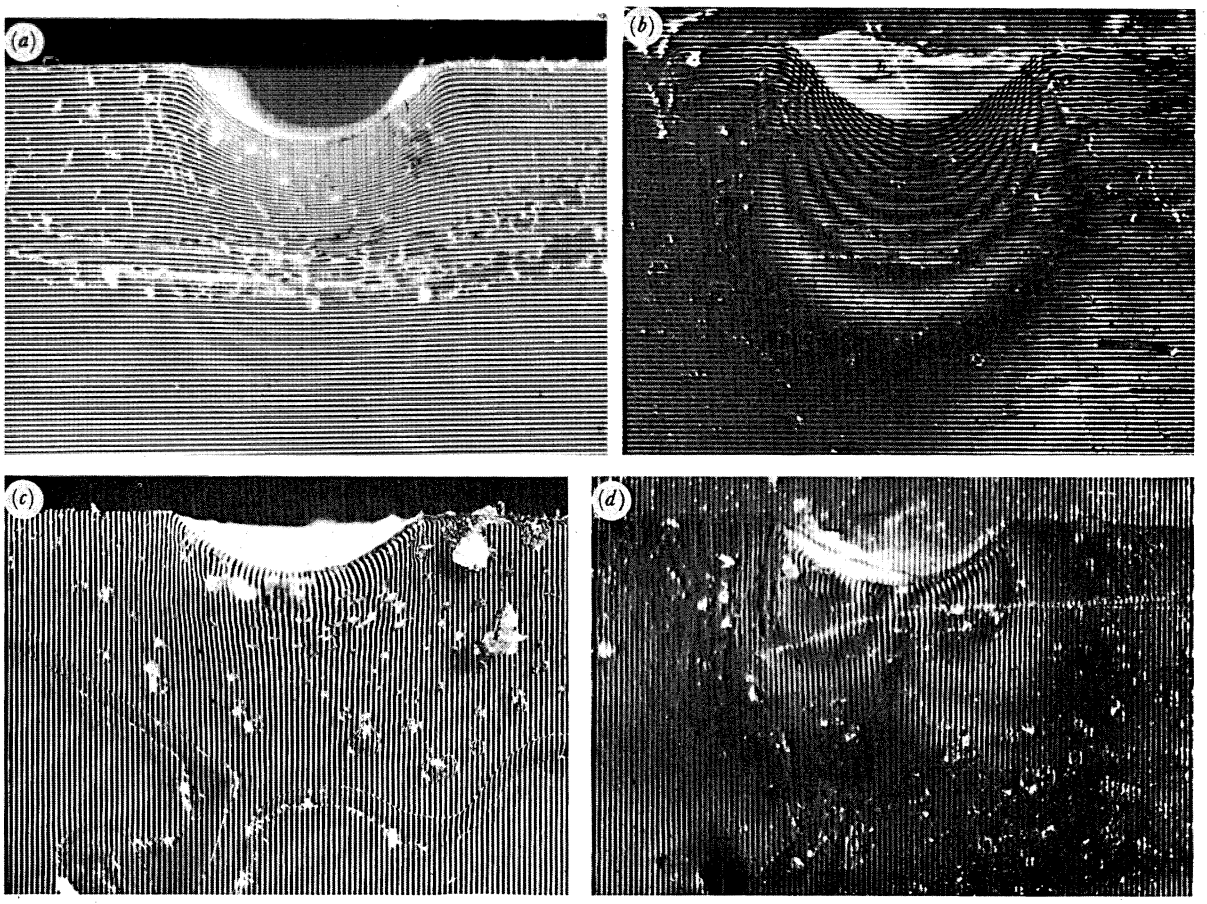

FIGURE 25*a–d*. For description see opposite.

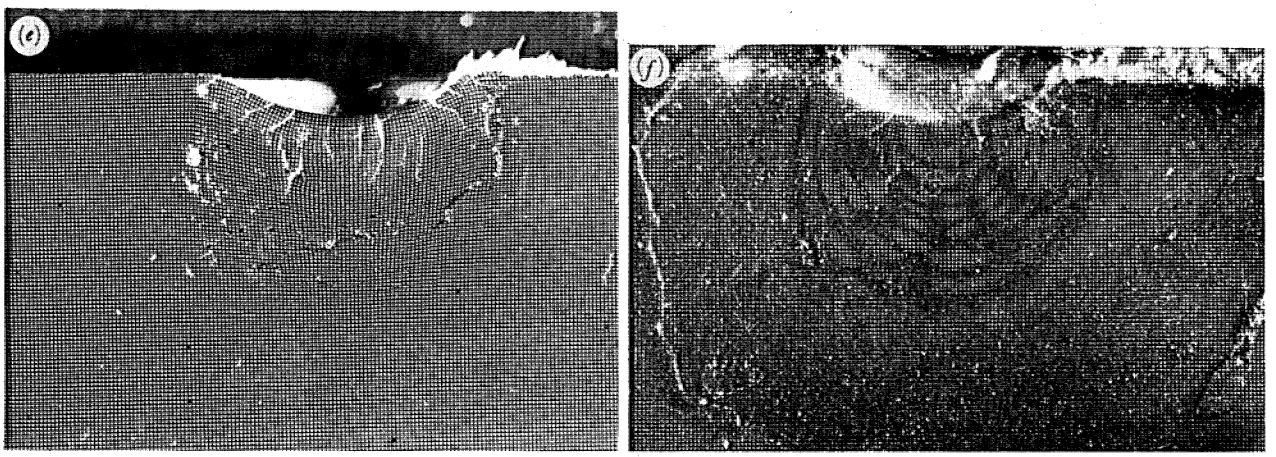

FIGURE 25. (*a*) Deformed horizontal line grating beneath an indentation by a 4 mm diameter sphere. Line spacing: 85 μm. (*b*) Moiré fringes formed by laying a reference grating on top of the specimen shown in (*a*). (*c*) Deformed vertical line grating beneath another indentation by a 4 mm diameter sphere. (*d*) Moiré fringes formed from (*c*) with a reference grating. (*e*) Deformed 2D grating beneath a 6 mm diameter steel sphere impact; $v_i = 124 \pm 4$ m s^{-1}, $v_r = 32$ m s^{-1}; kinetic energy dissipated: 6.3 J. (*f*) Two-dimensional displacement pattern formed from the specimen of (*e*) with a crossed reference grating.

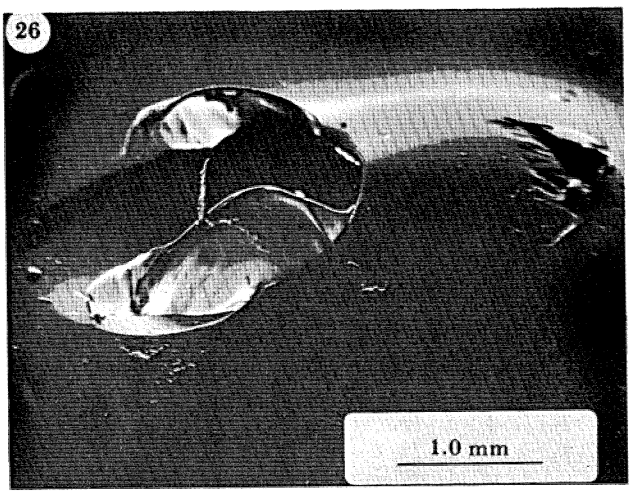

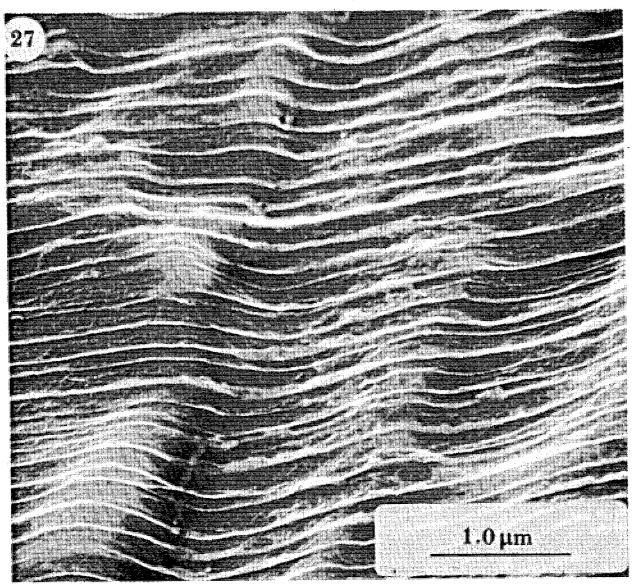

FIGURE 26. Possible example of melting caused by the impact of a 2 mm-diameter steel sphere from left to right. Ball embedded but fell out before the electron micrograph was taken; $v_i = 240$ m s^{-1}, $\alpha = 40°$.

FIGURE 27. Electron micrograph of the highly sheared surface from near the crater exit of a 2 mm-diameter steel sphere impact site; $v_i = 110$ m s^{-1}, $\alpha = 25°$.

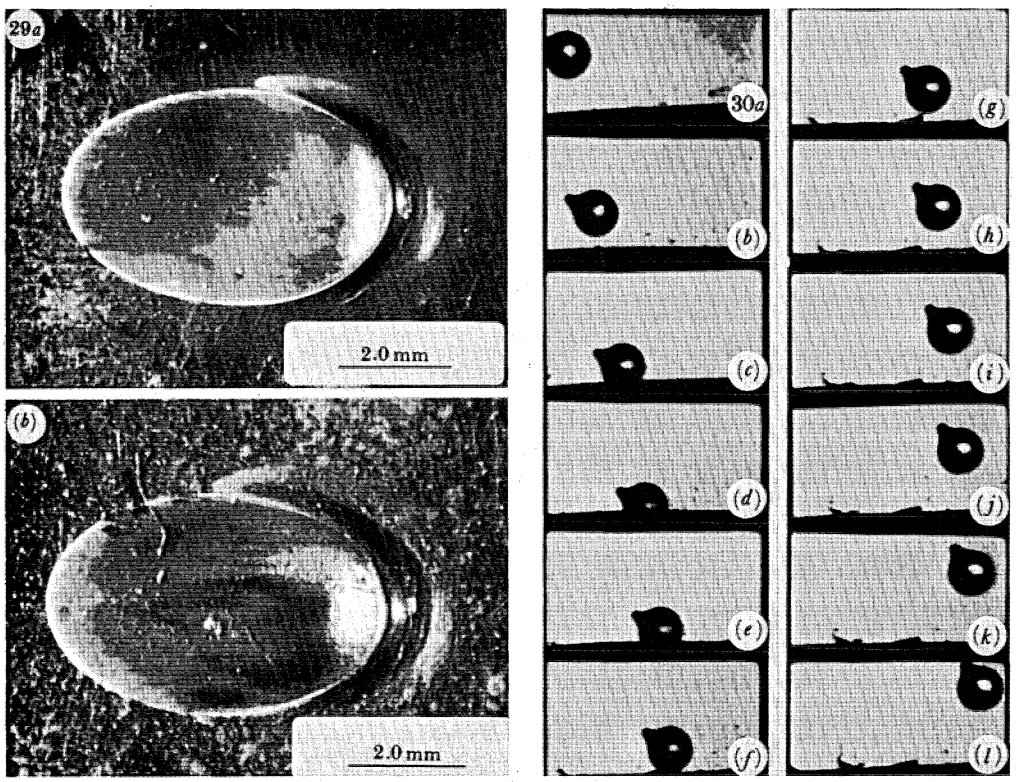

FIGURE 29. Optical pictures comparing oblique impact craters formed by 5 mm steel and glass spheres with similar kinetic energies. (*a*) Steel: $v_i = 128 \pm 7$ m s^{-1}, $\alpha = 39.5°$; $v_r = 62$ m s^{-1}, $\beta = 34°$; $E_{Ki} = 4.17$ J; $E_{Kr} = 0.98$ J; $\Delta E_K = 3.19$ J. (*b*) Glass: $v_i = 222$ m s^{-1}, $\alpha = 39°$; $v_r = 105 \pm 8$ m s^{-1}, $\beta = 43 \pm 4°$; $E_{Ki} = 4.24$ J; $E_{Kr} = 0.95$ J; $\Delta E_K = 3.29$ J.

FIGURE 30. High-speed photographic sequence showing rotation imparted to a tagged glass sphere. Interframe time: 17 μs. Rotation imparted: 3° per 17 μs (3.1 krad s^{-1}). $v_i = 238 \pm 7$ m s^{-1}, $\alpha = 38 \pm 1°$; $v_r = 102 \pm 2$ m s^{-1}, $\beta = 42 \pm 1°$.

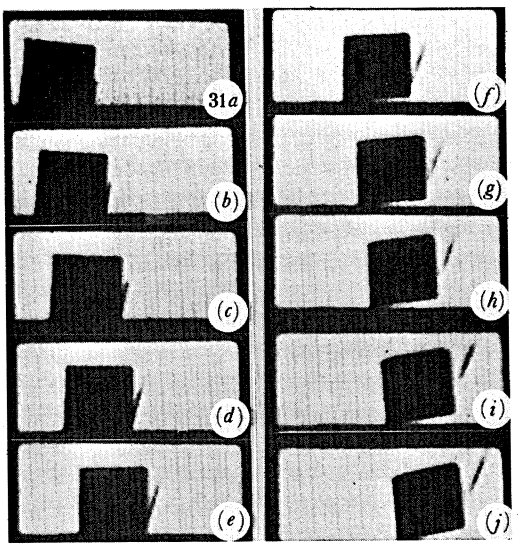

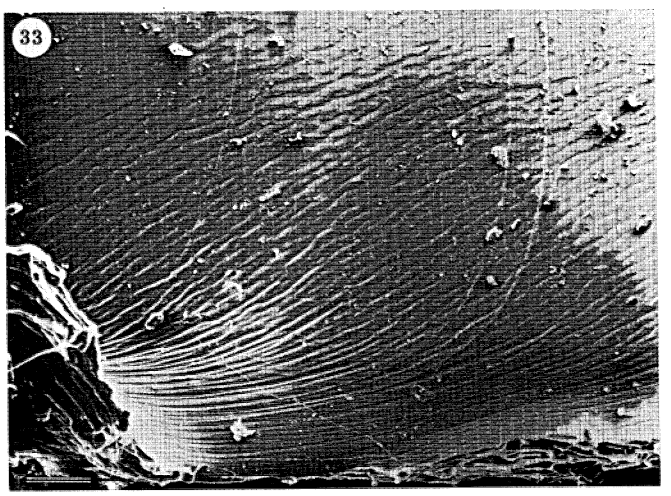

FIGURE 31. High-speed photographic sequence showing back rotation of an 8 mm-square steel plate and a chip of PE being cut off. Interframe time: 19 μs. $v_i = 89$ m s^{-1}, $\alpha = 10°$, $-\gamma = -8°$; $v_r = 72$ m s^{-1}, $\beta = 7°$, $\omega = -1.8$ krad s^{-1}.

FIGURE 33. Electron micrograph of shear bands at the base of the lip of figure 32*b*. Scale bar represents 100 μm. Potential: 20 kV.

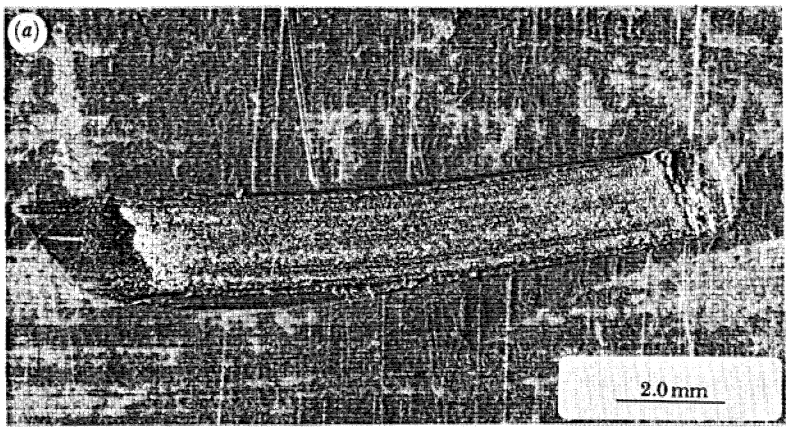

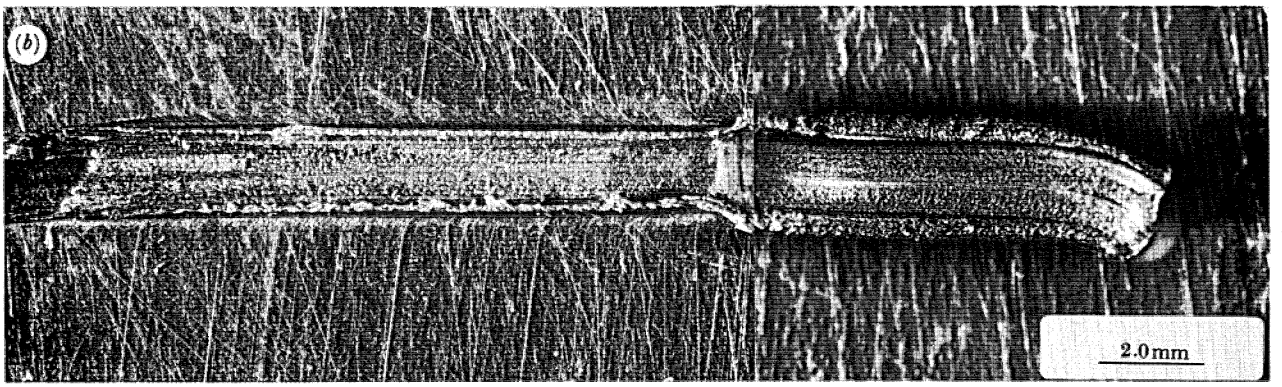

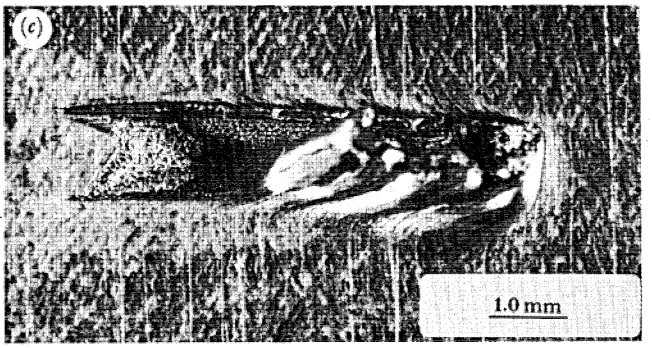

FIGURE 32*a–c*. For description see overleaf.

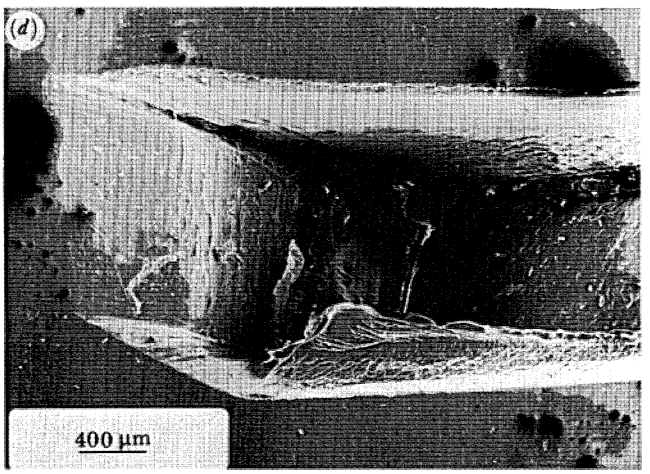

Description of plates 13 and 14

Figure 32. (*a*) Optical picture of the damage produced by the impact shown in figure 31. Plate moved from left to right. (*b*) Optical picture of an impact site where the plate rotated in a forwards sense; $v_i = 86$ m s^{-1}, $\alpha = 10°$, $-\gamma = -14°$. (*c*) Optical picture of a cutting-type crater. $v_i = 86$ m s^{-1}, $\alpha = 14°$, $-\gamma = -84°$; $v_r = 66$ m s^{-1}, $\beta = 14°$, $\omega = 2.3$ krad s^{-1}. (*d*) Scanning electron micrograph of a sharp dent. Potential: 20 kV. $v_i = 72$ m s^{-1}, $\alpha = 32°$, $-\gamma = -33°$; $v_r = 59$ m s^{-1}, $\beta = 21°$, $\omega = 6.4$ krad s^{-1}.

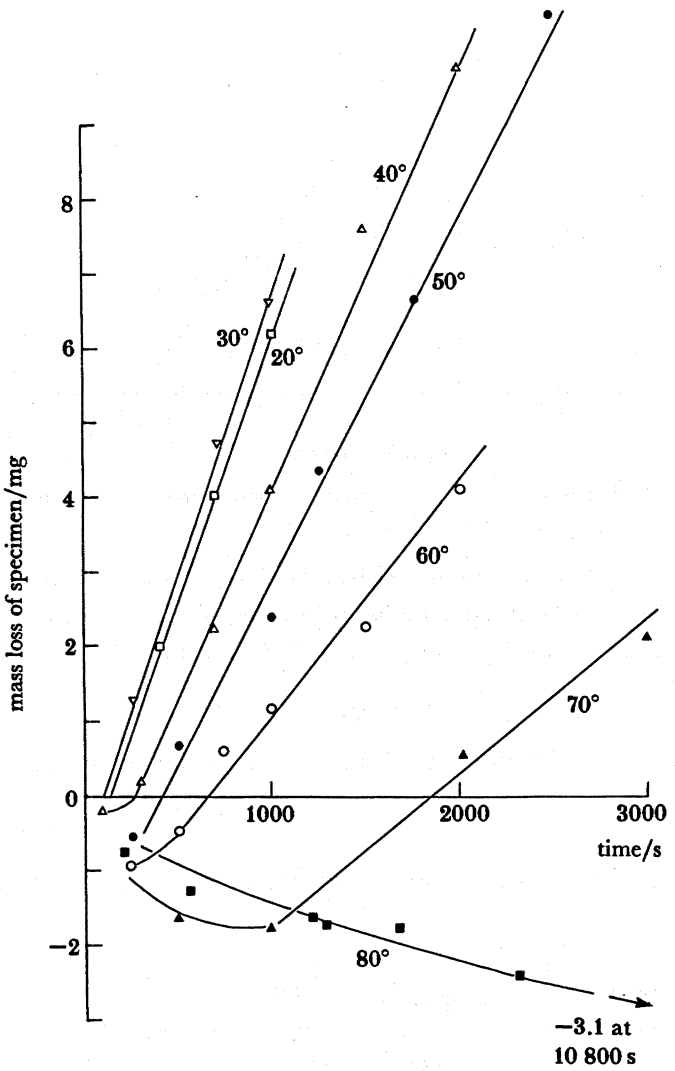

FIGURE 5. Graph of mass loss against time for 12 mm-diameter specimens eroded at various angles of impact. Speed of impact: 36 ± 6 m s^{-1}. Flux rate normal to the specimen surface: 3.5 ± 0.05 kg m^{-2} s^{-1}.

We have drawn a broken line for $\alpha < 20°$ because we do not know how it should approach zero. The erosion of our specimens should ideally be zero at $\alpha = 0°$, since although wear can undoubtedly occur when loose sand lying against a surface is caused to slide by fluid motion, the area presented to the sand stream in our rig will be zero, and hence (ideally) no impacts will occur. In reality, of course, edge effects, beam spreading and rogue particles will cause mass changes.

At the other end of the graph, we have shown erosion going to zero somewhere between 70° and 80°. This is consistent with the fact that we did not observe a positive mass-loss rate for $\alpha = 80°$. It could be argued, however, that although the scatter of points about the descending part of the curve does not allow one to discern an upward turn of slope such as would give a residual amount of erosion at normal impact, nevertheless the data do not rule out this possibility. This point could be checked by performing high-angle erosion at a higher flux rate than used here.

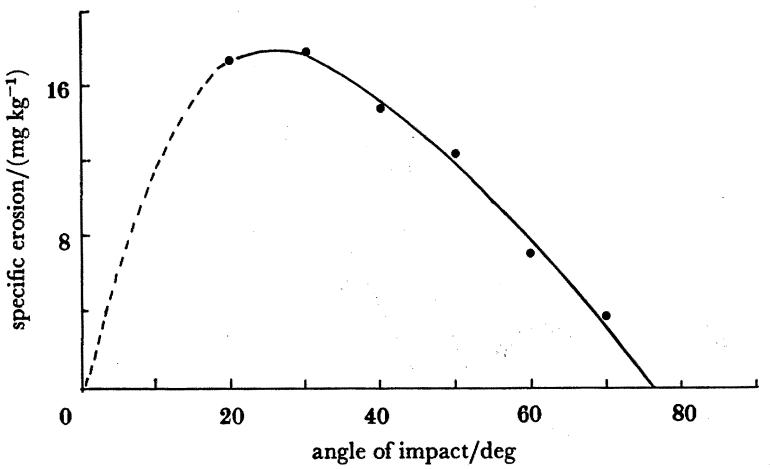

FIGURE 7. Graph of the dimensionless erosion parameter ϵ against impact angle (data of figure 5).

An average thinning rate can be calculated from the erosion parameter, ϵ. To do this, we assume that all the mass lost from the specimens consists of polymer and that it is lost uniformly over the surface (see the micrographs in figure 6). Then the thinning rate $\dot{T}$ is given by:

$$\dot{T} = \dot{m}/\rho A, \tag{4}$$

where ρ is the density of PE. All the macroscopic data for steady state erosion are set out numerically in table 4.

TABLE 4. EROSION DATA FOR PE FROM 300–600 μM SIEVED SAND AT A SPEED OF 36 ± 6 m s^{-1}

angle/deg	flux rate normal to the specimen surface / kg m^{-2} s^{-1}	incubation time, t_i/s	mass-loss rate / μg s^{-1}	ϵ / mg kg^{-1}	thinning rate / μm h^{-1}
20	3.5	120	7.0±0.1	17.4±0.2	240
30	3.5	90	7.3±0.2	18.1±0.3	250
40	3.4	285	5.8±0.3	15.0±0.7	200
50	3.55	430	5.0±0.2	12.4±0.2	175
60	3.5	610	2.8±0.3	7.2±0.2	100
70	3.5	1630	1.6	3.9	55
80	3.2	∞(?)	0(?)	0(?)	0(?)

(*c*) *Steady-state erosion on the microscopic scale*

An important variable in the analysis of erosion mechanisms is the 'impact zone frequency', Ω (Andrews 1981). This is the average impact frequency of erodent particles within an area equal to the average crater size, σ, assuming the area affected is not altered by the presence of embedded sand. If the mean particle mass is m_0, the number of impacts occurring on unit area of the surface per unit time is ϕ/m_0. Thus

$$\Omega = \phi\sigma/m_0. \tag{5}$$

From this expression, the 'incubation number' can be obtained. This is defined here as the number of impacts that have to occur on an impact zone before it contributes a net mass loss,

and it is therefore equal to Ωt_i, where t_i is the incubation time. Also, knowing the specimen impact frequency, ϕ/m_0, and the mass-loss rate, $\dot{m}$, the average loss of mass per impact, m_c, and the 'erosive efficiency', m_c/m_0, can be calculated (see table 5).

Several features can be seen from this table. First, the expected time between impacts on a given spot is a few seconds at the flux rates used. Secondly, the incubation numbers are large, suggesting that the amount of deformational damage needed before a wear particle is formed is also large. The value for the average loss of mass per impact (ng) does not rule out the possibility that each impact removes polymer (this mass of PE is a particle whose linear dimensions are *ca.* 10 μm). The alternative, of course, is that several impacts are required per wear particle, whose average size then would be bigger, but unless some means is found for recovering such tiny pieces of PE from several kilograms of used sand, this cannot be checked directly.

TABLE 5. MICROSCOPIC EROSION VARIABLES DEDUCIBLE FROM THE MASS-LOSS DATA

angle, α/deg	frequency of impact on the specimen surface, $(\phi A/m_0)/s^{-1}$	impact zone frequency, Ω/s^{-1}	incubation number, Ωt_i	average loss of mass per impact, m_c/ng	erosive efficiency, m_c/m_0
20	2200	0.31	37	3.2	1.7×10^{-5}
30	2200	0.30	27	3.3	1.7×10^{-5}
40	2100	0.31	88	2.8	1.5×10^{-5}
50	2200	0.45	194	2.3	1.2×10^{-5}
60	2150	0.55	336	1.3	0.7×10^{-5}
70	2150	0.43	700	0.7	0.4×10^{-5}
80	1950	0.37	∞ (?)	0(?)	0(?)

The question arises as to whether thermal effects play any part in the erosion of this material. It may well be thought to be likely since each impact causes plastic deformation, most of the energy dissipated ending up as heat (Taylor & Quinney 1934). Because PE has a low thermal conductivity, if the particles arrive fast enough, thermal energy will build up in the surface faster than it can move away by conduction, radiation and forced convection. If this thermal build-up did occur, it would be expected that ϵ would not be linearly related to ϕ. There are two possible competing processes: (*a*) heat builds up to such an extent that melting occurs (Andrews 1981), i.e. another erosion mechanism comes into play additional to the mechanical ones; (*b*) the elevated temperature facilitates stress relaxation, thus tending to reduce the mechanical damage inflicted by a given quantity of erodent.

We investigated the effect of flux rate at $\alpha = 40°$ and at impact speeds of 36 ± 6 m s^{-1}. The angle 40° was chosen because the erosion was close to the maximum but also the flux rate used at this angle was close to one quarter of the maximum possible with our rig enabling the flux rate to be quadrupled. The results obtained are set out in table 6.

It would seem from this, albeit limited, set of data that both ϵ and the incubation number, Ωt_i, are reasonably independent of flux rates over the range used: quadrupling the flux rate led to a quadrupling of the mass loss rate, and the incubation time was shortened to one quarter of its previous value. All this suggests that the damage processes are mechanical rather than thermal for this range of flux rates. This is, in fact, physically reasonable as the following argument shows (originally due to Andrews 1982*a*).

Suppose an impacting particle plastically deforms a volume of characteristic linear size, $\sigma^{0.5}$.

TABLE 6. EFFECT OF FLUX RATE ON EROSION AT 40°, SPEED OF IMPACT 36 ± 6 m s^{-1}

flux rate / kg m^{-2} s^{-1}	mass-loss rate / μg s^{-1}	ϵ / mg kg^{-1}	incubation time, t_i/s	incubation number, Ωt_i
5.33	5.9	12.6	285	104
11.0	15	15.4	130	98
22.0	24	12.4	75	113

Then the heat E put into this volume is $\rho\sigma^{1.5} C\Delta T$, where C is the specific heat of the polymer and ΔT the temperature rise. An upper bound to the decay time can be obtained ignoring radiation (probably small) and convection (probably large), and just considering conduction into the polymer. The heat flow rate is then given by $\kappa\sigma^{0.5}\Delta T$, where κ is the thermal conductivity. This ignores numerical factors of order unity.

Then
$$E = \rho\sigma^{1.5}\Delta T, \tag{6}$$
$$\mathrm{d}E/\mathrm{d}t = -\kappa\sigma^{0.5}\Delta T. \tag{7}$$

Eliminating T and rearranging gives
$$\mathrm{d}E/E = -\kappa\,\mathrm{d}t/\rho\sigma C, \tag{8}$$

whose solution is
$$E = B\exp(-\kappa t/\rho\sigma C), \tag{9}$$

where B is the constant of integration. Thus the characteristic decay time τ is $\rho\sigma C/\kappa$. Taking $\rho = 940$ kg m^{-3}, $\sigma = 17000$ μm^2, $C = 2.3$ J g^{-1}, $\kappa = 0.4$ W m^{-1} K^{-1}, gives $\tau = 0.09$ s. Since convection has been ignored this is an upper bound, i.e. the true time will be shorter. Thus a lower bound for the impact zone frequency ($1/\tau$) needed for heat build up is 11 s^{-1}. The data of table 5 for $\alpha = 40°$ show that the frequency achieved in these flux rate experiments varied over the range 0.4–1.2 s^{-1}, which is an order of magnitude down on the minimum frequency for thermal mechanisms to become significant. The practical effect of this is that accelerated erosion tests will give results valid for long-time, low-flux erosion of PE so long as the impact zone frequency is kept below *ca.* 10 s^{-1}. This corresponds to a macroscopic flux rate of *ca.* 180 kg m^{-2} s^{-1}, well above what we use, but almost certainly less than some workers have used in accelerated erosion tests!

A preliminary investigation was conducted into the effect of particle speed, but not enough data were collected to determine the power-law dependence. We feel that even if a large amount of data were available, it would be invalid to quote the exponent to more than two significant figures because the spread in particle speeds for any given driving pressure is about 10%. The data we collected are presented in table 7 (flux rates the same as in table 4).

TABLE 7. EFFECT OF PARTICLE SPEED AT A FLUX RATE THROUGH THE SPECIMEN SURFACE OF 3.5 ± 0.05 kg m^{-2} s^{-1}

angle/deg	speed / m s^{-1}	mass-loss rate / μg s^{-1}	ϵ/(mg kg^{-1})	incubation time/s
30	20 ± 3	1.2	3.0	2000
30	28 ± 4	1.3	3.2	800
30	36 ± 5	2.9	7.2	120
40	28 ± 4	1.7	4.2	240
40	36 ± 5	5.9	15.0	150

4. Single-particle studies

(*a*) *Introduction*

Craters produced by irregular grains of sand can only be dealt with statistically (as in tables 2 and 3) unless one is prepared to do an exhaustive particle by particle study (Bellman & Levy 1981). Even in that work, the impacts were not actually observed while they were occurring, although in several cases they were able to deduce how grains had struck from the damage done both to the surface and the particle.

Because in our experiments the sand grains are small (sub-millimetre) and travelling fairly slowly, there are major problems in using high-speed photography to film individual impacts. The small size means that high magnification would be needed, which would restrict the zone where the impact has to occur to be in focus to a narrow region along the line of sight. Also the contact times of small particles are very short, perhaps sub-microsecond (Hutchings 1977). This means that interframe times of *ca.* 1 μs would be needed to see anything useful. Thus either very precise triggering would be required (which is difficult because of both the small size of the grains and the 10% spread in speeds) or many frames would have to be taken in each sequence. This double requirement of small interframe times and long sequences is difficult to meet. Electronic cameras, such as the Imacon, allow shorter timescales to be investigated than any mechanical camera, but the number of frames is restricted, being at most *ca.* 18 for the Imacon. Tilly & Sage (1970) overcame these difficulties by using a whirling arm rig, in which the specimen moves and strikes the sand grains. An Imacon can be synchronized with the impact by using such a rig.

This option not being available to us, we adopted the method of Hutchings *et al.* (1976) and projected single macroscopic particles of simple shape to study the fundamental mechanisms of erosion in this material. The types of particle used are listed in table 8 along with their masses.

Table 8. Types of particles used in single-particle impact experiments

particle	mass/mg
2 mm diameter steel ball bearing	32.5±0.5
4 mm diameter steel ball bearing	258
4 mm diameter steel ball bearing with marker tag	264
5 mm diameter steel ball bearing	509
6 mm diameter steel ball bearing	878
5 mm diameter glass sphere	172
5 mm diameter glass sphere with marker tag	182
8 mm square steel plate (1.5 mm thick)	720

These sorts of projectiles are relatively easy to film by using the equipment described earlier (see figure 2). It may be objected (Bellman & Levy 1981) that such impacts are not representative of the energies and forces involved when real erosion by small particles takes place. However, the crater types we obtained show that this objection can be overcome. Major advantages of this approach are that the dynamics of impact and material deformation and loss mechanisms can be followed in detail.

(*b*) *Craters produced by single steel sphere impacts*

It was found that craters produced by steel spheres of diameter 2 mm and 4 mm can be plotted on a 'deformation map' (figure 8). This shows the crater type to be expected when

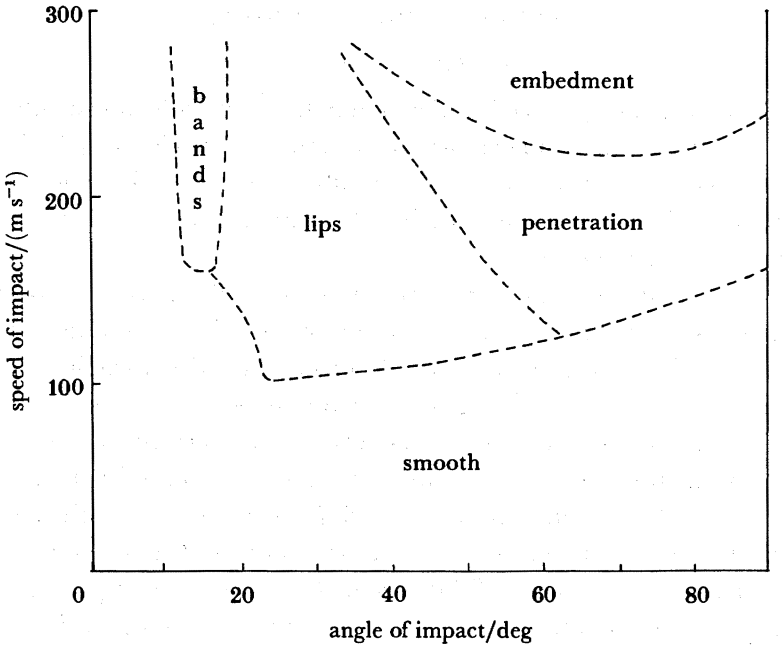

FIGURE 8. 'Deformation map' showing the type of crater to be expected when steel spheres strike a PE surface at various angles and speeds.

one of these spheres strikes with a given speed and angle. The map was constructed from the results of 160 impacts. A few shots that were performed with larger steel spheres also fitted into this pattern. Photographs of the various types are presented in figure 9, plates 3 and 4. Aluminium was deposited under vacuum on all specimens prior to photography. In the case of optical photography this provided an opaque, reflective coating.

'Smooth' craters are defined to be those where very little surface modification has taken place. Thus in figure 9*a* the original surface scratches have just been displaced by the passage of the ball. Over a narrow range of angles, the impact sites developed a regular series of 'bands' (figure 9*b*, *c*). It can be seen from the impression of their shape on the material in front of them that they have pulled back from the position they reached during impact. As the angle is raised, the bands become fewer (figure 9*d*) and then most of the displaced material ends up at the end of the crater as a 'lip' (figure 9*e*). Note in figure 9*d*, *e* the gradual increase of surface roughness from the entrance to the exit end. Surface scratches can be seen to run undeviated right up to the crater edge in the entrance end, but are turned in the direction of impact as the exit is approached. At high angles, it is possible for spheres to enter the surface to a depth greater than their radius and yet not be captured. This we term 'penetration' (see figure 9*f*). Note the radial striations indicating surface flow away from the lowermost point and also the line of discontinuity in slope about halfway down the entrance side. We think this is the circle of contact with the sphere at the instant of maximum penetration. If the speed is sufficiently high, enough material is displaced to envelope the sphere and prevent its ejection by elastic forces (figure 9*g*, *h*). This we call 'embedment'. Note that the speed needed to cause this to occur has a minimum around $\alpha = 70°$ (figure 8). We never observed embedment at 90°, though the maximum speed we used at this angle was 260 m s^{-1}.

It can be seen by comparing figures 3 and 9 that smooth and ploughed craters, the most

common types produced by sand grains (see table 2), are reproduced by ball impact. An anomaly can be seen here, however, in that lips do not form with steel spheres until the impact speed is greater than 100 m s^{-1} (figure 8), whereas sand grains produce the equivalent ploughing-type craters at much lower speeds (*ca.* 36 m s^{-1}). As damage varies with the damage number D ($= \rho_p v_i^2/\sigma_y$), where ρ_p is the particle density and σ_y the dynamic yield stress of the polymer (Hutchings 1982), and as the density of quartz (2600 kg m^{-3}) is less than that of steel (7800 kg m^{-3}), one would not expect sand grains to produce lipped craters until they had speeds in excess of 170 m s^{-1} (assuming σ_y is not significantly different in the two cases). It must be pointed out here that it is very difficult to justify the use of D for anything other than *normal* impact (Hutchings 1974), although it has been found experimentally to be useful for mild steel (Hutchings *et al.* 1976) and polypropylene (Walley *et al.* 1984) at impact angles less than 90°.

The resolution of this anomaly that we favour comes from a suggestion by Bitter (1963). He pointed out that the part of an irregular particle in contact with the surface will have a radius of curvature, r, much less than the characteristic linear size, R, of the whole sand grain. However, the mass associated with the point that is causing deformation is the mass of the whole particle. Thus mechanically to first order it behaves as a small sphere of density $(R/r)^3$ greater than the real material density. The moments of inertia, I, of the real particle and the imaginary small sphere are, of course, different due to the different distribution of mass about the contact point. I, for the sand grain, will be $(R/r)^2$ greater than that of the imaginary small sphere. Thus, all other things being equal, the real sand grain will have less tendency to be set into rotation by a frictional couple acting at the point of contact about the centre of mass. Now since sand grains travelling at 36 m s^{-1} at 20° to the surface are seen to cause damage equivalent to steel spheres travelling at 130 m s^{-1} at the same angle, the apparent density of the contact point given by the above argument is *ca.* 10^5 kg m^{-3}. The typical linear size of a whole grain is 450 μm, so the radius of the contact point must be given by $(R^3\rho_{quartz}/10^5)^{\frac{1}{3}} \simeq 130$ μm. As can be seen from figure 3, this is consistent with the width of the craters (the smooth one being 130 μm across, the lipped one 105 μm) and certainly inconsistent with the whole linear width of the sand grains having been involved.

(*c*) *Observations with high-speed photography*

The purpose of using large particles was to be able to use high-speed photography to observe what takes place during an impact. In this way, material-removal mechanisms can be identified, and quantitative information regarding rebound speeds and angles, energy losses, and dynamic hardness obtained. A preliminary investigation showed that typical contact times for steel spheres on PE were *ca.* 50 μs. Filaments were often seen being pulled out to very large strains on the rebound (figure 10, plate 5). Sometimes two filaments are drawn out (figure 10*m*, *n*). On one occasion only, a filament remained attached to a sphere during the subsequent impact with the specimen chamber (figure 11, plate 5), but its mass was too small to measure. This is not really surprising, since if the erosive efficiency of the spheres m_c/m_0 is the same as for the sand grains (10^{-5} from table 5), the filament had a mass of 5 μg, which our balances cannot detect. A lip can be seen being formed in the sequence of figure 12, plate 6. What is meant by 'penetration' is illustrated in figure 13, plate 6. The ball enters the surface to a depth greater than its radius. It is then expelled backwards (angle of rebound $\beta > 90°$) by the elastic response of the polymer. If embedment does occur, the amount of material displaced is large

(figure 14, plate 7). Note in this sequence that the lip continues to grow after the ball has disappeared from sight. The last three frames show the whole specimen pivoting about a point on the right-hand side; it was subsequently found to have been knocked out of the mount by the impact. The difficulty of producing embedment in normal impact is seen from figure 15, plate 7. The ball enters to a depth at least equal to its diameter, yet it still emerges!

Sequences like these can be analysed to give the speed and angle of rebound for various impact speeds and angles (figures 16 and 17). Two sets of data were taken. The first set (figure 16*a*, *b*) were obtained with PE specimens punched out from the 5 mm sheet and mounted as a single thickness on the surface of bakelite blocks. Later it was feared that the rigidity of the blocks behind could be influencing the rebound velocities, i.e. the back boundary was not far enough away for the 'semi-infinite' condition to be valid. So some impacts were repeated using a double thickness of the polymer sheet mounted in the massive steel holder used for the 2 mm diameter steel sphere shots. Additionally the floor of the angled mount had a PE block recessed into it below the specimens.

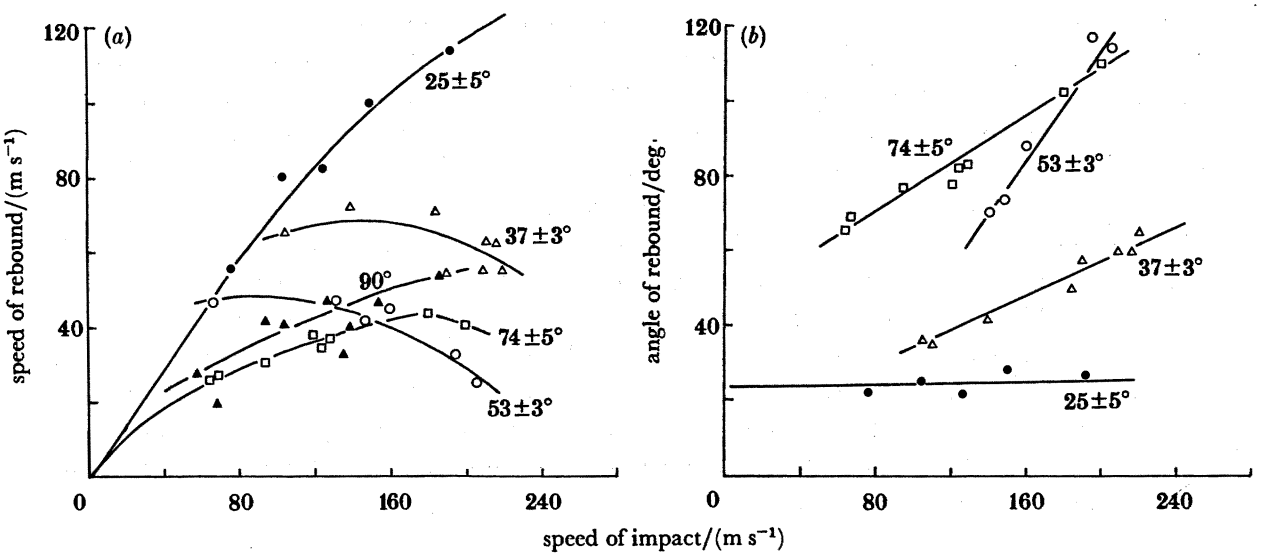

FIGURE 16. (*a*) Graph of the rebound speed against impact speed for various angles of impact. (*b*) Graph of the rebound angle against impact speed for various angles of impact. Specimen thickness, 5 mm.

Small differences were seen particularly at high impact speeds: the angle of rebound increased and the speed of rebound decreased more rapidly for the more compliant arrangement. However, when these data were converted to loss of kinetic energy (figure 17*a*, *b*) and fractional loss of kinetic energy (figure 18), no difference in the two data sets could be detected, within experimental error. This is not really surprising because the loss of energy is computed from the difference between the square of the impact speed, which is large, and the square of the rebound speed, which is small.

No analysis of oblique sphere impact on a thick block has yet correctly predicted the speed and angle of rebound. The difficulty arises in accounting for the forces exerted on the ball by the displaced material. If these are ignored and it is assumed that the magnitude of the vertical component of velocity is reduced by a factor e (the coefficient of restitution for normal impact

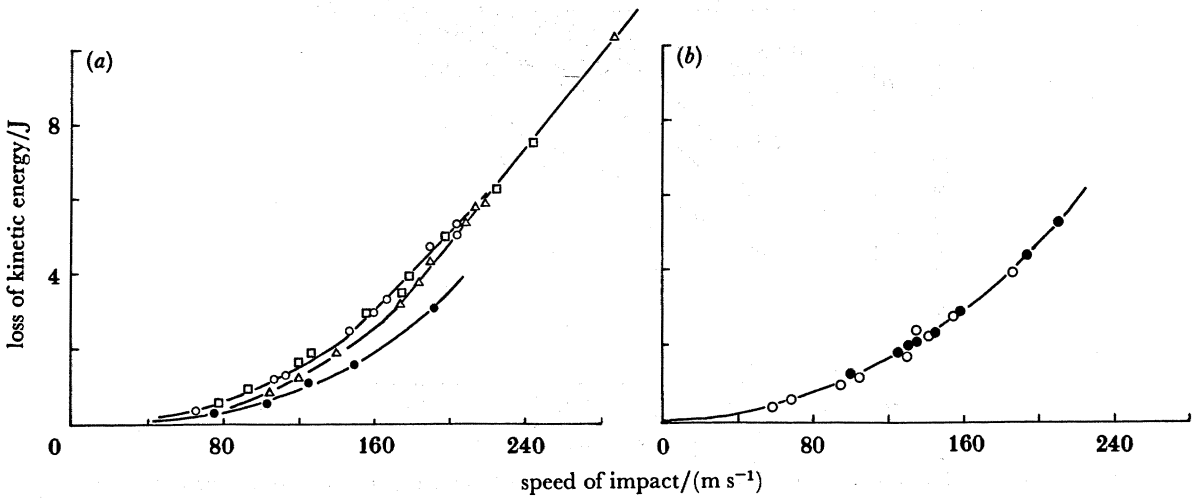

FIGURE 17. (*a*) Graph of the kinetic energy lost during impact against speed of impact for various angles of impact. Data from both 5 mm and 10 mm thick specimens. Symbols: ●, 25°; △, 37°; ○, 50°; □, 70°. (*b*) Graph of kinetic energy lost during normal impact. Open symbols: 5 mm thick specimens. Solid symbols: 10 mm thick specimens.

at a speed equal to the vertical component), and the horizontal component is reduced by friction, then

$$e\cot\beta = \cot\alpha - \mu(1+e), \tag{10}$$

where β is the rebound angle and μ the coefficient of friction (Hutchings 1974). By using the data illustrated in figure 16*a*, the value of e can be seen to decrease with increasing normal impact velocity, so β will decrease with impact speed according to (10). Not only is this prediction wrong, but the absolute values of β are also wrong, for this equation predicts $\beta = 9°$ for a 200 m s^{-1} impact at 37° if μ is taken to be zero (μ is known to be small under conditions of high sliding speed; Bowden & Persson 1961). In fact, it is doubtful whether the initial assumption that the frictional and normal forces act independently of each other is valid (Sundararajan 1984). Qualitatively the displaced material acts as a ramp, raising β, and as a brake, reducing the rebound speed, the greatest effect being seen for intermediate impact angles of 50–70° (figure 16).

Low-angle impacts (25°) are almost specular with comparatively little loss of energy. When α exceeds 60°, the loss of energy for a given impact speed increases little, hence the data for normal impact had to be plotted separately to avoid confusion (figure 17*b*). A plot of the loss of kinetic energy as a fraction of the initial energy (figure 18) shows clearly when embedment is likely to occur for a given angle (100% loss).

There has been some success with metals in deriving the crater volume numerically from the equations of motion of a sphere through a rigid-plastic medium with friction (Hutchings *et al.* 1981). In their model, the yield stress σ_y used is treated as a fitting parameter, which is reasonable because σ_y is known to vary with strain rate. However, they find that if they choose a value for σ_y to give a 'best fit' to the loss of kinetic-energy data, the volume of the crater formed is overestimated. This is almost certainly due to the displaced material filling up the crater ahead of the ball. Also with a rigid-plastic model solid there is no elastic recovery. That this is certainly not the case with polymers can be seen from figure 12, which shows a glass sphere impact. The lip can be seen springing back over a period of *ca.* 40 μs (frames 12*f*–*h*).

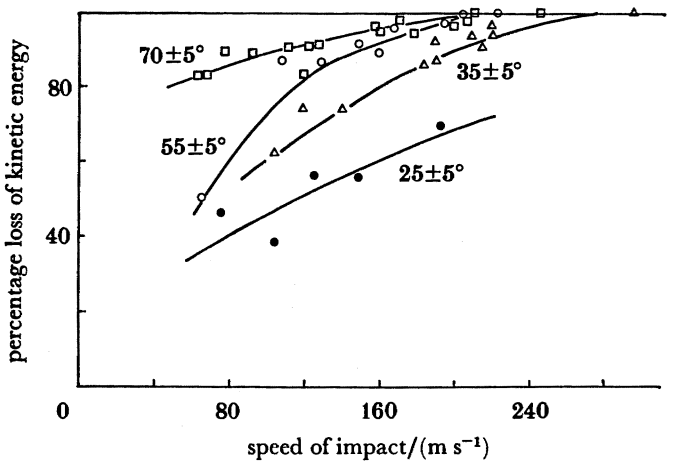

FIGURE 18. Graph of the fraction of kinetic energy lost against impact speed for various angles of impact.

Subsequent frames showed no further change. Since this time is commensurate with the contact time, it is quite certain that even as the ball rebounds, the entrance end of the crater will be recovering, and what we perform measurements on after the event are craters where substantial recovery has occurred.

Figure 19 shows Talysurf profilometer traces along and across an oblique impact crater. From these we define lip material as that which is displaced above the original surface, and the crater as the depression below the original surface. Although the Talysurf has been used to measure crater volumes on ceramics (see, for example, Rickerby *et al.* 1979) its sensitivity is such that we could only use it on craters shallower than 0.5 mm, such as were produced by 2 mm diameter steel spheres at low angles and speeds.

Crater volumes were measured by the simple method of cutting the lips off with a sharp blade and filling the depression with plasticene, the mass needed to do this giving the volume. Likewise the mass of the lip material gave the lip volume. These are plotted against speed of impact for various angles in figure 20.

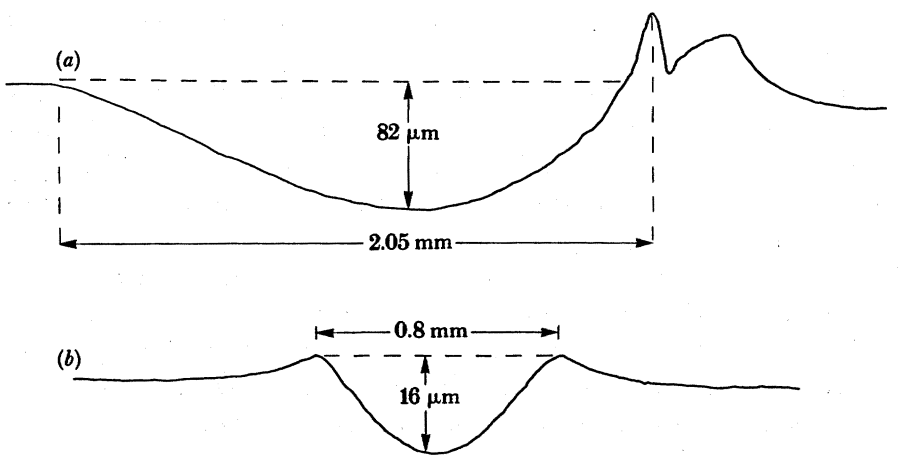

FIGURE 19. (*a*) Talysurf trace along a crater formed by the impact of a 2 mm diameter steel sphere from left to right. $v_i = 93$ m s^{-1}, $\alpha = 25°$. (*b*) Talysurf trace across a crater formed by the impact of a 2 mm diameter steel sphere. $v_i = 170$ m s^{-1}, $\alpha = 5°$.

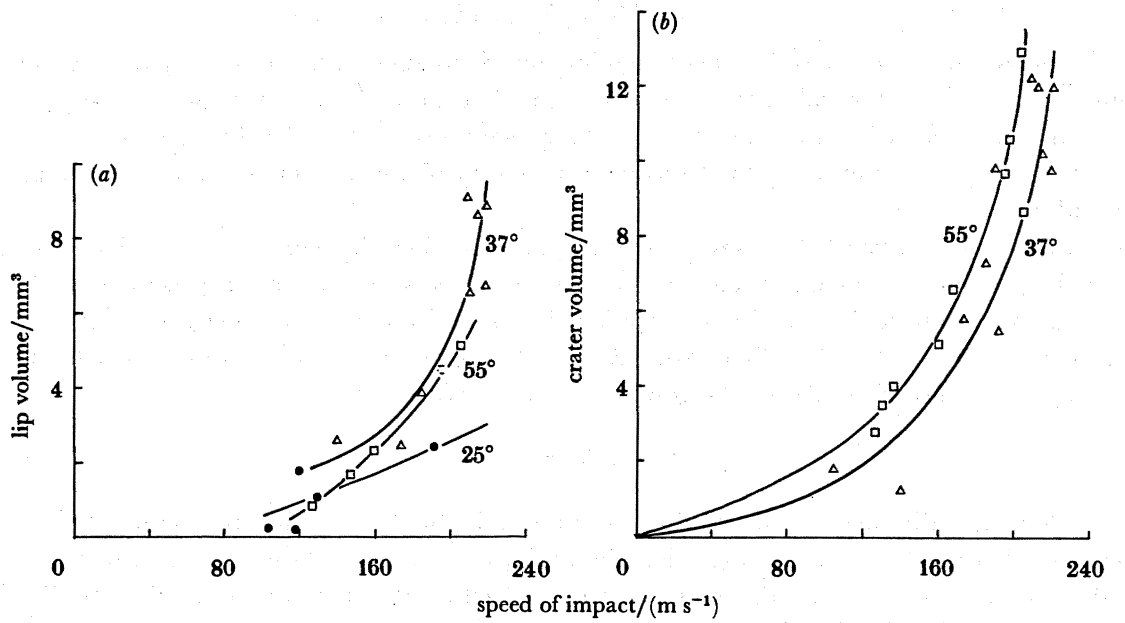

FIGURE 20. (*a*) Graph of the volume of lip material against speed of impact of 4 mm diameter steel spheres at various angles. (*b*) Graph of the crater volume against impact speed for the same impacts as in (*a*).

The scatter in the data for 25° and 37° impacts precludes a power-law fit, but the 55° data have velocity dependences for the crater volume of $v_i^{2.77\pm0.01}$ and lip volume of $v_i^{2.8\pm0.2}$. It can also be seen that the ratio of lip to crater volume is greater for 37° craters (*ca.* 0.75) than for the 55° craters (0.5 ± 0.15).

It is not known what fraction of the kinetic energy goes into crater as opposed to lip formation. However, it is possible to divide the volume of the two entities by the total energy to give plots of their specific energy of formation. Figure 21 gives this for the 55° data. This clearly shows the lip to have a smaller volume for a given unit of energy than the crater. Also both specific energies *decrease* with impact speed implying that a *greater* fraction of the energy dissipated goes into permanent material displacement as the velocity is raised.

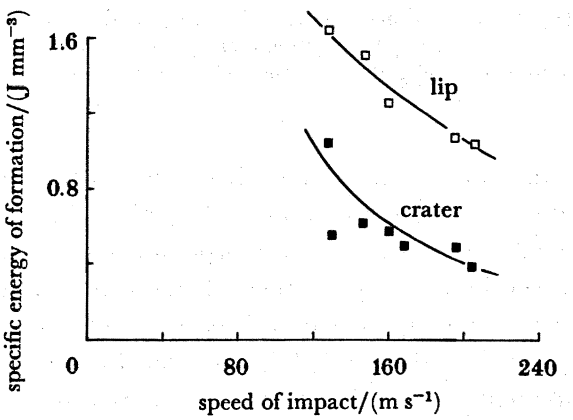

FIGURE 21. Specific energy of formation of lips and craters for 55° impacts.

(*d*) *Moiré photography*

The deformation produced by the normal impact of spheres on PE was investigated by using moiré methods. Crater volumes were measured after impact by using the 'out-of-plane' technique developed by Andrews (1982*b*). They were always considerably less than that at the instant of maximum deformation as determined by high-speed photography (see figures 22 and 23).

The outer arc of figure 22 is a cross section of a crater when the ball was at rest. The crosses show the position of the moiré fringes when the impact site was measured. It was found always to be possible to fit a circular arc to the relaxed cross section, e.g. the inner arc of figure 22. This gave the relaxed radius of curvature R_r, and hence also the volume of the relaxed crater V_r using the general formula for the volume V of a spherical cap

$$V = \pi(RD^2 - \tfrac{1}{3}D^3), \tag{11}$$

where R is the radius of curvature and D the chordal depth. The middle arc of figure 22 shows the error that results if it is assumed that the radius of curvature of the relaxed crater is that of the sphere that caused it. The volume V_c calculated on this assumption is substantially in error, and would give highly erroneous values of the dynamic hardness. That the crater diameter contracts as well as the depth is easily confirmed by placing one of the spheres used on the relaxed crater: it rests on the top, not the bottom.

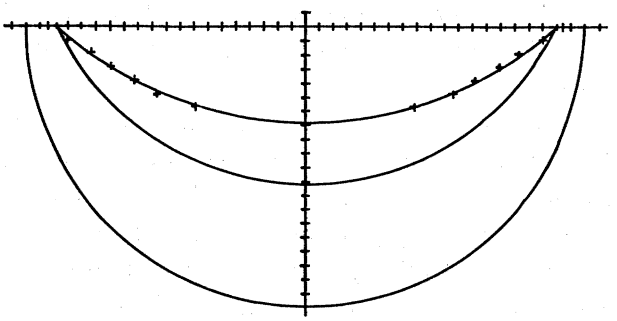

FIGURE 22. Diagram to show the extent of relaxation of a normal impact crater. The inner arc is the crater profile one month after impact calculated by the out-of-plane moiré fringe method. The outer arc is the maximum extent of deformation as observed during impact by using high-speed photography. The middle arc illustrates the error that would result from assuming that the chordal diameter did not relax. The tick marks are 0.1 mm apart.

By fitting power laws to the crater volume data, it was found that the maximum volume of indentation V_i varies as $v_i^{2.0\pm0.1}$, the relaxed volume V_r as $v_i^{2.67\pm0.01}$. Thus the ratio $V_r : V_i$ rises from 0.1 at $v_i = 80$ m s^{-1} to 0.2 at 140 m s^{-1}, i.e. proportionally less relaxation occurs at higher impact speeds. This is also seen by the way the relaxed radius R_r varies with v_i in figure 23. Relaxation was found to continue for periods of at least two weeks after impact, the volume of the crater studied declining from 3.6 mm^3 to 2.7 mm^3 over this period. Thus it is important to specify when the measurement was taken. All the data plotted in figure 23 were obtained at least four weeks after impact.

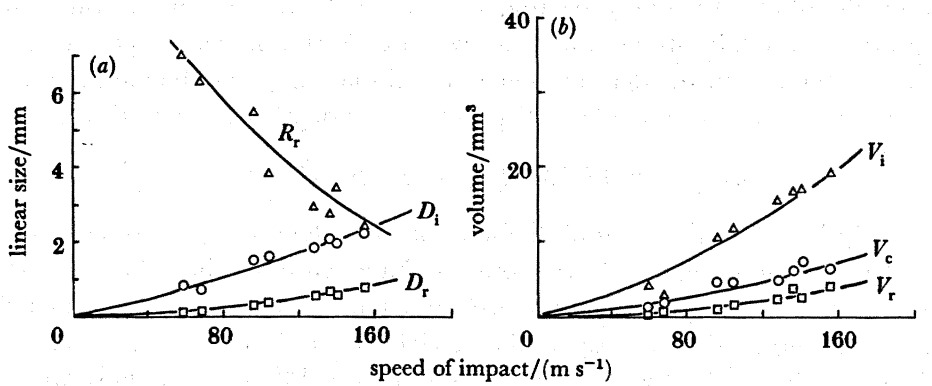

FIGURE 23. (*a*) Plots of the linear dimensions of normal impact craters formed by 4 mm diameter steel spheres against speed of impact. D_i is the maximum depth during impact; D_r is the depth after relaxation for at least a month; R_r is the relaxed radius of curvature. (*b*) Plots of normal impact crater volumes against speed of impact. V_i is the maximum volume during impact; V_c is the erroneous volume calculated assuming depth relaxation but no chordal relaxation; V_r is the true relaxed volume determined by moiré methods.

It can be seen from figure 24 that the rim of the crater is raised above the original surface. The volume of this raised material V_{rim} may be calculated from the solid of revolution as:

$$V_{rim} = 2\pi \int_{\frac{1}{2}W}^{(\frac{1}{2}W)+b} r z(r)\, dr, \tag{12}$$

where W is the chordal width, b the rim width and $z(r)$ describes the rim profile along the radius vector r. This works out as 13% of the relaxed volume for the impact site shown in figure 24.

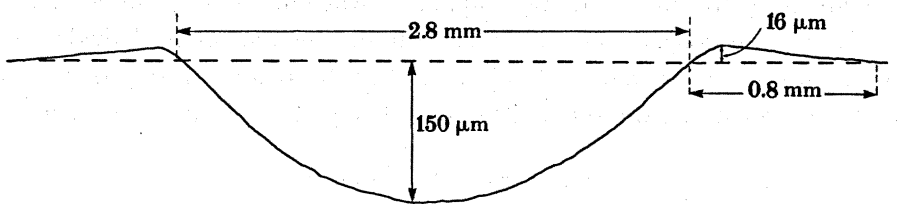

FIGURE 24. Talysurf profile of a relaxed normal impact site produced by a 2 mm diameter steel sphere; $v_i = 68$ m s^{-1}, $v_r = 20$ m s^{-1}.

This result raises the question as to where the rest of the material displaced by the impact went. There are two possibilities: (i) if PE behaves incompressibly, the surface must have been raised for some considerable distance out from the crater, but by an amount less than the resolution of the Talysurf profilometer; (ii) the PE could have densified beneath the impact site. We were unsuccessful in confirming the second possibility directly using infrared absorption on a cross section through the crater region. However, we were able to determine the size of deformation zones resulting from both quasi-static indentations (figure 25*a–d*, plate 8) and dynamic impacts (figure 25*e*, *f*, plate 9) by using an in-plane moiré method. One piece of grating, printed on a 25 μm thick film, formed the 'filling' of a 'sandwich' of PE, the film being attached to one of the pieces of PE using a cyanoacrylate glue. The sandwich was held together with a U-shaped steel spring embedded in polystyrene resin and the top surface machined flat. Simple line gratings gave the clearest fringes (figure 25*a–d*), but because of the low success rate

due to the difficulty of indenting or impacting a line normally by a sphere, it was desirable to use crossed gratings to obtain displacements in two directions from each experiment.

To a good approximation, the deformation zone volume V_{zone} may be found by assuming the boundary is a spherical arc of diameter X, penetrating a depth Y beneath the surface. Then

$$V_{\text{zone}} = \pi\{Y^2(\tfrac{1}{2}X - \tfrac{1}{3}Y) - (\tfrac{1}{6}d)(d^2 + \tfrac{3}{4}W^2)\}, \tag{13}$$

where d is the depth and W the chordal diameter of the indentation. By using this formula, the region of deformation in figure 25*e* was found to have ten times the volume of the crater. Note also that these sandwich specimens differ from uncut blocks in that no raised rim is formed. Thus it is even more certain that the displaced material entered the deformation zone, and thus must have increased in density by 10% on average. Figure 25 also shows how far specimen boundaries should be kept from the impact, for grid lines up to a distance of *ca.* 5 times the crater depth are bent, and this *after* relaxation. Oblique impacts were also found to produce deformation out to this order of distance.

This method gives an upper bound to the value of the bulk temperature rise to be expected during impact. For the zone of figure 25*e*, *f* has a volume of 115 mm^3 and hence a heat capacity of 0.26 J K^{-1}, from the values for density and specific heat given in table 1. The 6 mm diameter steel sphere that caused this deformation had an impact speed of 124 m s^{-1} and a rebound speed of 32 m s^{-1}, so it lost 6.3 J of energy in this process. If all this energy were uniformly and adiabatically dissipated within the deformation zone, the temperature rise would be *ca.* 25 K. This is far too small to cause bulk melting, although since the energy clearly is not dissipated uniformly, it is possible that a small amount of molten polymer could form. This would explain the 'angel wings' seen in the crater of figure 26, plate 10. These were formed around a sphere that was brought to a stop in an oblique impact (it was only loosely embedded and fell out before the picture was taken). Several other oblique impacts showed evidence of a thin, strongly sheared surface layer (figure 27, plate 10) but this deformation probably occurred in the solid state. In some cases, the sheared material bridged cracks in the polymer.

(*e*) *The dynamic hardness*

Imacon sequences of normal impact, in principle, allow the dynamic hardness to be calculated. For if we assume with Tabor (1951) that the resistance to the sphere's progress into the surface is due to a pressure, P, acting over the projected area of contact, then the equation of motion is simply

$$m\ddot{x} = -P\pi(2Rx - x^2), \tag{14}$$

where x is measured in the direction of motion and m is the sphere's mass. When the sphere is momentarily at rest, we know that the work done by the resistance equals the initial kinetic energy of the ball. Thus

$$\tfrac{1}{2}mv_1^2 = P\pi \int_0^{D_1} (2Rx - x^2)\,\mathrm{d}x$$

$$= P\pi[RD_1^2 - \tfrac{1}{3}D_1^3].$$

Therefore

$$\tfrac{1}{2}mv_1^2 = PV_1, \tag{15}$$

from (11). Note that P is assumed constant during the impact. If this is not the case, what we calculate from (15) is an average hardness. Also, only those impacts when $D_1 < R$ can be used.

The results are tabulated in table 9. It can be seen that the nearness of the boundary with the rigid substrate raised the apparent hardness when a single 5 mm thickness of PE was used, the effect becoming greater as the impact speed was raised. When double-thickness specimens were used, the measured dynamic hardness was the same as the quasi-static values. The biggest error in these calculations comes from the volume, for if the Imacon is used to determine the impact and rebound speeds the magnification is of necessity low and hence the depth of penetration rather inaccurately determined.

TABLE 9. THE HARDNESS OF PE DEDUCED FROM SPHERE IMPACTS

sphere diameter/mm	specimen	speed of impact / m s^{-1}	hardness/MPa
3.0 (steel)	moiré sandwich	*ca.* 10^{-5}	80
4.0 (steel)	moiré sandwich	*ca.* 10^{-5}	60
5.0 (steel)	moiré sandwich	*ca.* 10^{-5}	75
5.0 (steel)	moiré sandwich	*ca.* 10^{-5}	70
4.0 (steel)	5 mm thick sheet	59	115
4.0 (steel)	5 mm thick sheet	104	115
4.0 (steel)	5 mm thick sheet	128	160
4.0 (steel)	5 mm thick sheet	140	170
4.0 (steel)	2 thicknesses of 5 mm sheet	100	75
4.0 (steel)	2 thicknesses of 5 mm sheet	100	75

(*f*) *A comparison of glass and steel sphere impacts*

If the depth of penetration is small, we can ignore the term in x^2 in (15), which therefore becomes simple harmonic. Thus the solution for the contact time t_p is

$$t_p = \pi(\tfrac{1}{8}m\pi PR)^{\frac{1}{2}} \tag{16}$$

(Tabor 1951). We were unable to check this quantitatively as t_p is uncertain to about half an interframe time (9 μs) and P is also poorly known (see table 9). However, (16) predicts that spheres of the same size but different densities (and hence different masses), should have different contact times. Specifically glass spheres should be in contact for less time than steel spheres. This was indeed found to be the case (figure 28).

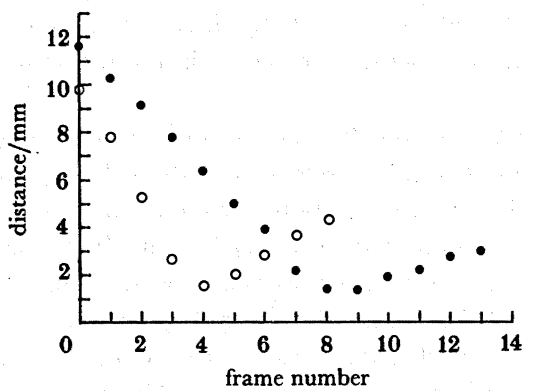

FIGURE 28. Plot of the position of the centre of mass against Imacon frame number (interframe time 17 μs) for two normal impacts by 5 mm diameter spheres. Glass (open symbols): $v_i = 147$ m s^{-1}, $v_r = 33$ m s^{-1}. Steel (solid symbols): $v_i = 78$ m s^{-1}, $v_r = 24$ m s^{-1}. Note the difference in contact times.

A few oblique impacts were performed to see if, when the parameter ρv^2 was the same for the two types, the damage was the same. Two craters are compared in figure 29, plate 11, where the ratio of the speed of the glass sphere to that of the steel sphere was about 1.7 (the ratio of densities is 0.34). The gross features are almost identical, but there are differences in the small-scale features such as the start of rippling in the crater. In general, the energy losses are comparable, although, as might be expected, the rebound speeds were higher for glass spheres.

(*g*) *The coefficient of friction in oblique impact*

None of the Imacon sequences presented so far contains information about whether the spheres are set into rotation by impact. To investigate this, we used the same technique as Hutchings *et al.* (1976), placing tags on both glass and steel spheres. These were fired at low angles of incidence (between 30° and 40°) so that they would slide a distance at least equal to their diameter to allow the frictional forces, if any, to impart as great an angular impulse as possible. In all these experiments, none of the tagged spheres was ever observed rotating before impact.

An estimate of the average friction coefficient $\bar{\mu}$ may be made by using the following argument (Hutchings 1974). We do not know how the friction force, F, and the normal reaction force, N, vary with time, but we do know the total impulses they deliver, since

$$\int N(t)\,\mathrm{d}t = \Delta(mv)_{\mathrm{N}}, \tag{17}$$

$$\int RF(t)\,\mathrm{d}t = \Delta(I\omega), \tag{18}$$

where I is the moment of inertia, ω the rotation rate and subscript N denotes normal components. We therefore define $\bar{\mu}$ as

$$\bar{\mu} = \int F(t)\,\mathrm{d}t \Big/ \int N(t)\,\mathrm{d}t, \tag{19}$$

which from (17) and (18) gives

$$\bar{\mu} = \Delta(I\omega)/R\Delta\,(mv)_{\mathrm{N}}. \tag{20}$$

Steel spheres were never observed to be set rotating unless filaments were drawn out. Often these filaments would cause rotation out of the plane of the photograph, but the one case which did rotate in the plane (by 4° in 51 μs) suggests the filaments were exerting a force of about 10 N. Glass spheres were, however, unambiguously set into rotation by friction alone (see, for example, figure 30, plate 11).

One problem with using a tag is that the moment of inertia, I, is significantly altered. In the case of the glass sphere, the tags were welded on with a flame, and as can be seen, they did not usually have a uniform cross section. Being at the periphery, their estimated contribution to I depends strongly on their mass distribution. It can be seen from table 8 that a typical tag mass is 10 mg. If this is regarded as being located 3 mm from the sphere centre, its moment of inertia is *ca.* 10^{-10} kg m^2, cf. I for the untagged spheres 4.2×10^{-10} kg m^2.

The impact shown in figure 30 produced a measured rotation of 3° per frame (17 μs). Another glass sphere impact give 4° per frame at a lower speed. The calculation of $\bar{\mu}$ is tabulated in table 10.

An estimate of the sensitivity of this technique, and hence a lower bound for the friction that

TABLE 10. DATA FROM WHICH COEFFICIENTS OF FRICTION WERE CALCULATED

velocity of impact α^0 / m s^{-1}	velocity of rebound β^0 / m s^{-1}	rotation / krad s^{-1}	$\Delta(I\omega)$ / kg m^2 s^{-1}	$\Delta(mv)_N$ / kg m s^{-1}	coefficient of friction, $\bar{\mu}$
glass ($238\pm7, 38°\pm1°$)	($102\pm2, 42°\pm1°$)	3.1	1.6×10^{-6}	1.4×10^{-2}	0.045
glass ($210, 36°\pm2°$)	($110, 45°\pm3°$)	4.2	2.1×10^{-6}	0.83×10^{-2}	0.10
steel (108, 36°)	(62, 31°)	0	0	0.83×10^{-2}	$\leqslant 0.012$

can be measured, may be made from the tagged steel spheres. These were observed, on average, not to rotate, but a typical set of values for the inclination of the tag to the horizontal is: 37°, 34°, 37°, 40°, 34°, 40°, the average and error of which are clearly $37°\pm3°$. Thus if a ball were rotating sufficiently slowly that after six frames (the usual number achieved following an impact) it had turned through 3° or less, we would conclude the ball had not rotated within experimental error; 3° in 102 μs is a rotation rate of *ca.* 0.5 krad s^{-1}. From the data of table 10, this implies a minimum detectable friction coefficient of 0.008 for glass and 0.012 for steel in these experiments. Thus we conclude $\bar{\mu}$ for steel sliding on PE in oblique impact at 100 m s^{-1} is less than 0.012.

(*h*) *Square-plate impacts*

Impacts were performed with 8 mm × 8 mm × 1.5 mm square steel plates to model the formation of craters classified as 'cut' or 'sharp dents' in table 2. To describe the impact of a sharp particle, one extra parameter is needed over and above what are needed for spheres, and that is a measure of its orientation. The standard method to describe this is taken from machining theory, and that is to specify the angle the front face makes with a normal to the surface. This is termed the rake angle, $-\gamma$ (negative for forward-leaning particles).

In these experiments, the firing pressure of the gun was held constant so that all impacts took place within a small velocity range, 75–100 m s^{-1}, most being around 85 m s^{-1}. All, except one (figure 31, plate 12), were caused to rotate in a forward sense by impact. The rebound speed was observed to decline as the impact angle increased, whereas the rebound angle, β, increased; β was usually just a few degrees less than α. The imparted rotational kinetic energy lay in the range 0.02–0.2 J, which is 1–10% of the energy of impact.

The back rotating impact of figure 31 produced the damage site shown in figure 32*a*, plate 13. This type of damage, where a chip of polymer is produced by a machining action, required low values of α and $-\gamma$. This criterion was sometimes produced by the impact itself, the plate rotating forwards and striking the surface a second time at a favourable orientation. The chip stayed attached in all cases where the plate rotated forwards (figure 32*b*, plate 13). In real erosion, this sort of mechanism, damaging though it is, is likely to contribute little to the loss of material, as the range or orientations required is so small ($0° > -\gamma > -15°$).

In most impacts at moderate angles, the point of contact was simply dragged through the surface by the motion of the plate producing cut craters with material displaced to the sides (figure 32*c*, plate 13). These are similar in appearance to the cutting-type craters produced by sand grains (figure 3*c*).

High-angle impacts produced sharp dents (figure 32*d*, plate 14). Material outside the crater seems not to have been displaced by the impact. However, enlargement of the area close to the base of the lip of the crater, shown in figure 32*b*, revealed shear bands extending several hundred microns out into the surrounding material (figure 33, plate 12).

5. Conclusions

(*a*) Primary data on the erosion of gas-pipe grade PE have been obtained for various speeds and angles of impact and for various flux rates, the erodent being 300–600 μm sieved quartz sand. It was found that the erosion against angle curve is similar to that of ductile metals, although with the difference that no mass loss was detected for angles of impingement greater than 80°.

(*b*) There are not only similarities but also differences between the erosion behaviour of polymers and ductile metals. Single-particle oblique impact on metals often produces lips that are only weakly attached to the substrate (Hutchings *et al.* 1976), whereas in PE the displaced material is quite strongly bonded. Only a few subsequent impacts may be needed to remove lip material in metals whereas the incubation number for PE is several tens or even hundreds of impacts. Both show most mass loss at 20–30°, but PE was not observed to lose mass at close to normal impact. This may be contrasted with metals, which exhibit finite erosion at 90°.

(*c*) The other major differences between the impact response of polymers and metals are due to their thermal properties, particularly their relative melting points, thermal conductivities, heat capacities and heats of fusion. A theoretical analysis, originally due to Andrews (1982*a*), has been used to calculate the flux rate for which thermal mechanisms of erosion start to become important. For PE, we estimate that thermal effects would become significant at a flux rate of *ca.* 180 kg m^{-2} s^{-1}. This is six times the rate used in our erosion rig, but emphasizes the problems of testing polymers in accelerated erosion experiments.

(*d*) High-speed photography, scanning electron microscopy, and moiré methods have been used to gain quantitative information about the mechanics of single particle impact damage on PE. These methods gave: (i) the energy dissipated during impact for a range of impact angles and speeds; (ii) the coefficient of high-speed sliding friction; (iii) the size of the deformation zone; (iv) the temperature rise during impact. Two erosion mechanisms were identified for single impacts: the drawing out of filaments by rounded particles, and the cutting off of chips by sharp particles.

(*e*) A comparison of the damage produced by sand grains moving at *ca.* 35 m s^{-1} and steel spheres travelling at *ca.* 130 m s^{-1} showed that macroscopic particle studies model sand impact damage processes quite well. This we attribute to the large 'effective density' of the small irregularities on the grains that communicate the change of momentum of the whole particle to the eroding surface.

(*f*) Recently we have extended our studies to polypropylene (PP) (Walley *et al.* 1984) and polyetheretherketone (PEEK) and have obtained 'deformation maps' for both these materials. Both exhibited ductile behaviour, but PEEK, and to a lesser extent PP, showed a brittle response under some conditions. The great attraction of PE in a low velocity erosive environment is its ductile response under most conditions and its relatively low susceptibility to erosion.

This work was sponsored by the Engineering Research Station (ERS) of the British Gas Corporation (BGC). We thank Dr M. Howe of the ERS for his interest and advice. S.M.W. would like to thank the BGC for a research scholarship. Thanks, too, are due to Dr D. R. Andrews, who designed the multiparticle erosion rig and also shared his insights into

solid particle erosion, Mr C. D. Greenaway for assistance with the multi-particle erosion work, Professor F. P. Chiang for introducing us to moiré methods, and Dr B. J. Briscoe, who made valuable comments upon this work.

References

Andrews, D. R. 1980 Ph.D. thesis. University of Cambridge.
Andrews, D. R. 1981 *J. Phys.* D **14**, 1979–1991.
Andrews, D. R. 1982*a* SERC Junior Fellowship final report.
Andrews, D. R. 1982*b* *Opt. Engng* **21**, 650–654.
Andrews, D. R. 1983*a* *J. Phys.* E **16**, 192–193.
Andrews, D. R. 1983*b* *J. Phys.* E **16**, 706–709.
Andrews, D. R. & Field, J. E. 1982*a* *J. Phys.* D **15**, 571–578.
Andrews, D. R. & Field, J. E. 1982*b* *J. Phys.* D **15**, 2357–2367.
Andrews, D. R. & Horsfield, N. 1983 *J. Phys.* D **16**, 525–538.
Andrews, D. R., Walley, S. M. & Field, J. E. 1983 In *Proc. 6th Int. Conf. on Erosion by Liquid and Solid Impact* (ed. J. E. Field & N. S. Corney), paper 36. Cavendish Laboratory, University of Cambridge.
Bellman, R. Jr & Levy, A. 1981 *Wear* **70**, 1–27.
Benjamin, P. 1980 *Plast. Rubb. Int.* **4**, 269–273.
Bitter, J. G. A. 1963 *Wear* **6**, 169–190.
Bowden, F. P. & Persson, P. A. 1961 *Proc. R. Soc. Lond.* A **260**, 433–458.
Bragaw, C. G. 1979 In *Proc. 4th Int. Conf. on Plastics Pipes*, paper 23. London: Plastics and Rubber Inst.
Cousens, A. K. & Hutchings, I. M. 1983 In *Proc. 6th Int. Conf. on Erosion by Liquid and Solid Impact* (ed. J. E. Field & N. S. Corney), paper 41.
Engel, L., Klingele, H., Ehrenstein, G. W. & Shaper, H. 1981 *An Atlas of Polymer Damage.* London: Wolfe Science Books.
Finnie, I., Wolak, J. & Kabil, Y. H. 1967 *J. Mater.* **2**, 682–700.
Gaur, U. & Wunderlich, B. 1981 *J. Phys. Chem. Ref. Data* **10**, 119–152.
Gorham, D. A. 1979 In *Proc. 2nd Int. Conf. on Mechanical Properties at High Rates of Strain* (ed. J. Harding), chap. 1. London: Inst. of Physics.
Greenaway, C. D. 1982 Cavendish Laboratory Internal Report.
Hutchings, I. M. 1974 Ph.D. thesis, University of Cambridge.
Hutchings, I. M. 1977 *J. Phys.* D **10**, L179–L183.
Hutchings, I. M. 1982 In *Proc. 29th Sagamore Army Materials Research Conf.* (ed. J. Mescall & V. Weiss), pp. 161–196. New York: Plenum Press.
Hutchings, I. M., MacMillan, N. H. & Rickerby, D. G. 1981 *Int. J. mech. Sci.* **23**, 639–646.
Hutchings, I. M., Rochester, M. C. & Camus, J.-J. 1977 *J. Phys.* E **10**, 455–457.
Hutchings, I. M. & Winter, R. E. 1975 *J. Phys.* E **8**, 84–86.
Hutchings, I. M., Winter, R. E. & Field, J. E. 1976 *Proc. R. Soc. Lond.* A **348**, 379–392.
Meldt, R. 1982 In *Proc. 5th Int. Conf. on Plastics Pipes*, paper 29. London: Plastics and Rubber Inst.
Rickerby, D. G., Pramila Bai, B. N. & MacMillan, N. H. 1979 *J. mater. Sci.* **14**, 1807–1816.
Schmitt, G. F. Jr 1980 In *Wear control handbook* (ed. M. B. Peterson & W. O. Winer), p. 247. New York: ASME.
Sheldon, G. L. & Finnie, I. 1966 *Trans. Am. Soc. mech. Engrs* B **88**, 387–392.
Söderberg, S., Hogmark, S., Engman, U. & Swahn, H. 1981 *Tribology Int.* **14**, 333–342.
Sundararajan, G. 1982 *Wear* **97**, 9–14.
Swallowe, G. M. & Field, J. E. 1982 *Proc. R. Soc. Lond.* A **379**, 389–408.
Tabor, D. 1951 *The hardness of metals.* Oxford: Clarendon Press.
Taylor, G. I. & Quinney, H. 1934 *Proc. R. Soc. Lond.* A **143**, 307–326.
Tilly, G. P. 1969*a* *Wear* **14**, 63–79.
Tilly, G. P. 1969*b* *Wear* **14**, 241–248.
Tilly, G. P. & Sage, W. 1970 *Wear* **16**, 447–465.
Timothy, S. P. & Hutchings, I. M. 1981 In *Proc. 7th Int. Conf. on High Energy Rate Fabrication, Leeds* (ed. T. Z. Blazynski), pp. 19–28.
Walley, S. M. 1983 Ph.D. thesis. University of Cambridge.
Walley, S. M., Field, J. E. & Yennadhiou, P. 1984 *Wear* **100**, 263–280.

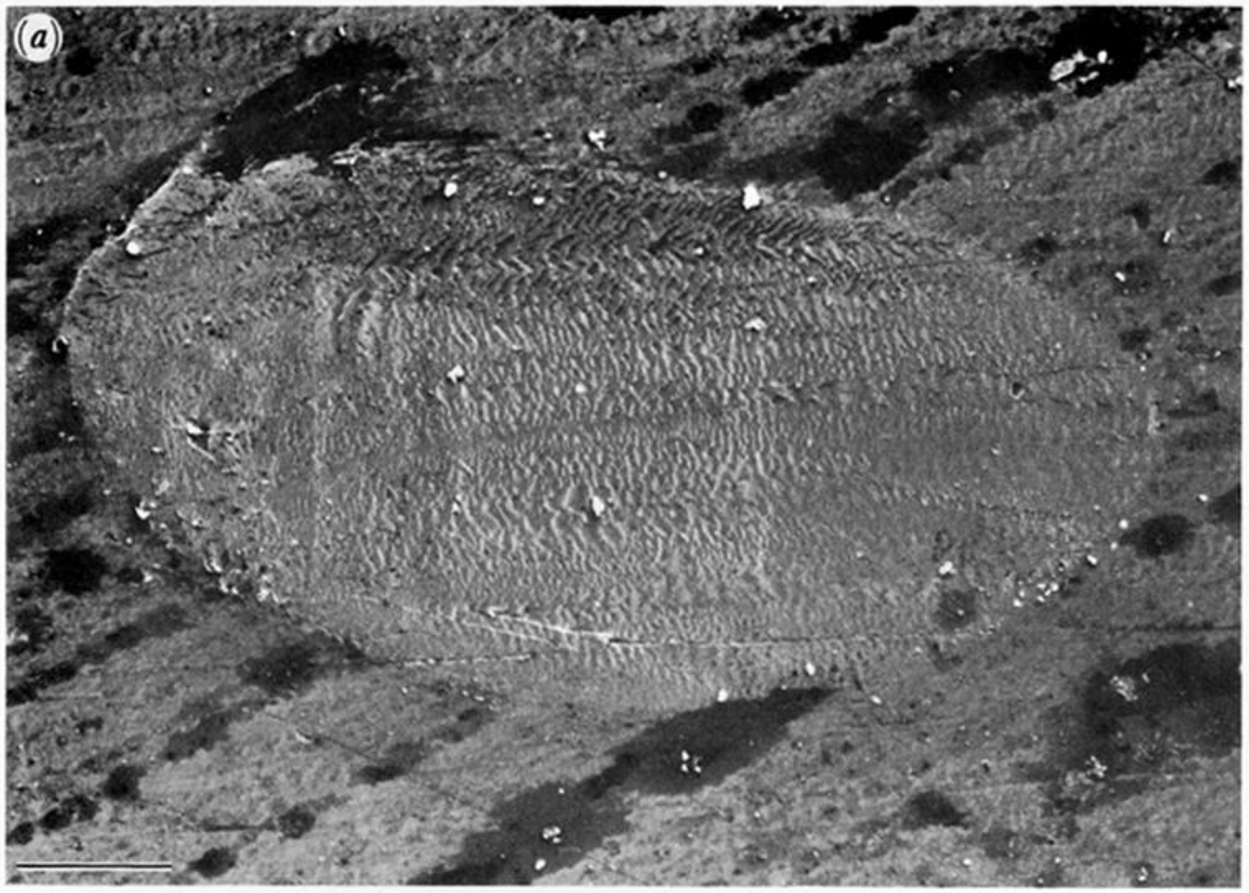

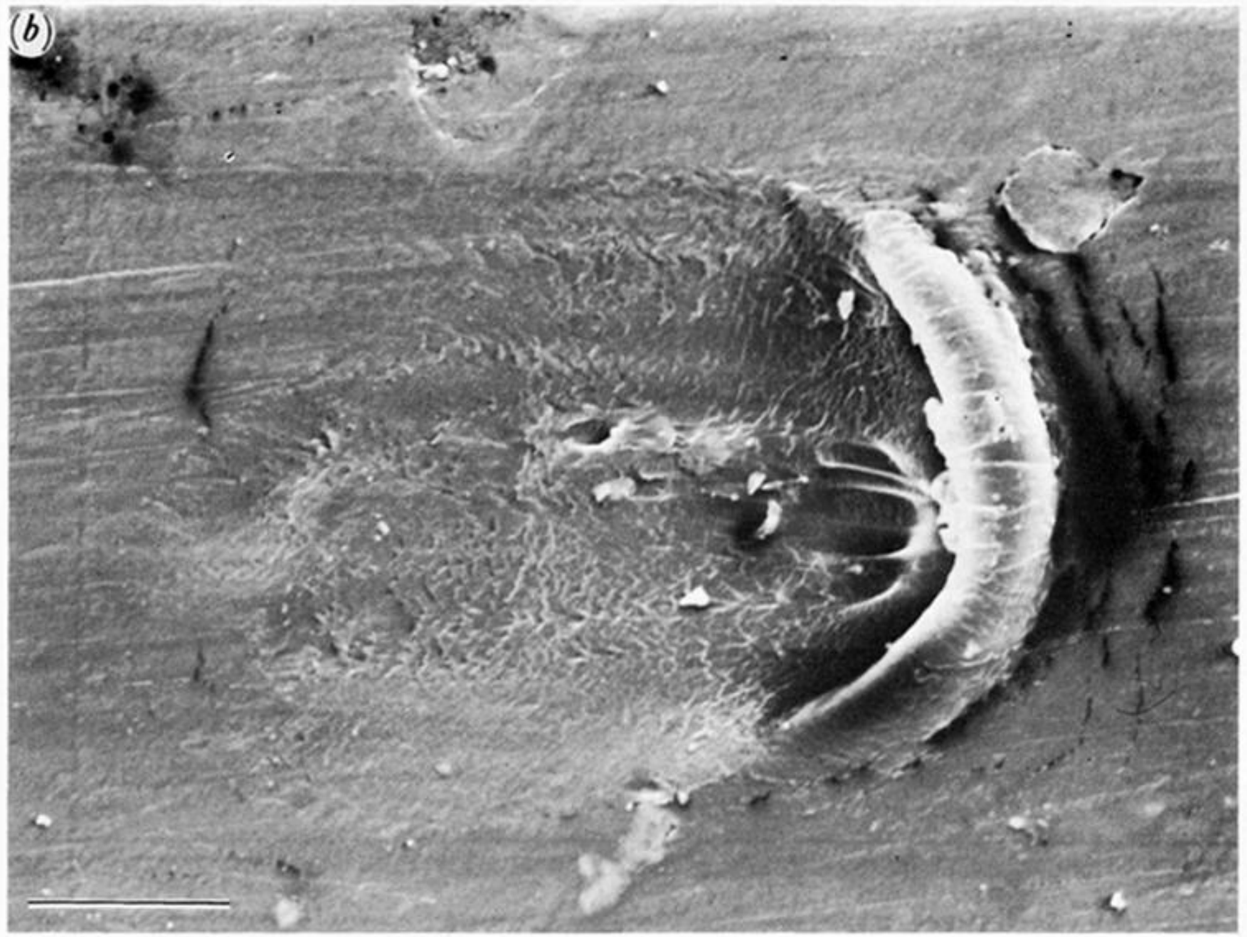

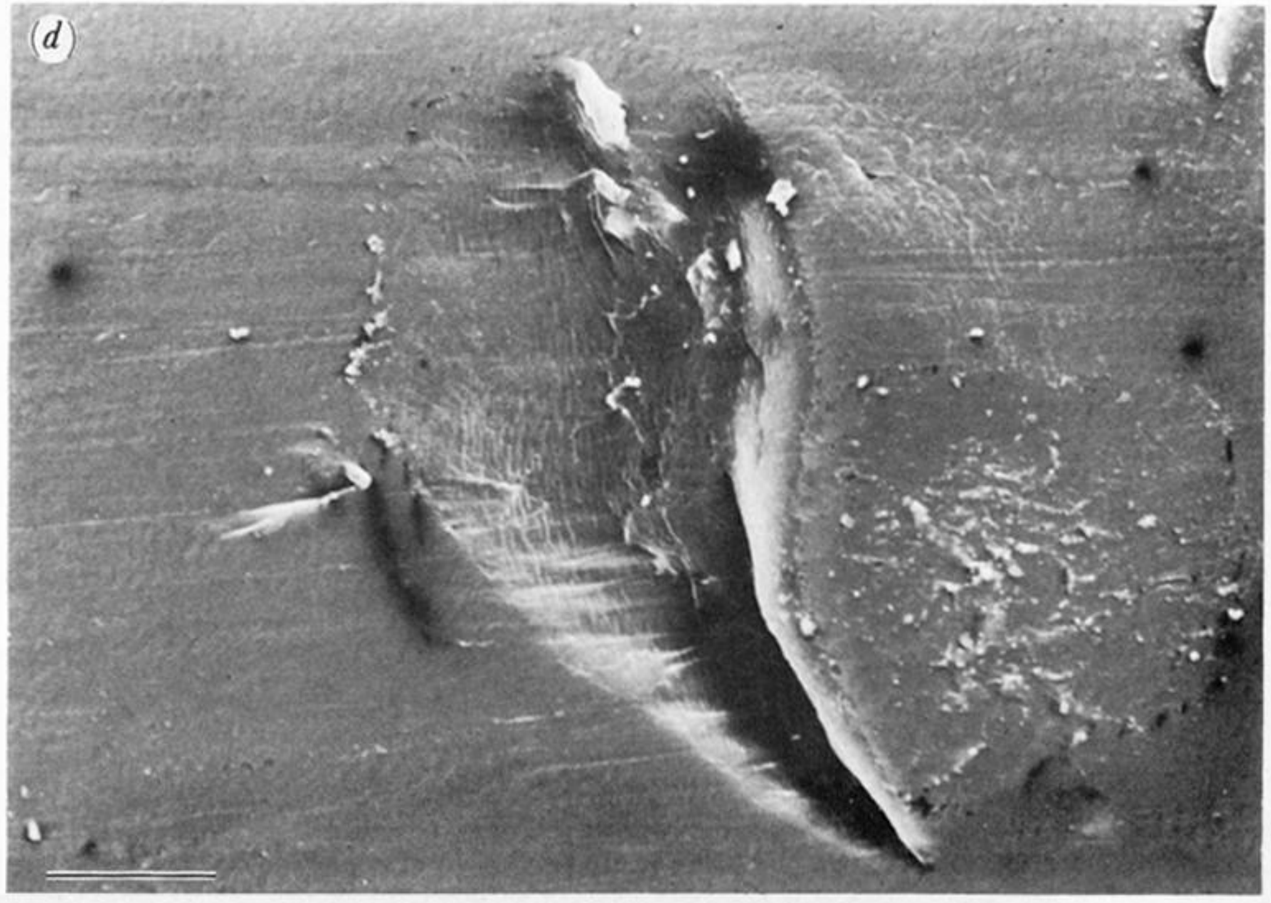

FIGURE 3. Examples of single-impact sites formed by 300–600 μm sieved sand travelling at 36 ± 6 m s^{-1}. The scale bars represent 40 μm. (*a*) Smooth crater, $\alpha = 20°$ from right to left. (*b*) Ploughed crater, $\alpha = 40°$ from left to right. (*c*) Cut craters, $\alpha = 20°$ from right to left. (*d*) Sharp dent, $\alpha = 40°$ from left to right. Potential: 20 kV in all cases.

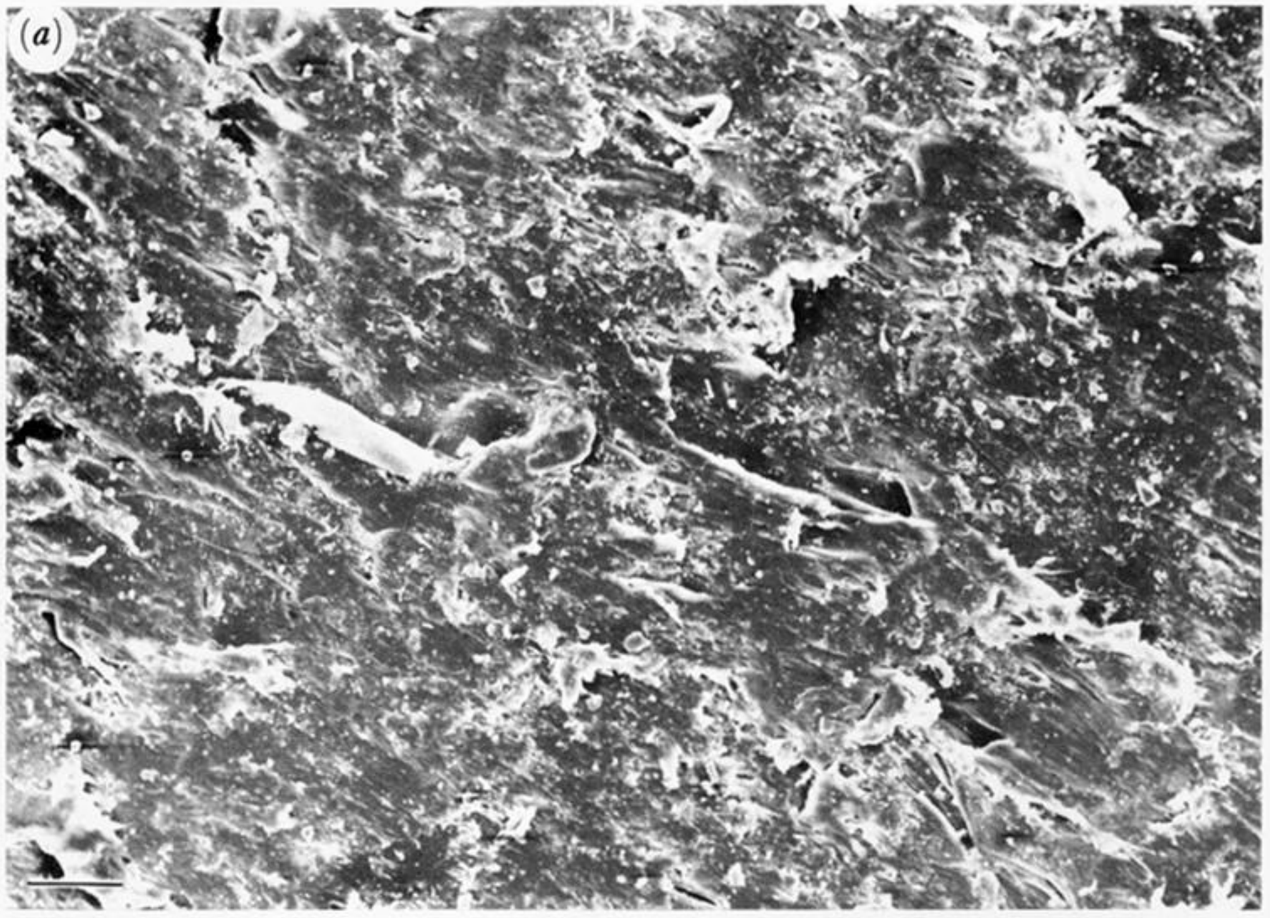

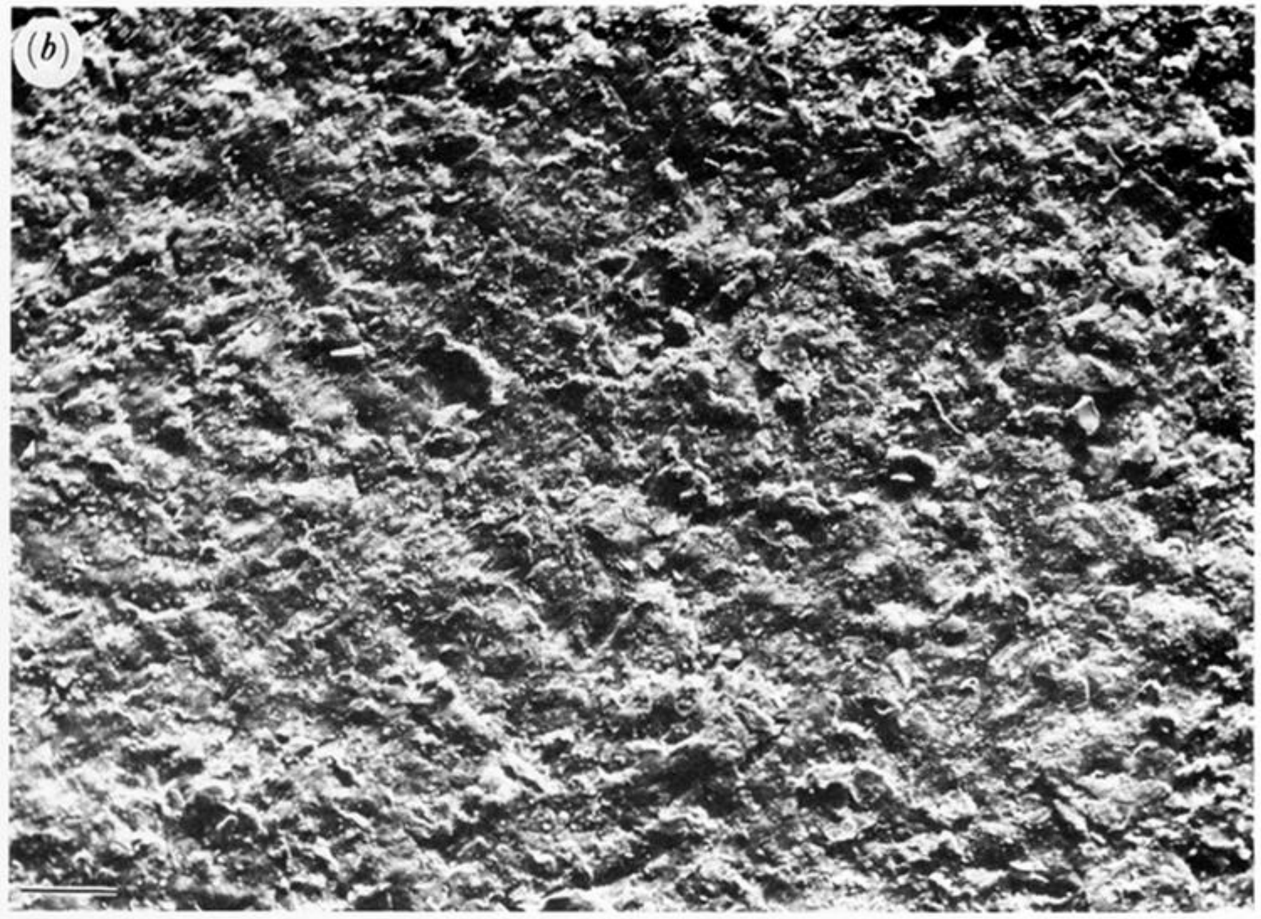

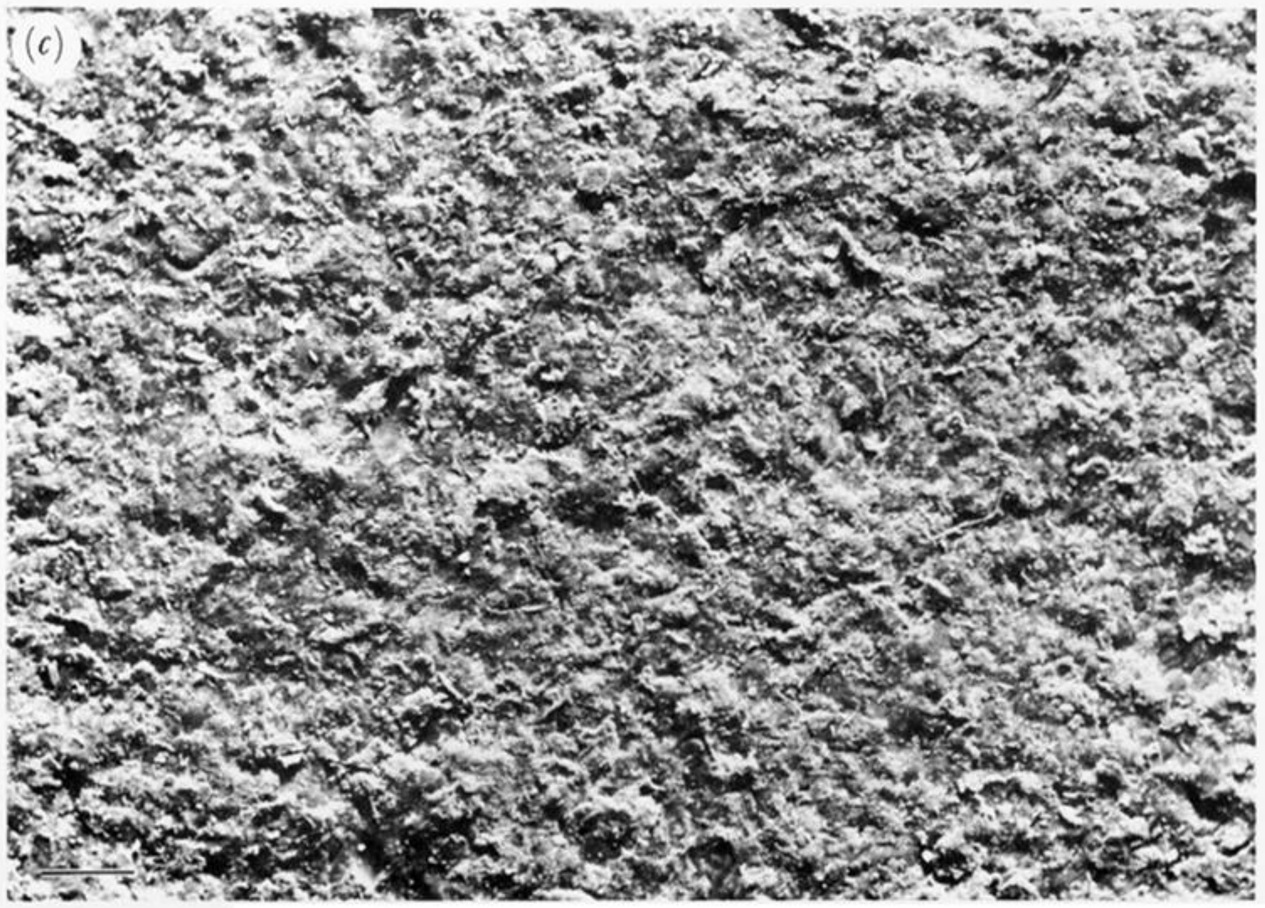

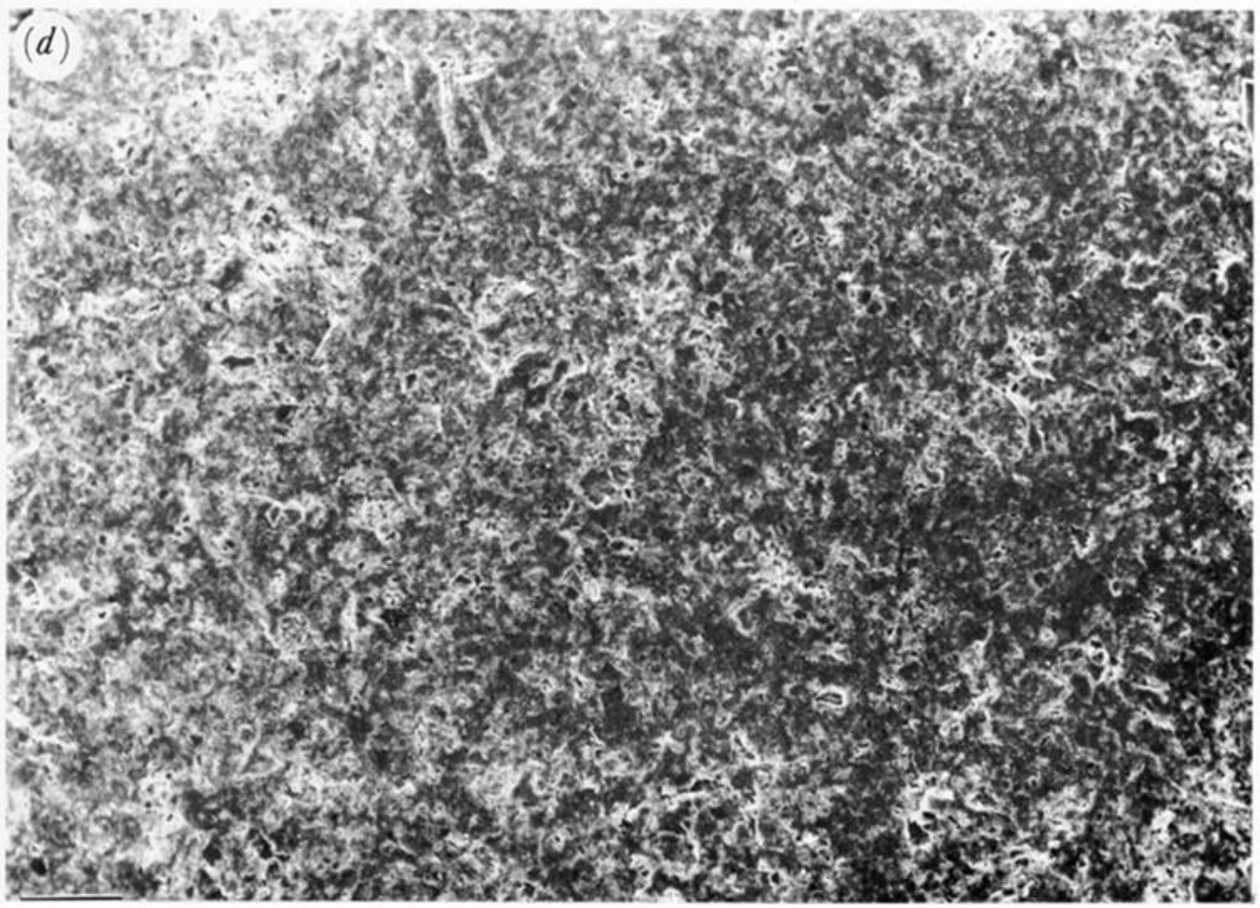

FIGURE 6. Electron micrographs of steady-state erosion surfaces produced by 300–600 μm sand at 36 ± 6 m s^{-1}. (*a*) $\alpha = 20°$, $t = 400$ s, scale bar represents 100 μm. (*b*) $\alpha = 40°$, $t = 700$ s, scale bar represents 200 μm. (*c*) $\alpha = 40°$, $t = 2000$ s, scale bar represents 200 μm. (*d*) $\alpha = 80°$, $t = 3000$ s, scale bar represents 100 μm. Potential: 20 kV in all cases.

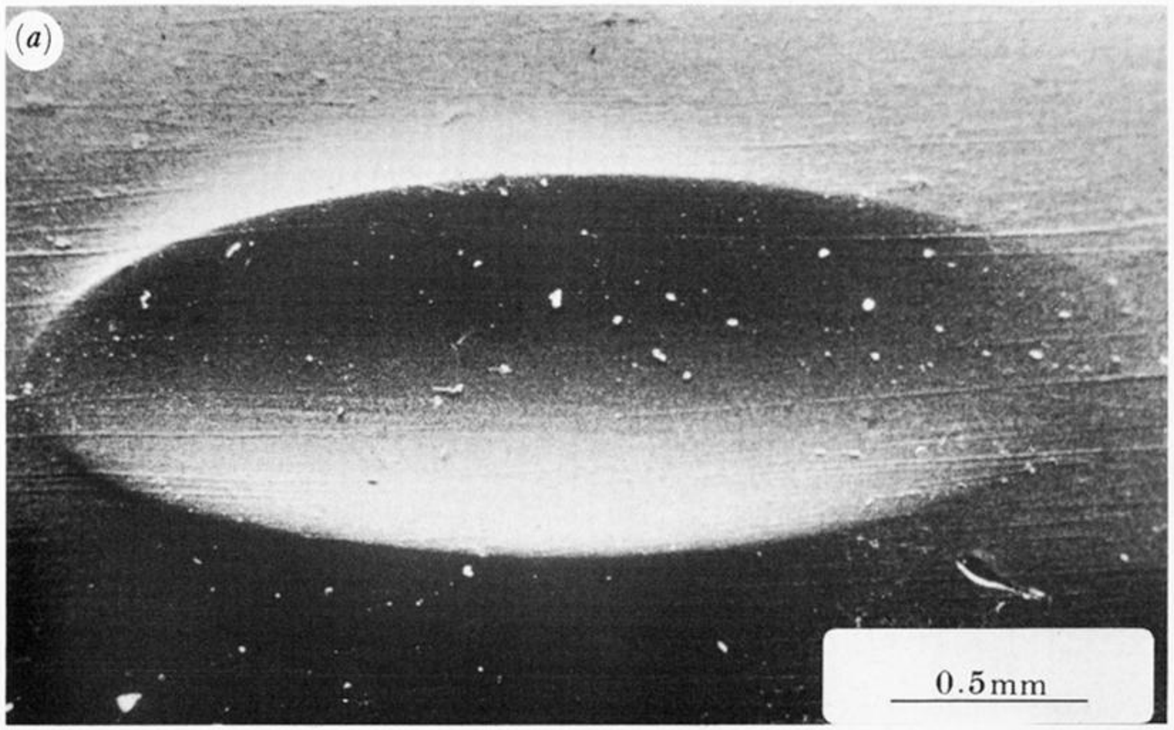

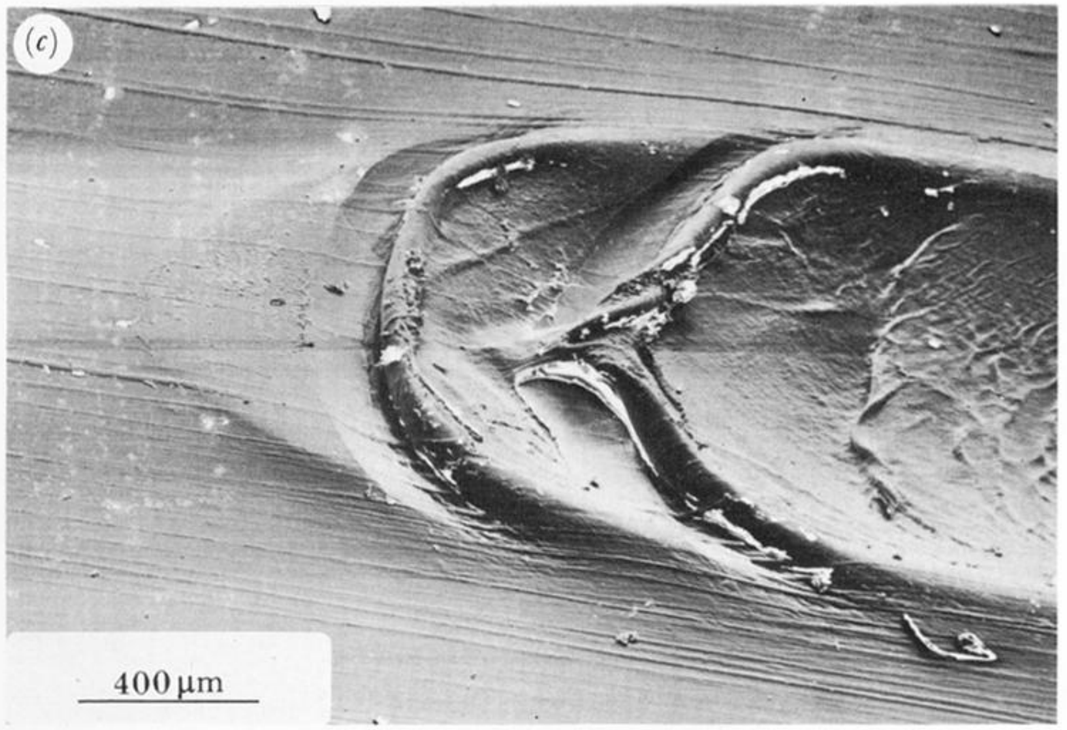

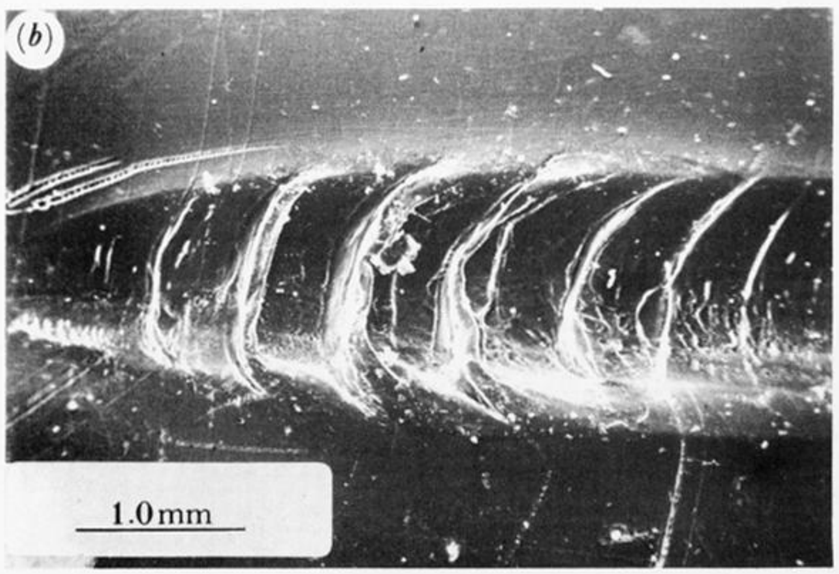

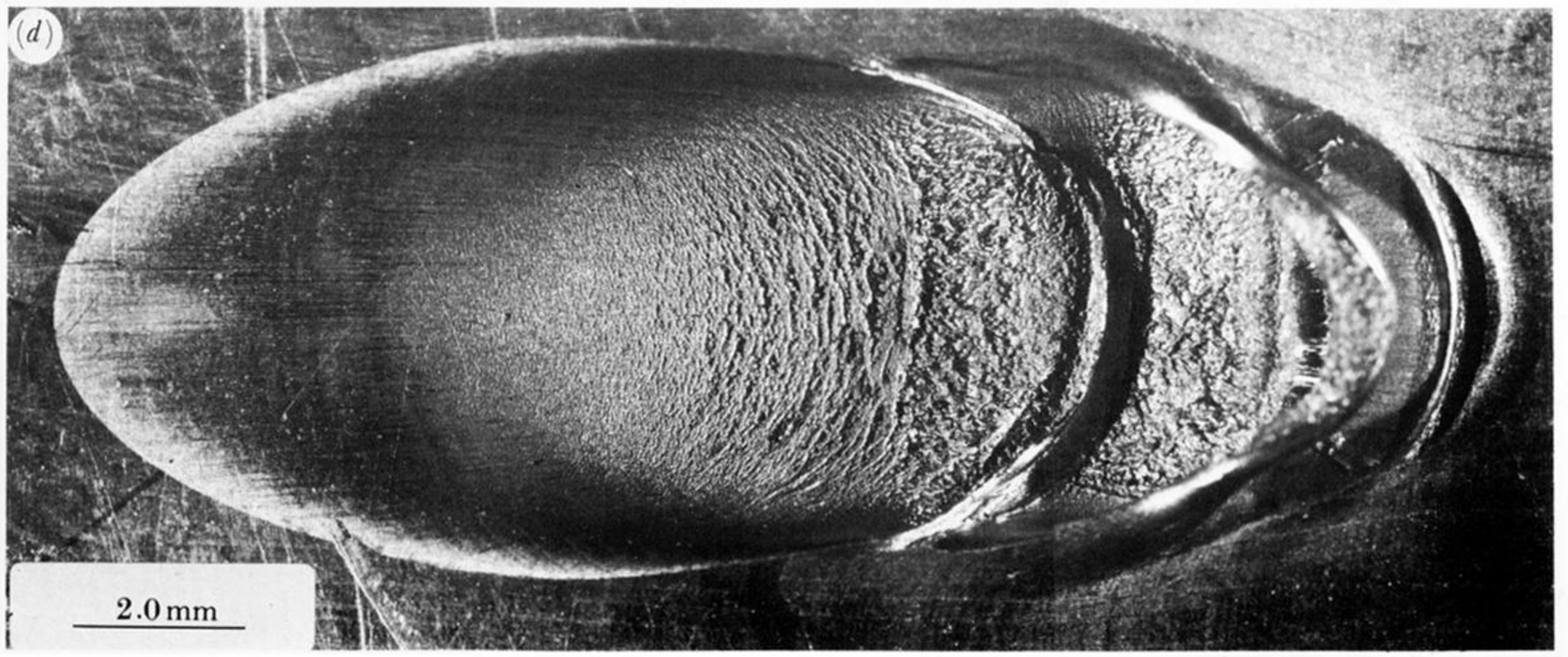

FIGURE 9. Examples of the types of craters mapped in figure 8. The pictures are electron micrographs unless otherwise stated. Diameters refer to the spheres. (*a*) Smooth. 2 mm diameter, impact from right to left: $v_i = 150$ m s^{-1}, $\alpha = 15°$. (*b*) Banded. 2 mm diameter, impact from right to left: $v_i = 260$ m s^{-1}, $\alpha = 10°$. (*c*) Banded. 2 mm diameter, 10 kV, impact from right to left: $v_i = 190$ m s^{-1}, $\alpha = 15°$. Note the impression of the bands on the material indicating relaxation has occurred. (*d*) Intermediate between banded and lipped. 8 mm diameter, impact from left to right: $v_i = 190$ m s^{-1}, $\alpha = 23°$. Optical picture. (*e*) Lipped crater. 4 mm diameter, impact from left to right: $v_i = 150$ m s^{-1}, $\alpha = 27°$. Optical picture. (*f*) Penetration. 4 mm diameter, impact from left to right: $v_i = 180$ m s^{-1}, $\alpha = 70°$. Optical picture. (*g*) Embedment. 4 mm diameter, 20 kV, impact from left to right: $v_i = 288$ m s^{-1}, $\alpha = 35°$. (See also figure 14.) (*h*) Embedment. 2 mm diameter, 20 kV, impact from left to right: $v_i = 260$ m s^{-1}, $\alpha = 70°$.

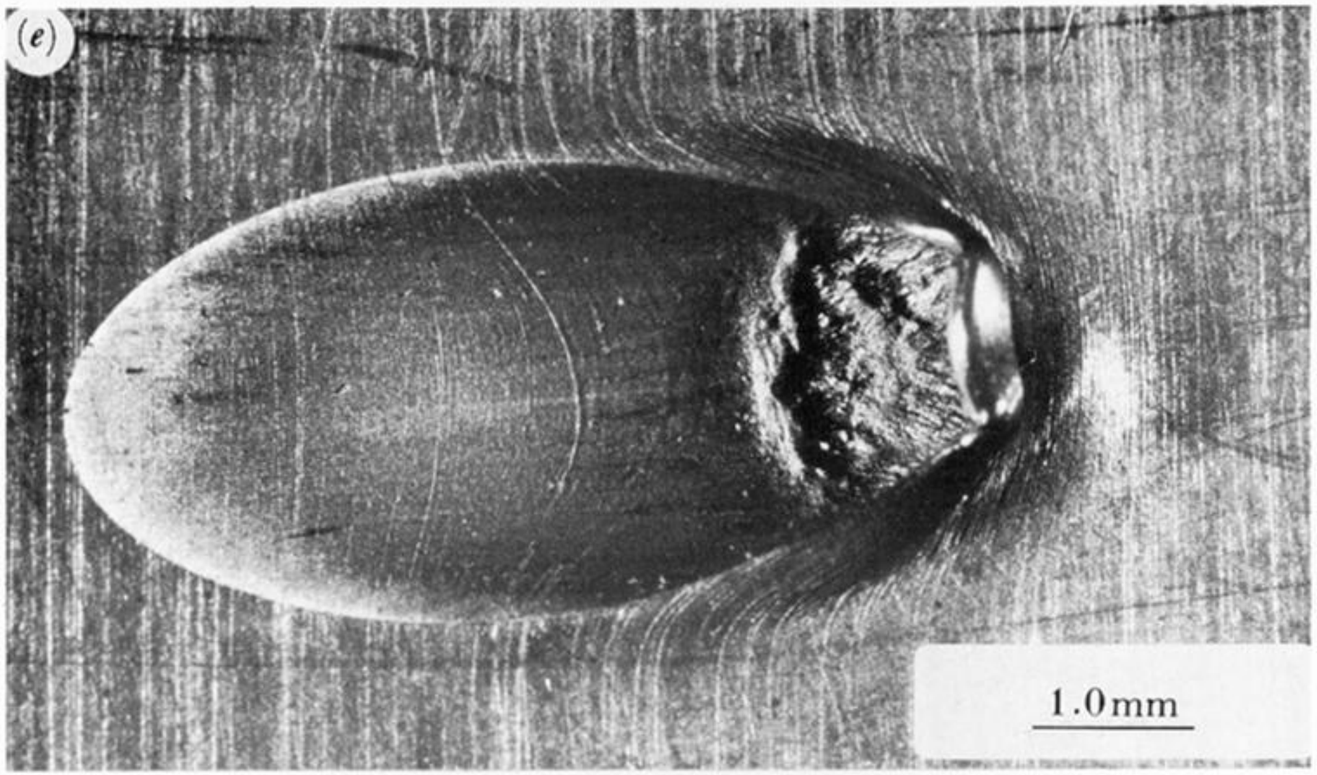
(e)
1.0mm

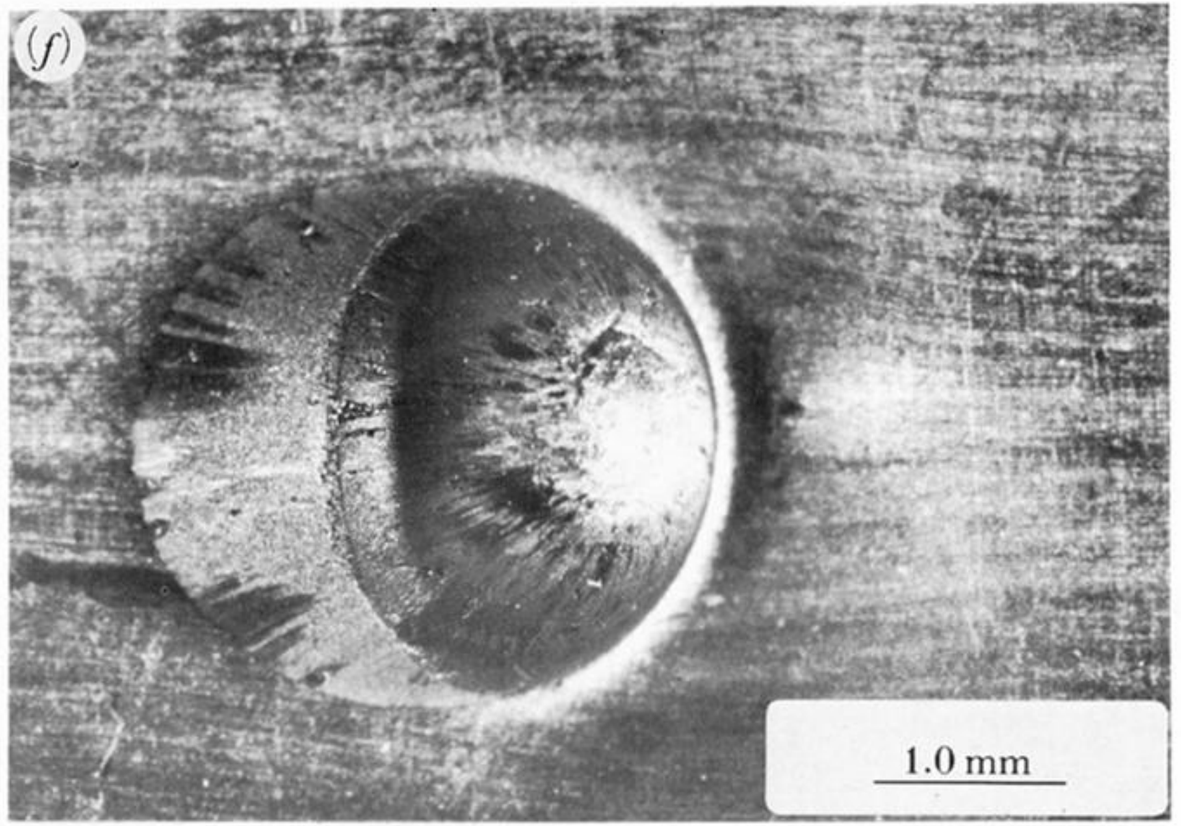
(f)
1.0 mm

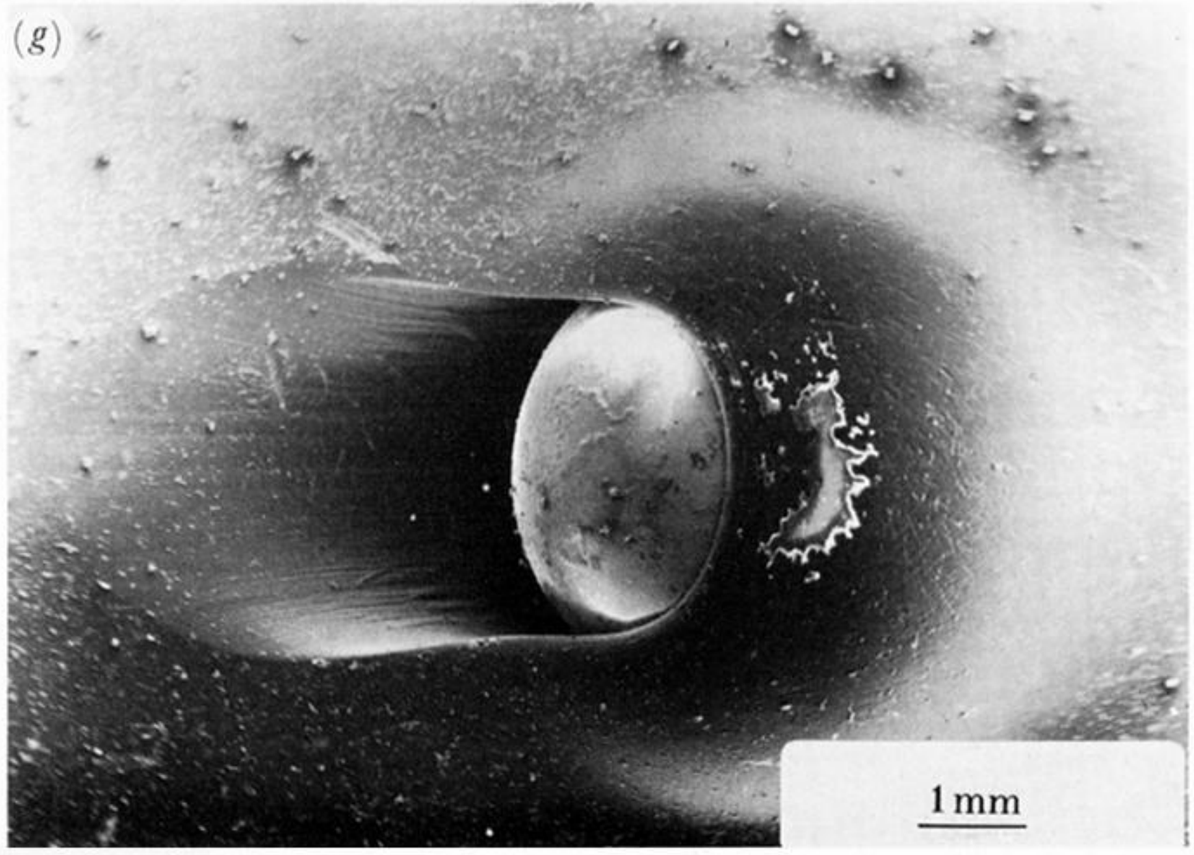
(g)
1mm

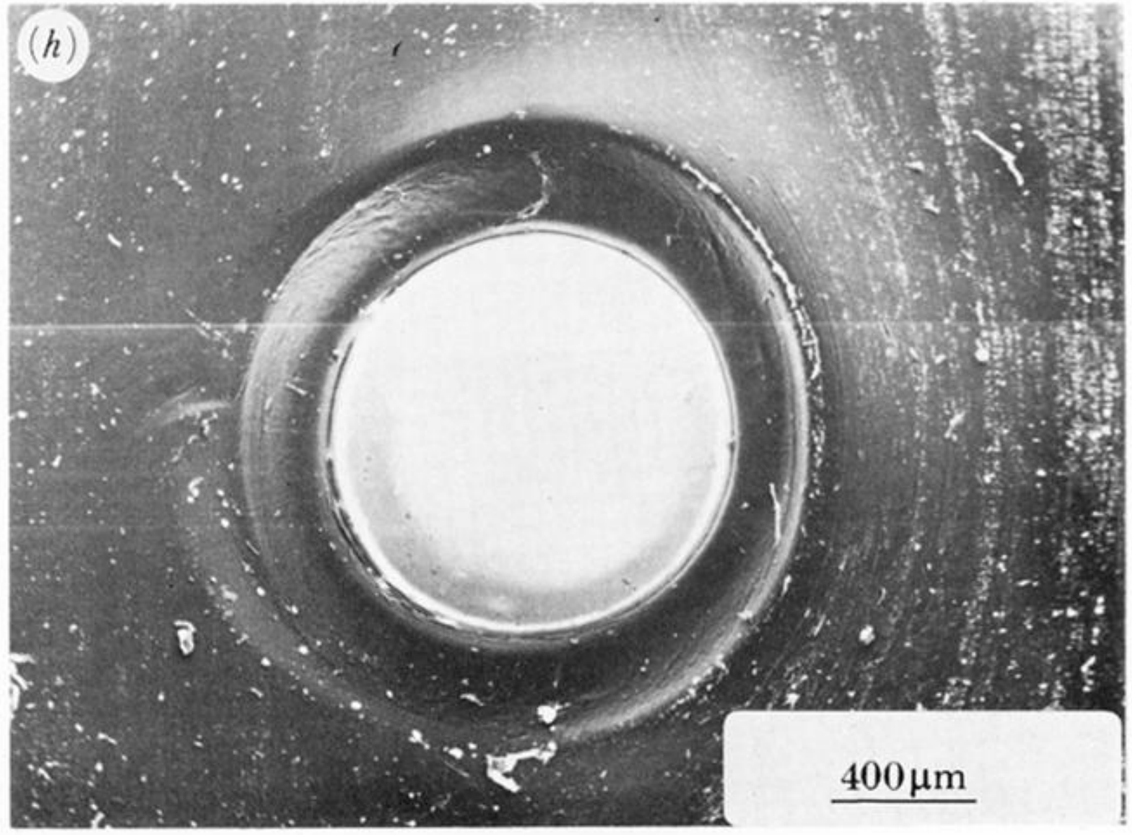
(h)
400μm

10*a*

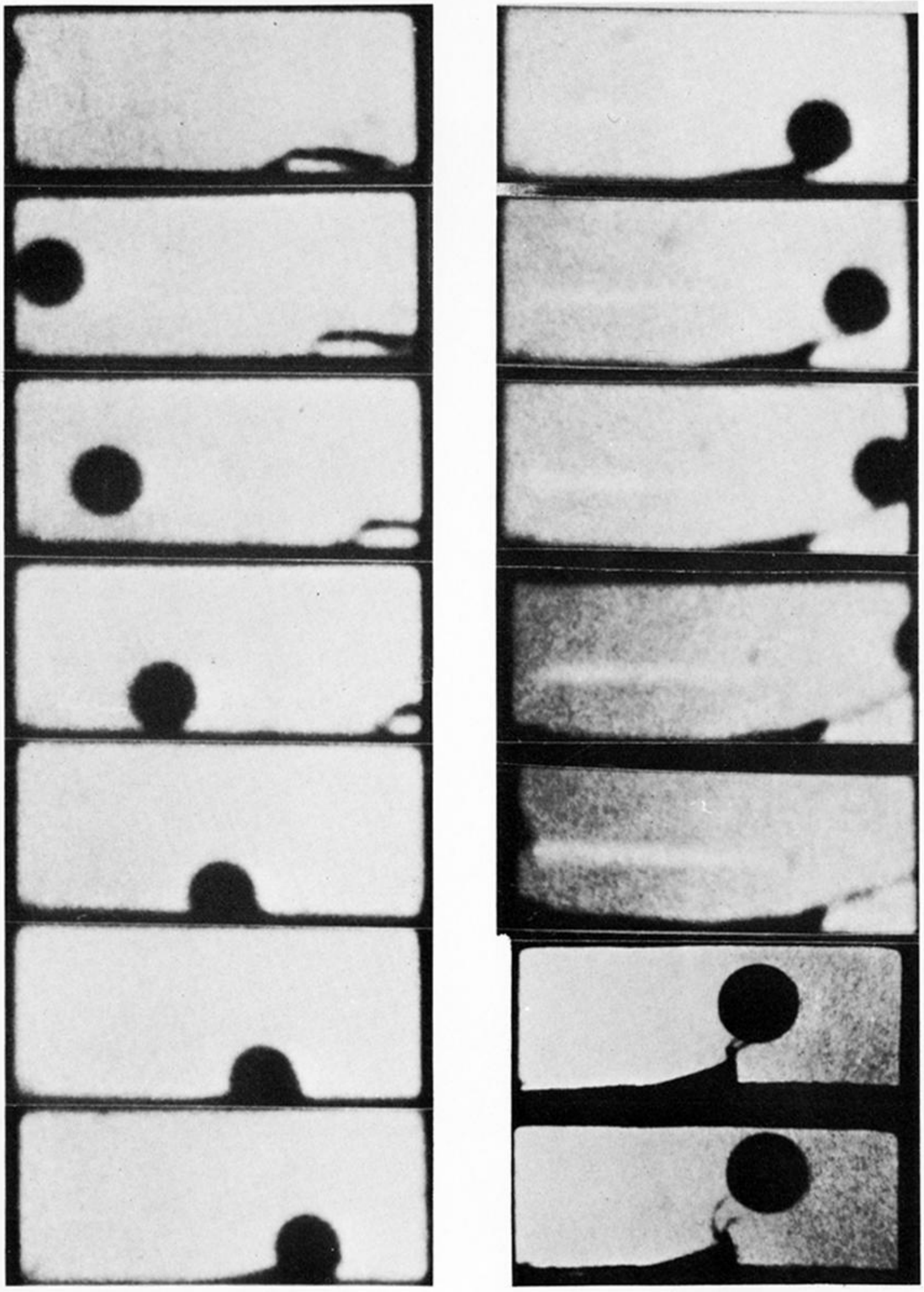

FIGURE 10. Frames (*a*)–(*l*), impact and rebound of a 4 mm diameter steel sphere that draws out a single filament. Interframe time: 19 μs. $v_i = 192$ m s^{-1}, $\alpha = 25°$; $v_r = 114$ m s^{-1}, $\beta = 27°$. Frames (*m*)–(*n*), last two frames of an impact that drew out two filaments. Interframe time: 17 μs. Sphere diameter: 5 mm. $v_i = 170 \pm 15$ m s^{-1}, $\alpha = 37°$; $v_r = 63 \pm 3$ m s^{-1}, $\beta = 47.5°$.

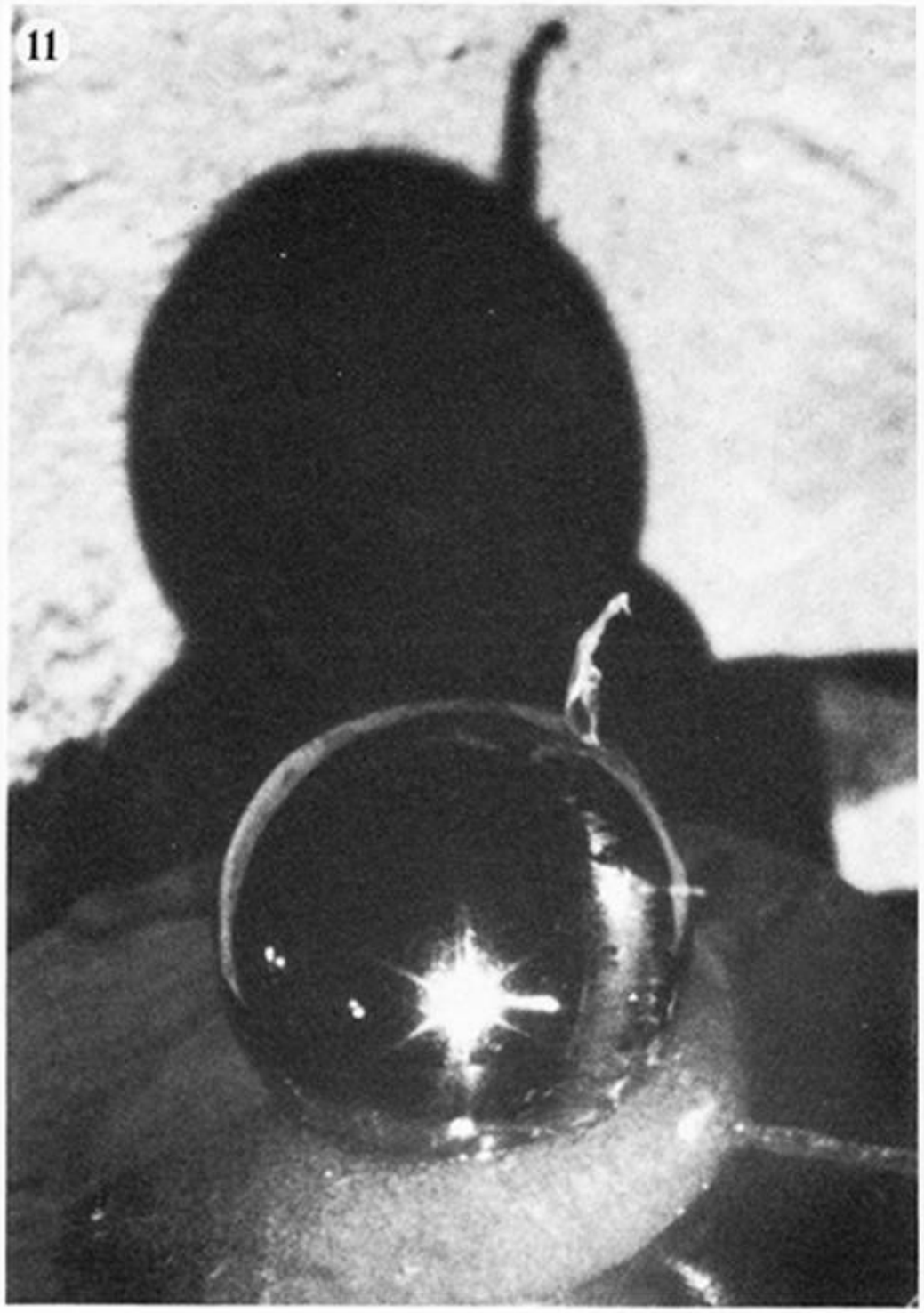

FIGURE 11. Optical picture of a filament that remained attached to a sphere after impact (ball diameter 5 mm). A shadow of the ball and filament appears in the background. $v_i = 170 \pm 15$ m s^{-1}, $\alpha = 36° \pm 4°$; $v_r = 64$ m s^{-1}, $\beta = 40°$.

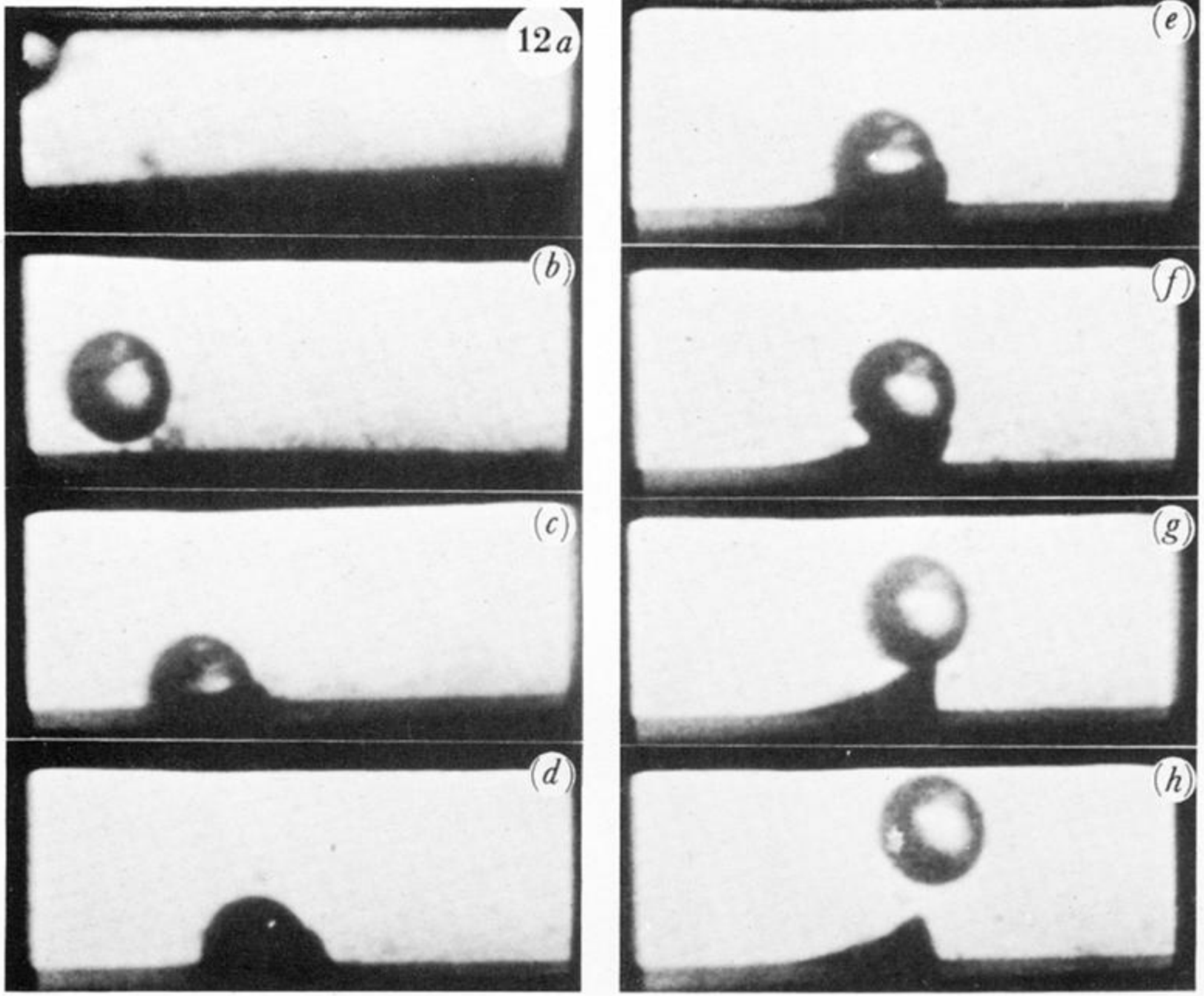

FIGURE 12. Impact and rebound of a 5 mm-diameter glass sphere. Note the rapid spring back of the lip material between frames (*e*) and (*g*). Interframe time: 17 μs. $v_i = 280$ m s^{-1}, $\alpha = 30°$; $v_r = 100 \pm 3$ m s^{-1}, $\beta = 54° \pm 2°$.

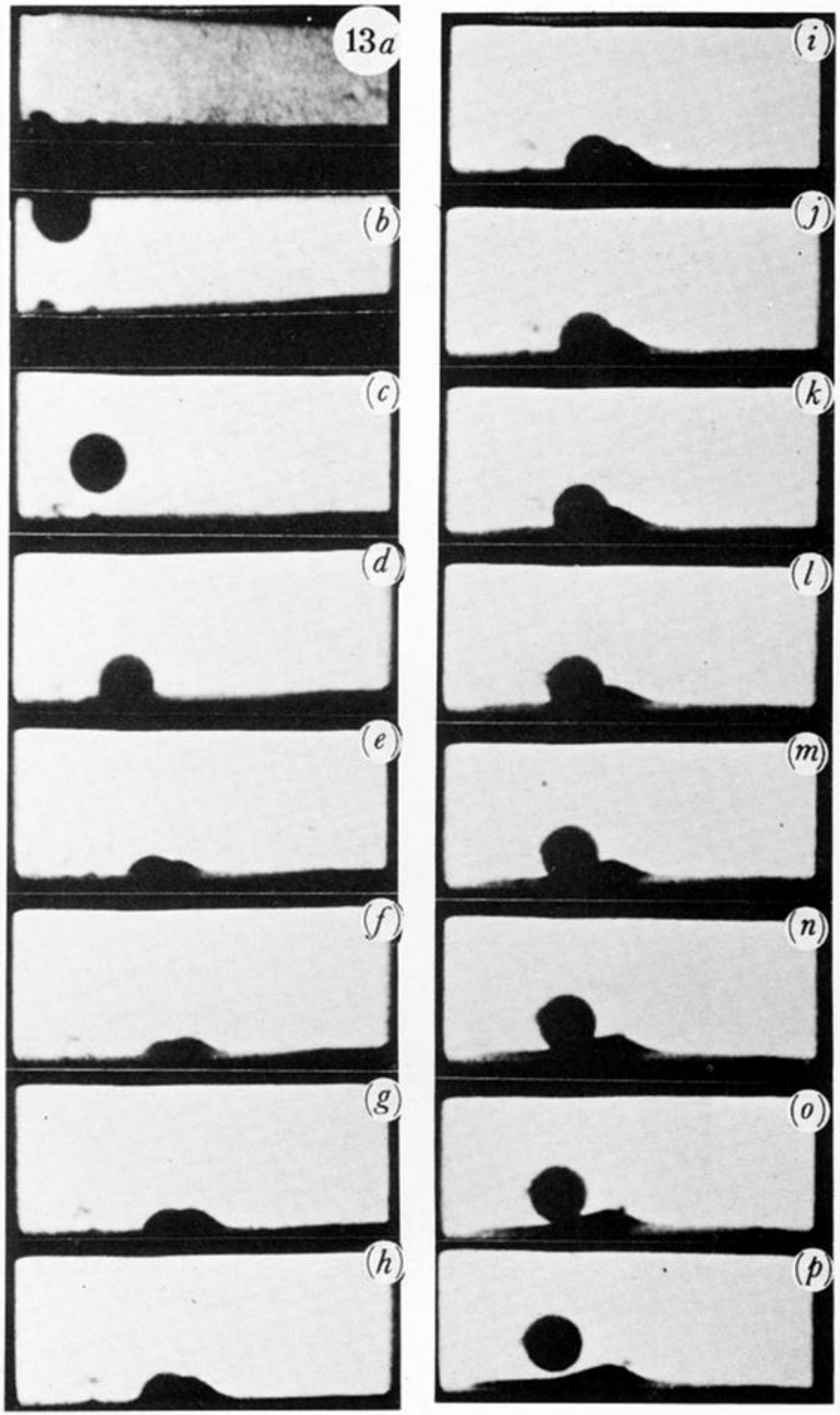

FIGURE 13. Penetrative impact by a 4 mm diameter steel sphere. Note that the ball comes out backwards. Interframe time: 17 μs. $v_i = 203 \pm 10$ m s^{-1}, $\alpha = 51.5° \pm 0.5°$; $v_r = 24$ m s^{-1}, $\beta = 135°$.

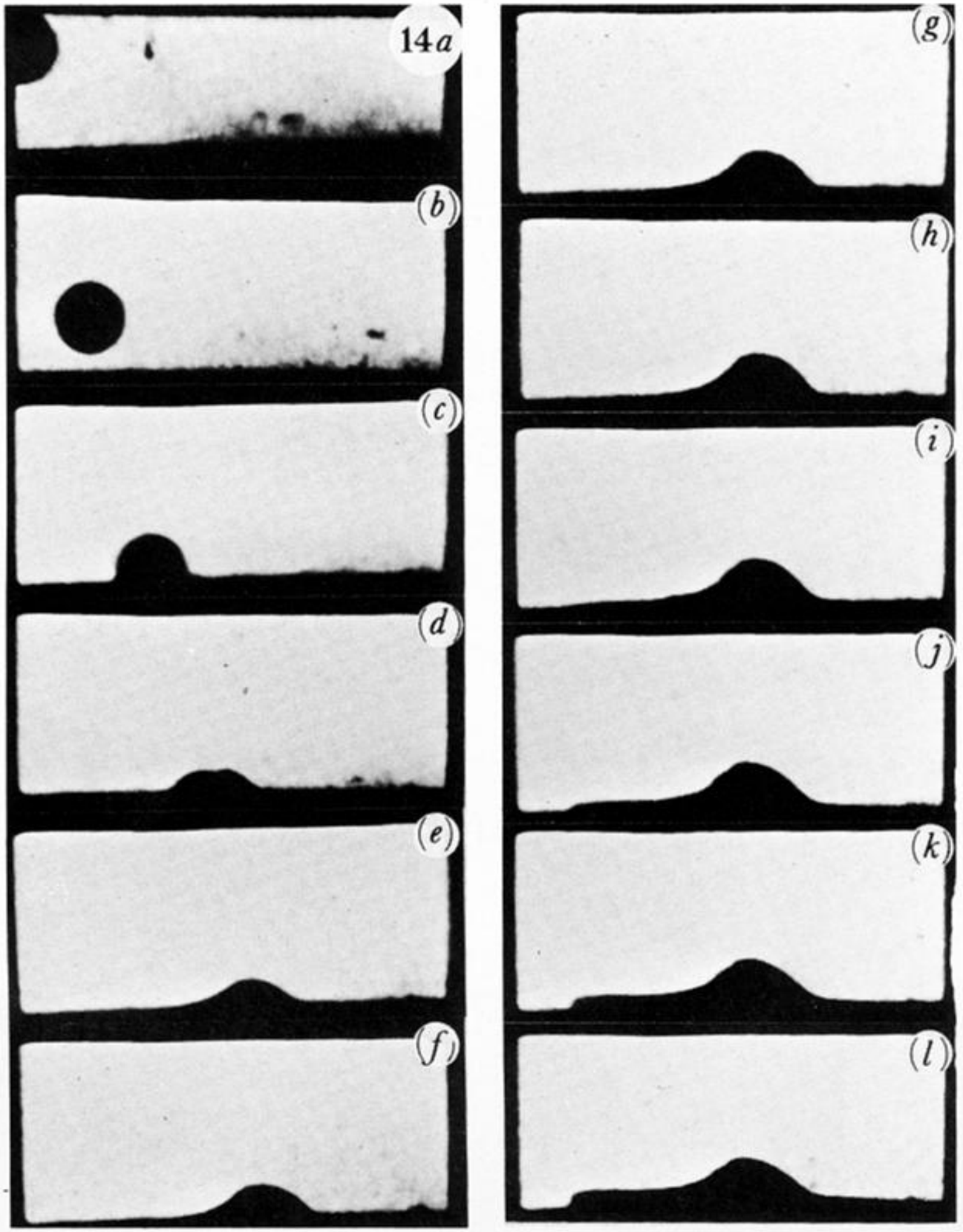

FIGURE 14. Example of embedment by a 4 mm diameter steel sphere. Interframe time: 17 μs. See also figure 9*g*. $v_i = 288$ m s^{-1}, $\alpha = 35°$.

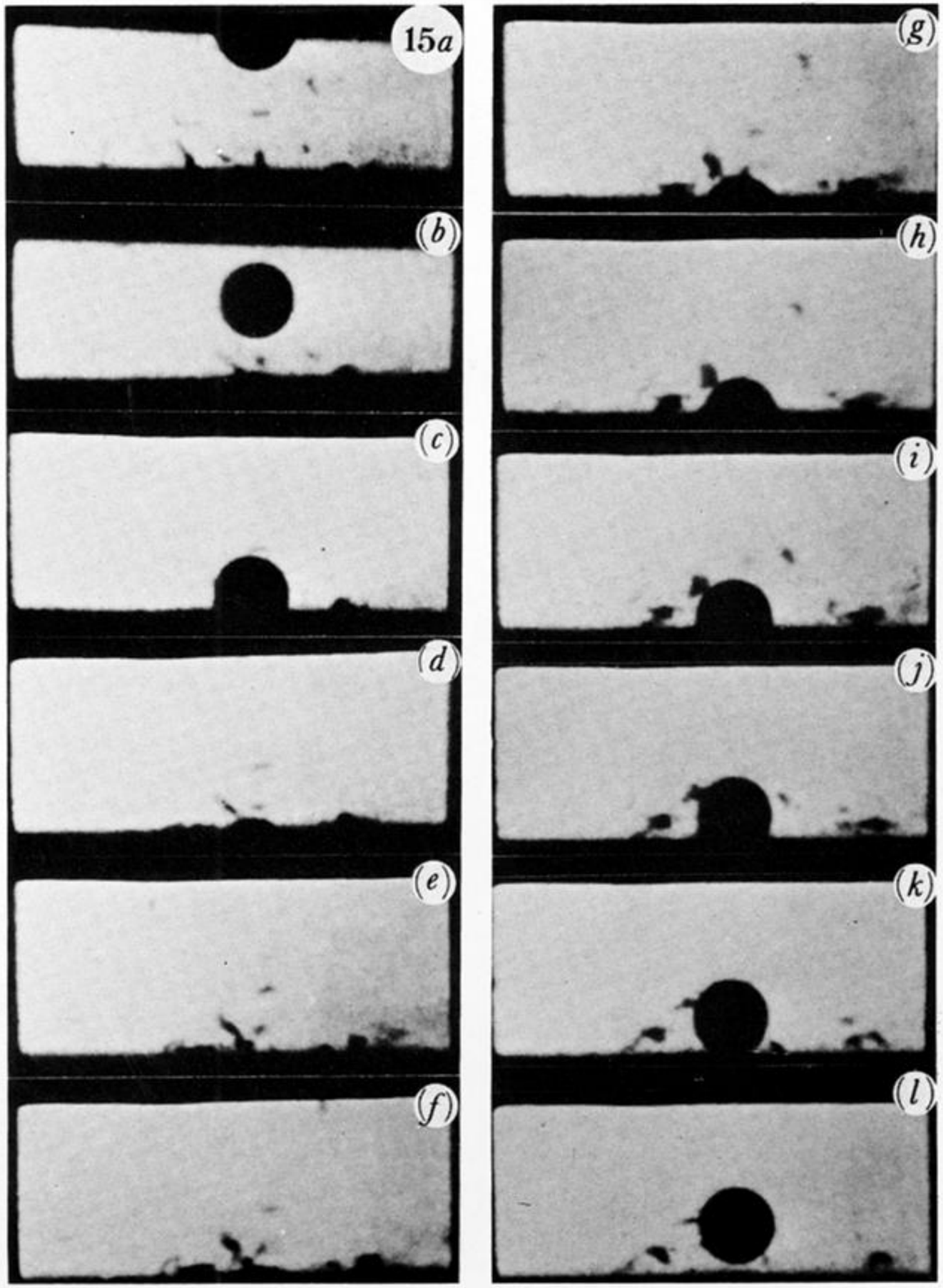

FIGURE 15. Normal impact by a 4 mm diameter steel sphere where the ball rebounds even after entering to a depth greater than its diameter. Interframe time: 17 μs. 10 mm thick specimen. $v_i = 194$ m s^{-1}, $v_r = 45$ m s^{-1}.

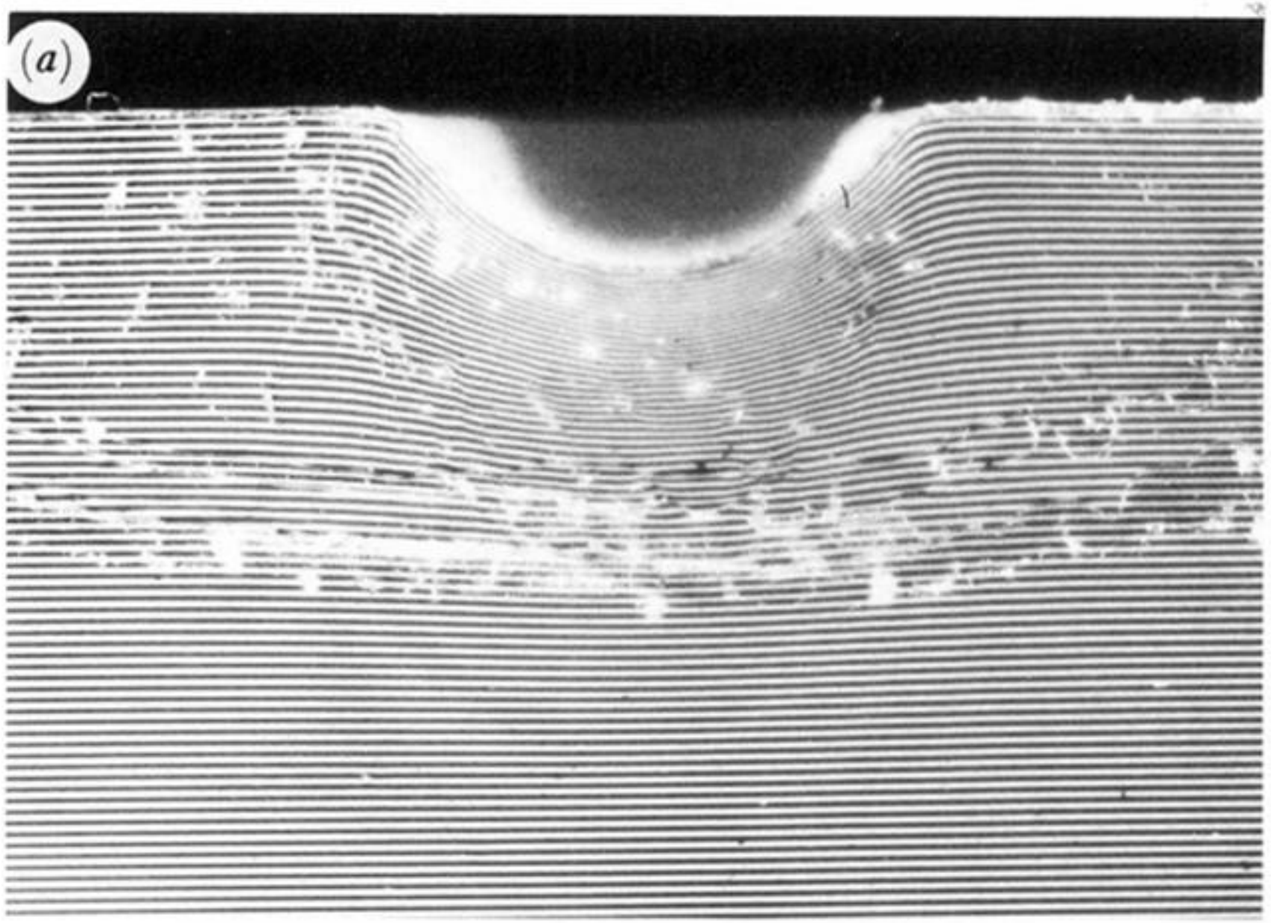

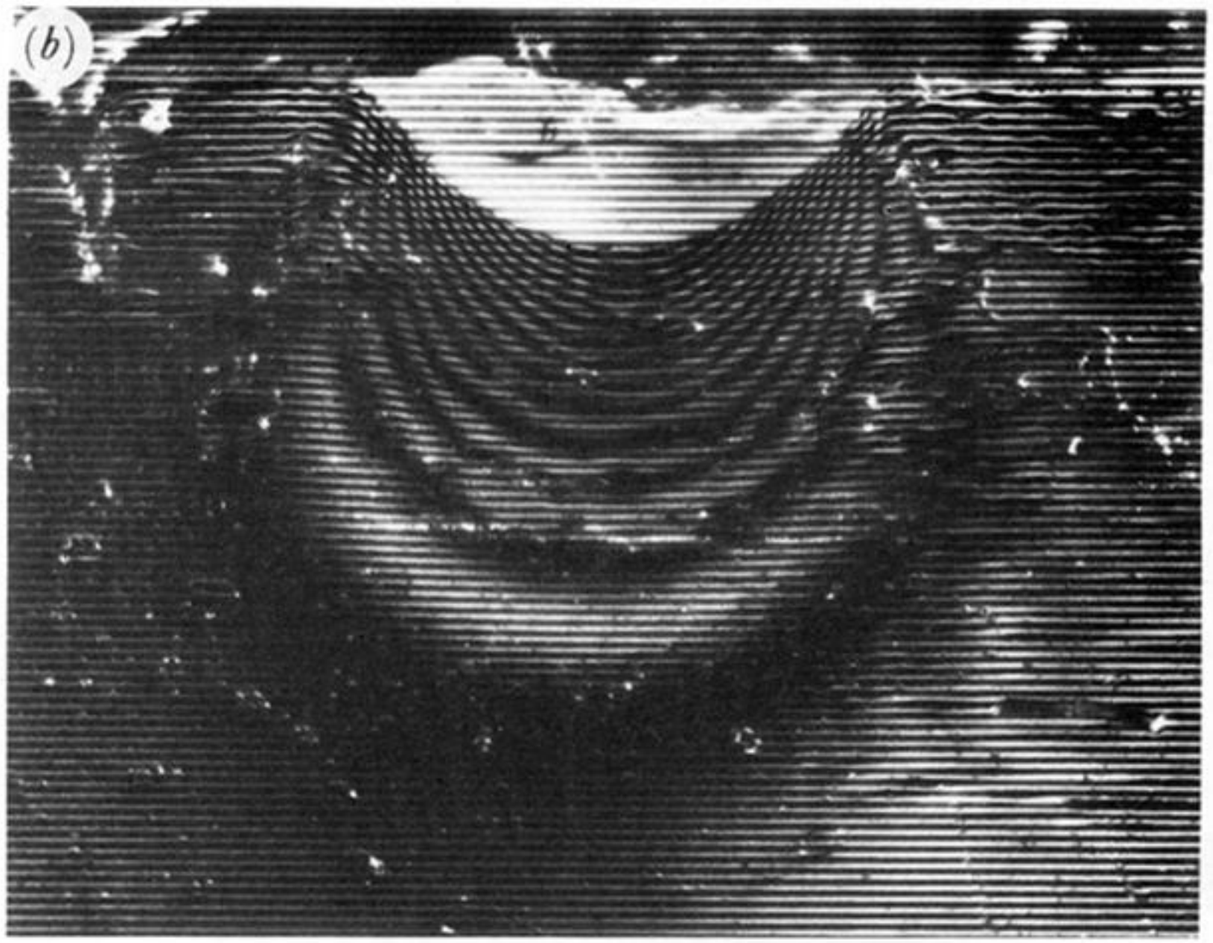

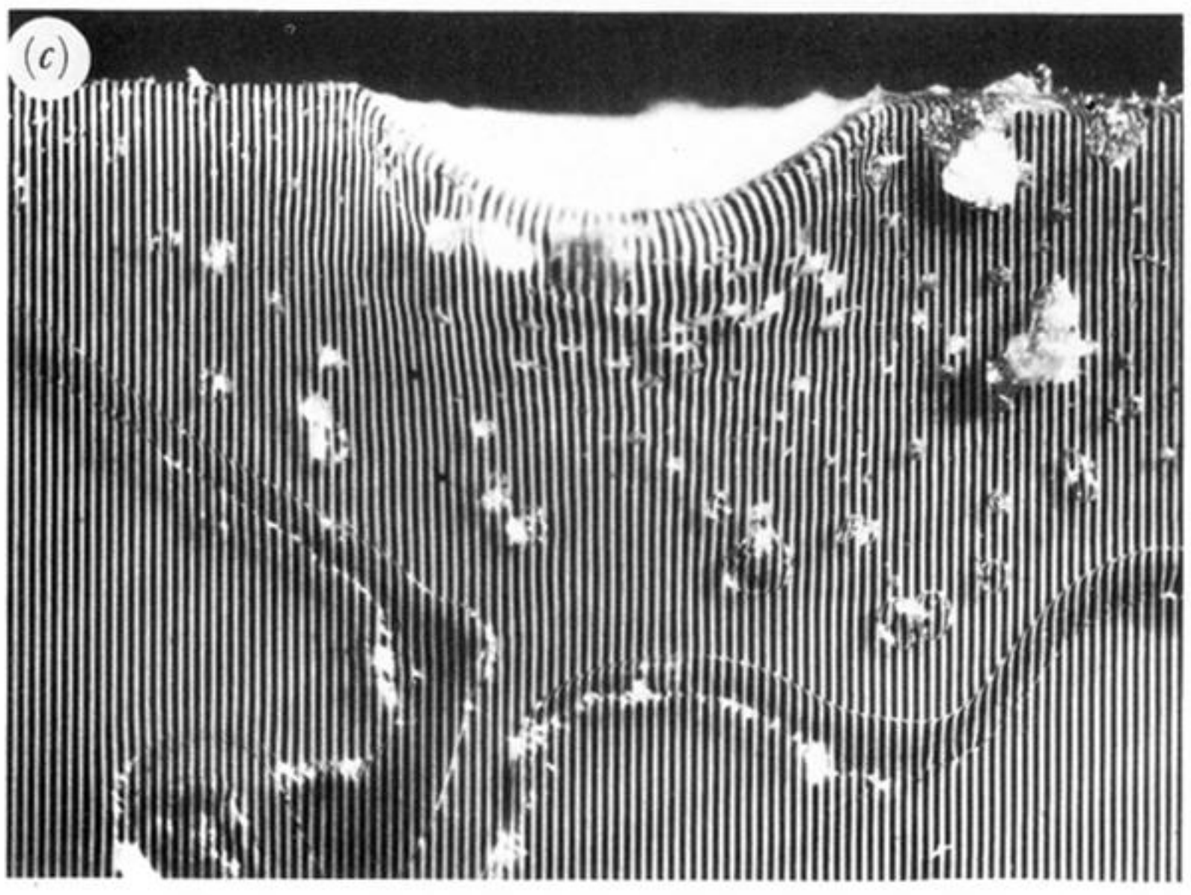

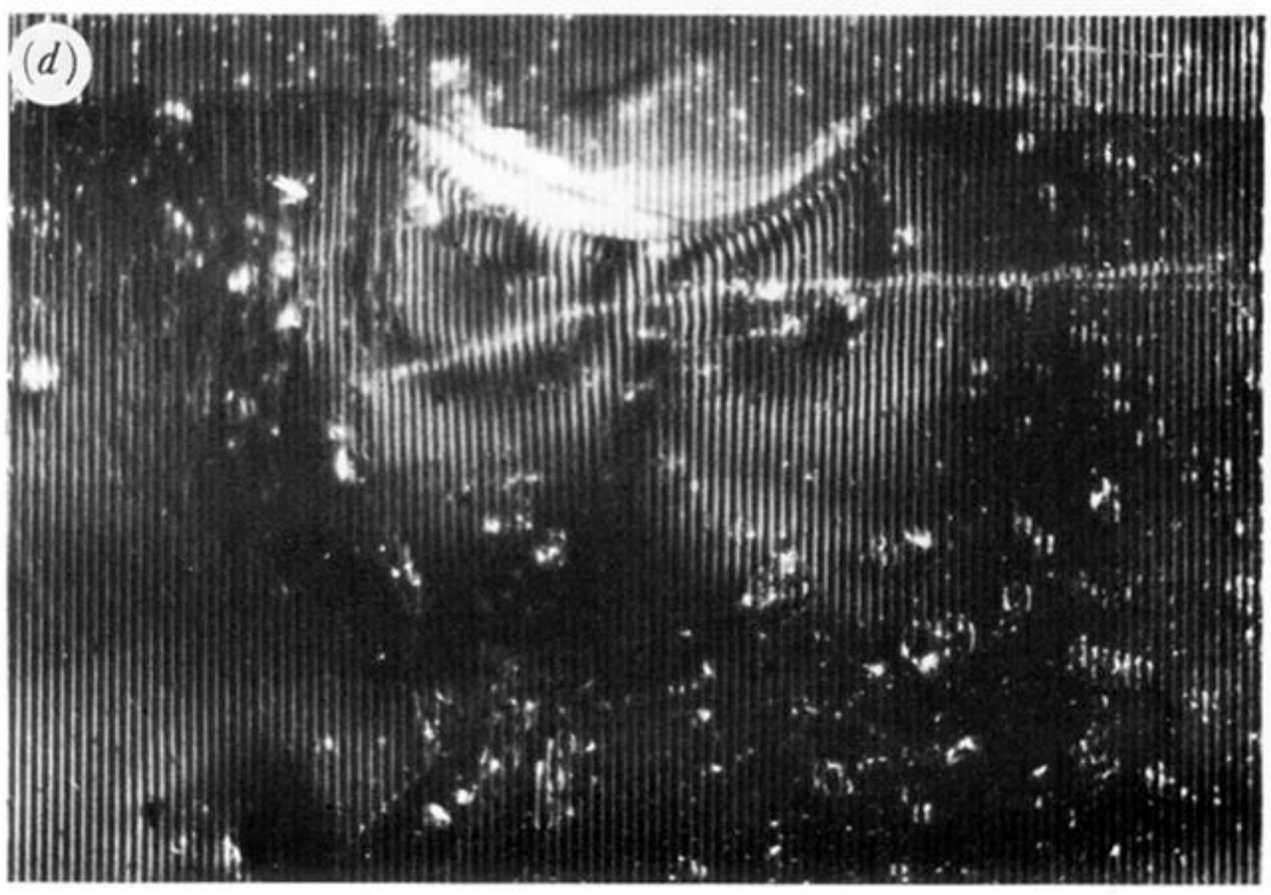

FIGURE 25*a–d*. For description see opposite.

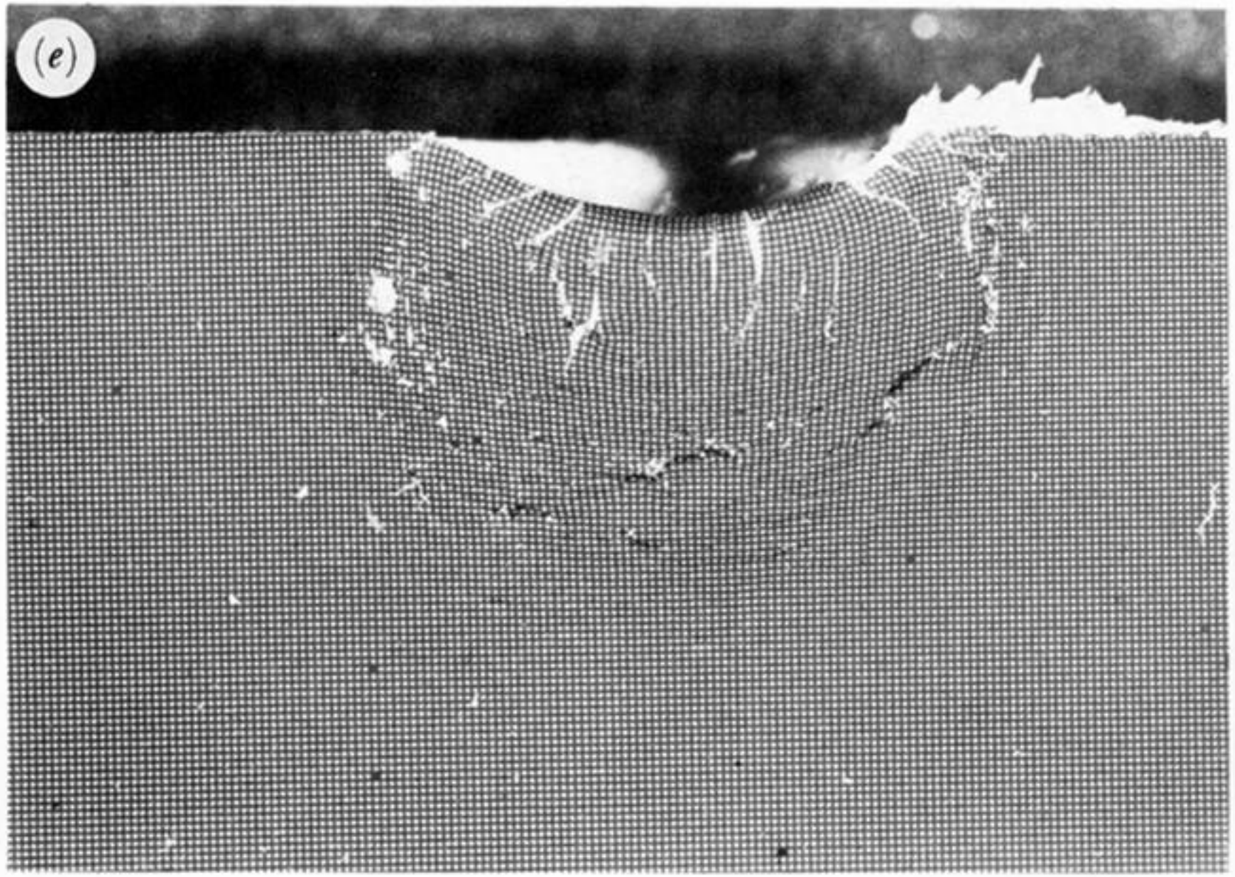

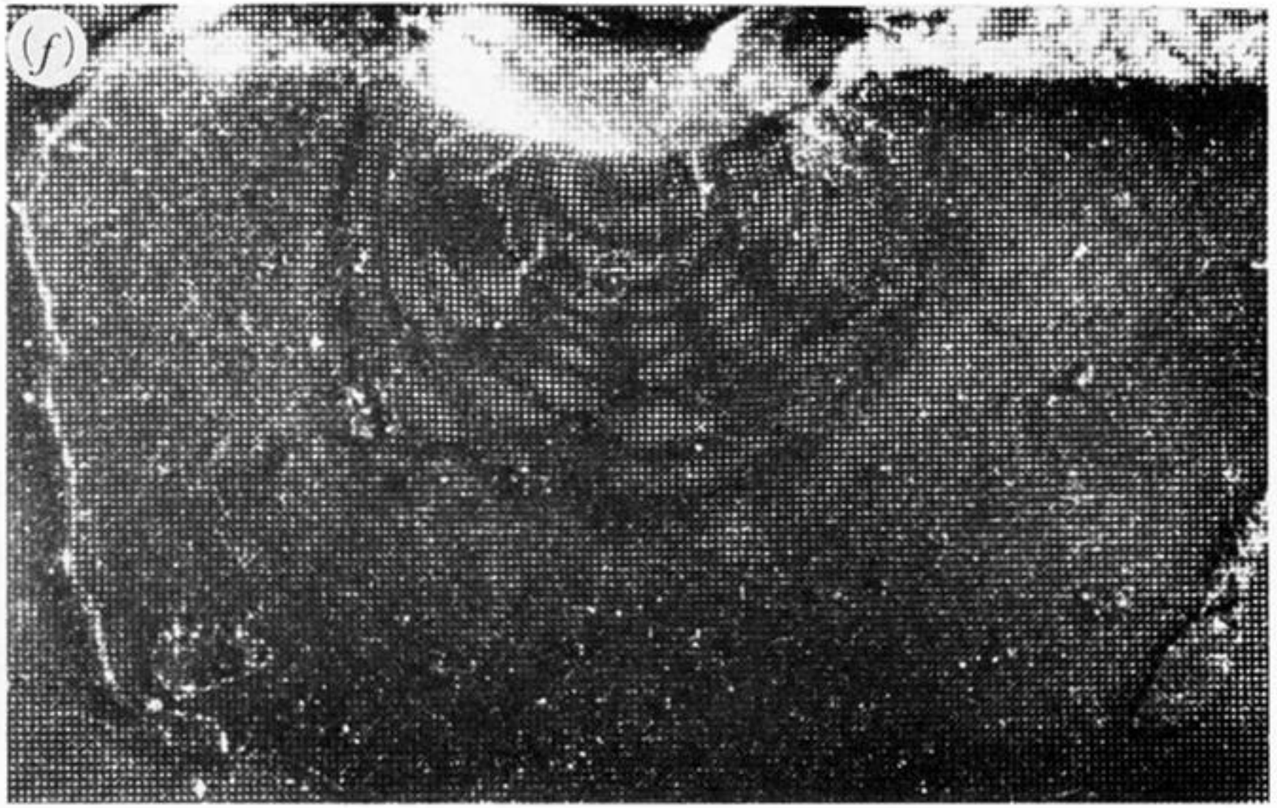

FIGURE 25. (*a*) Deformed horizontal line grating beneath an indentation by a 4 mm diameter sphere. Line spacing: 85 μm. (*b*) Moiré fringes formed by laying a reference grating on top of the specimen shown in (*a*). (*c*) Deformed vertical line grating beneath another indentation by a 4 mm diameter sphere. (*d*) Moiré fringes formed from (*c*) with a reference grating. (*e*) Deformed 2D grating beneath a 6 mm diameter steel sphere impact; $v_i = 124 \pm 4$ m s^{-1}, $v_r = 32$ m s^{-1}; kinetic energy dissipated: 6.3 J. (*f*) Two-dimensional displacement pattern formed from the specimen of (*e*) with a crossed reference grating.

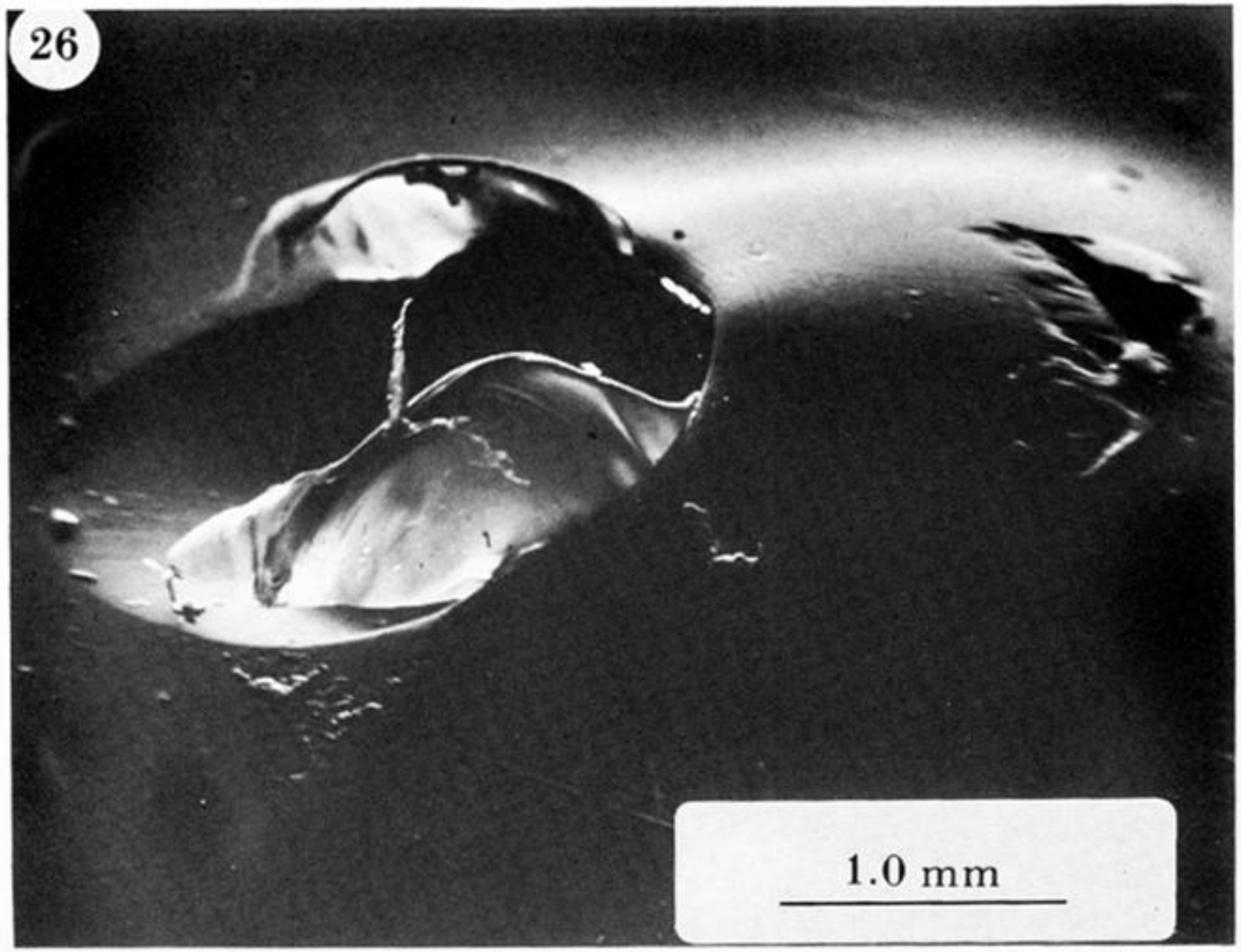

FIGURE 26. Possible example of melting caused by the impact of a 2 mm-diameter steel sphere from left to right. Ball embedded but fell out before the electron micrograph was taken; $v_i = 240$ m s^{-1}, $\alpha = 40°$.

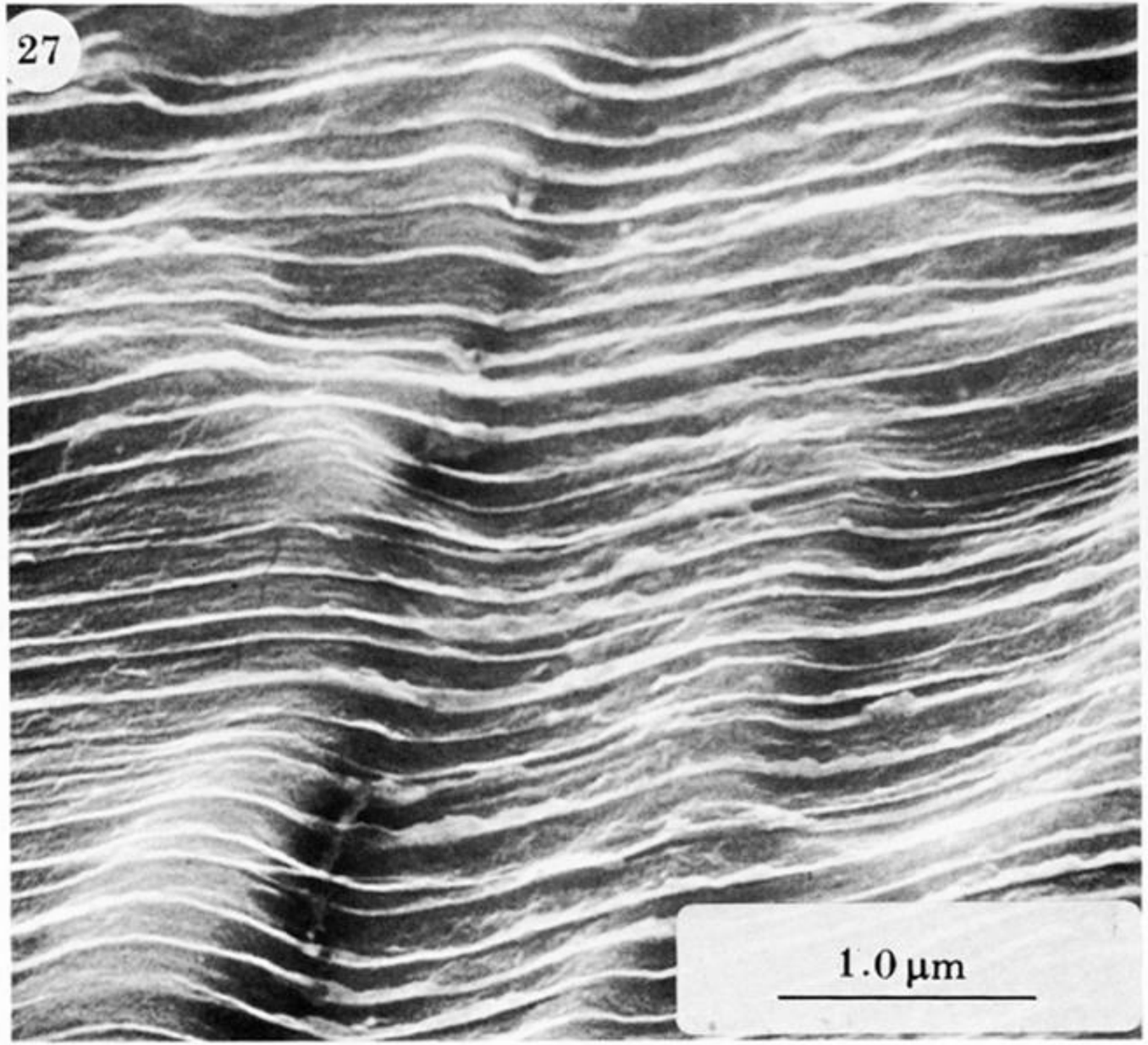

FIGURE 27. Electron micrograph of the highly sheared surface from near the crater exit of a 2 mm-diameter steel sphere impact site; $v_i = 110$ m s^{-1}, $\alpha = 25°$.

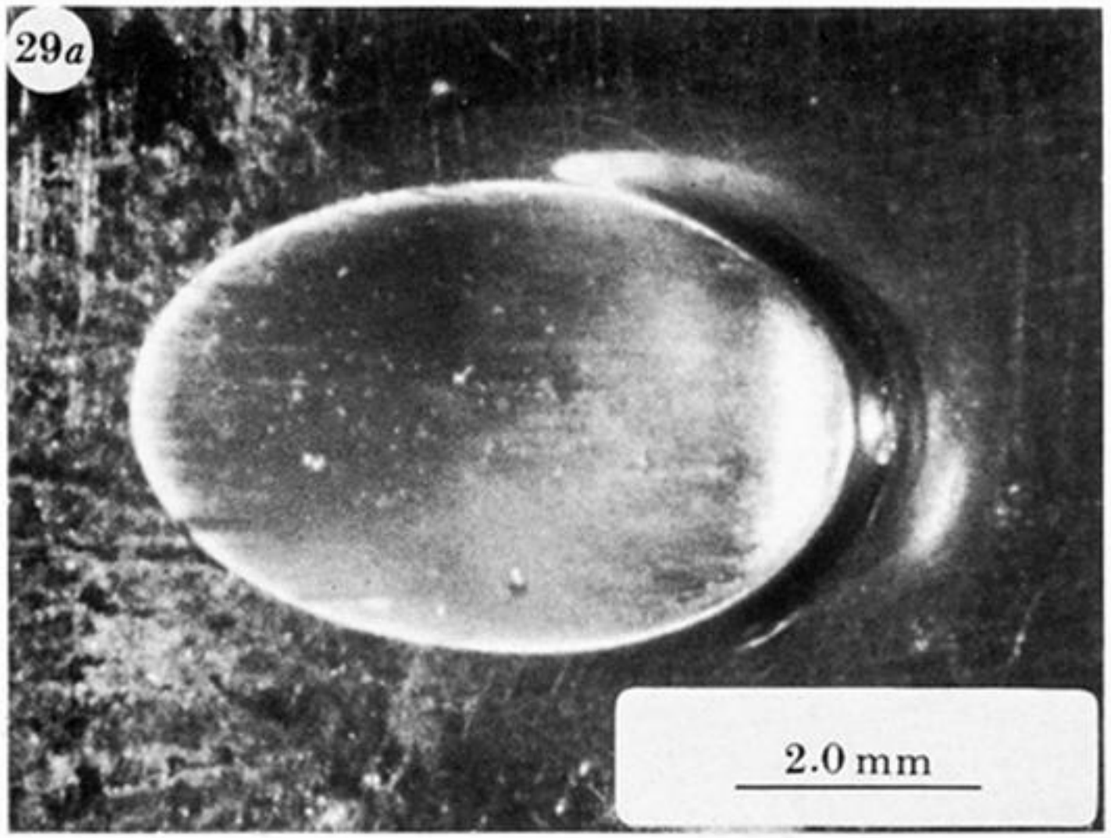

FIGURE 29. Optical pictures comparing oblique impact craters formed by 5 mm steel and glass spheres with similar kinetic energies. (*a*) Steel: $v_i = 128 \pm 7$ m s^{-1}, $\alpha = 39.5°$; $v_r = 62$ m s^{-1}, $\beta = 34°$; $E_{Ki} = 4.17$ J; $E_{Kr} = 0.98$ J; $\Delta E_K = 3.19$ J. (*b*) Glass: $v_i = 222$ m s^{-1}, $\alpha = 39°$; $v_r = 105 \pm 8$ m s^{-1}, $\beta = 43 \pm 4°$; $E_{Ki} = 4.24$ J; $E_{Kr} = 0.95$ J; $\Delta E_K = 3.29$ J.

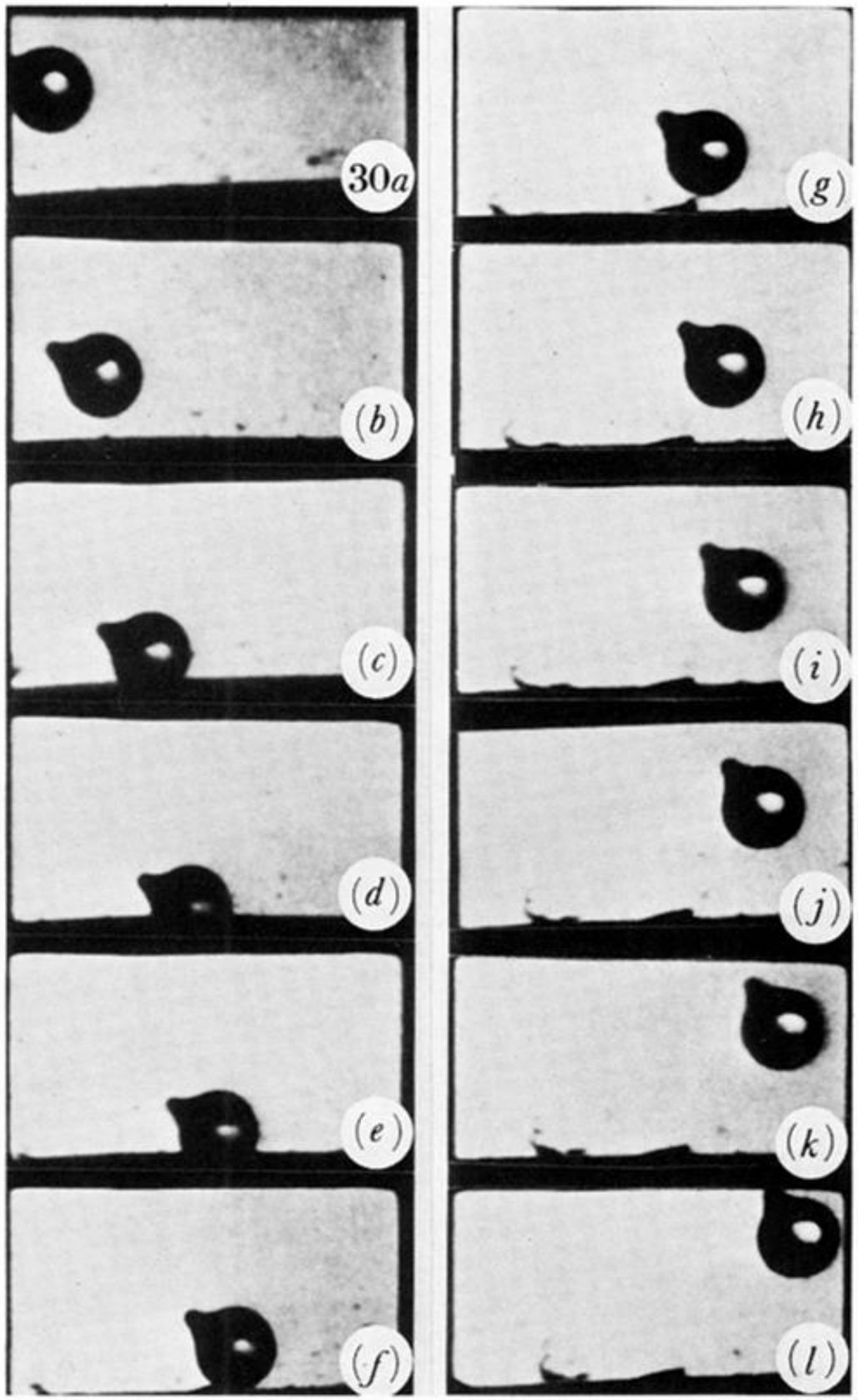

FIGURE 30. High-speed photographic sequence showing rotation imparted to a tagged glass sphere. Interframe time: 17 μs. Rotation imparted: 3° per 17 μs (3.1 krad s^{-1}). $v_i = 238 \pm 7$ m s^{-1}, $\alpha = 38 \pm 1°$; $v_r = 102 \pm 2$ m s^{-1}, $\beta = 42 \pm 1°$.

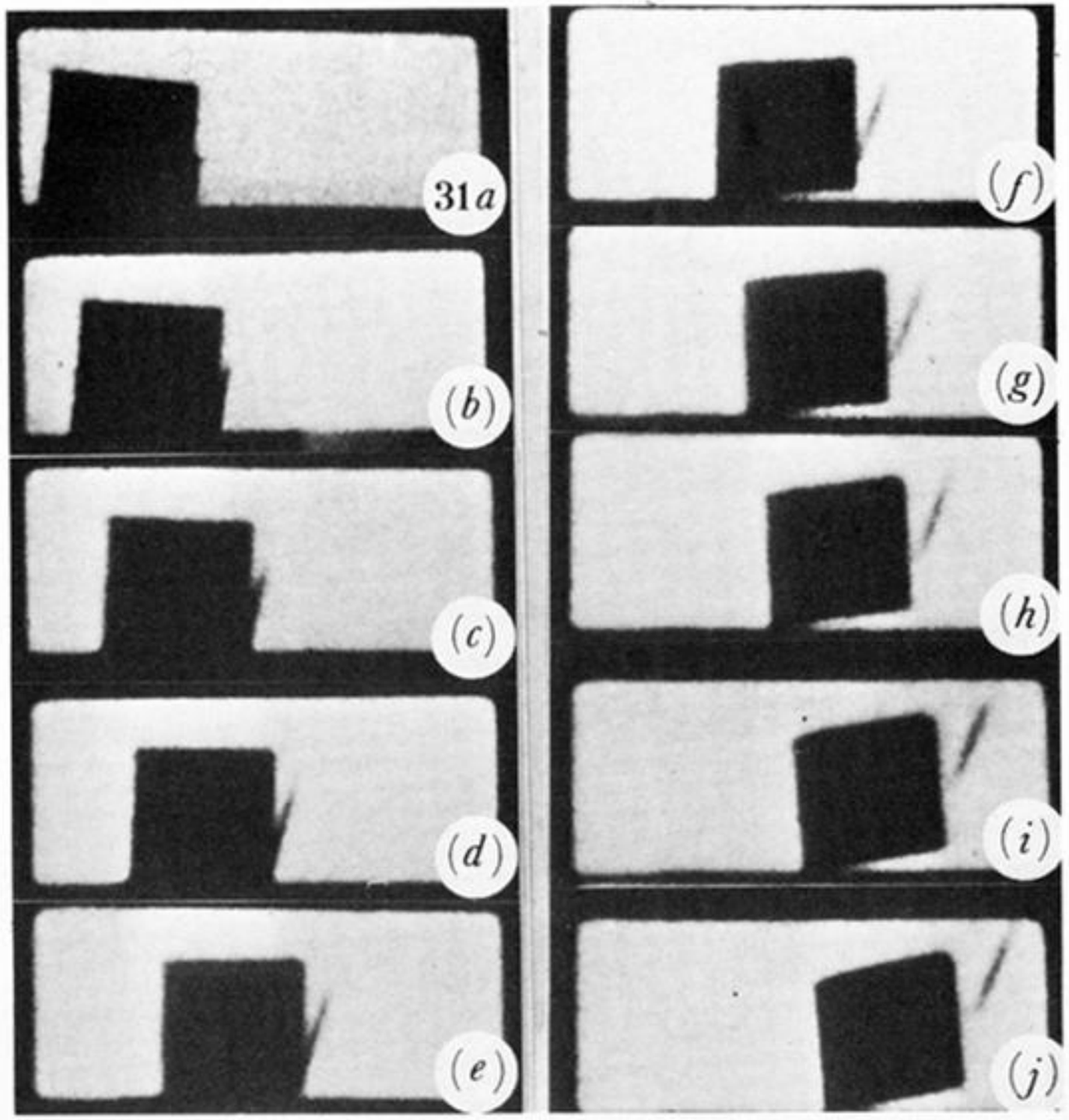

FIGURE 31. High-speed photographic sequence showing back rotation of an 8 mm-square steel plate and a chip of PE being cut off. Interframe time: 19 μs. $v_i = 89$ m s^{-1}, $\alpha = 10°$, $-\gamma = -8°$; $v_r = 72$ m s^{-1}, $\beta = 7°$, $\omega = -1.8$ krad s^{-1}.

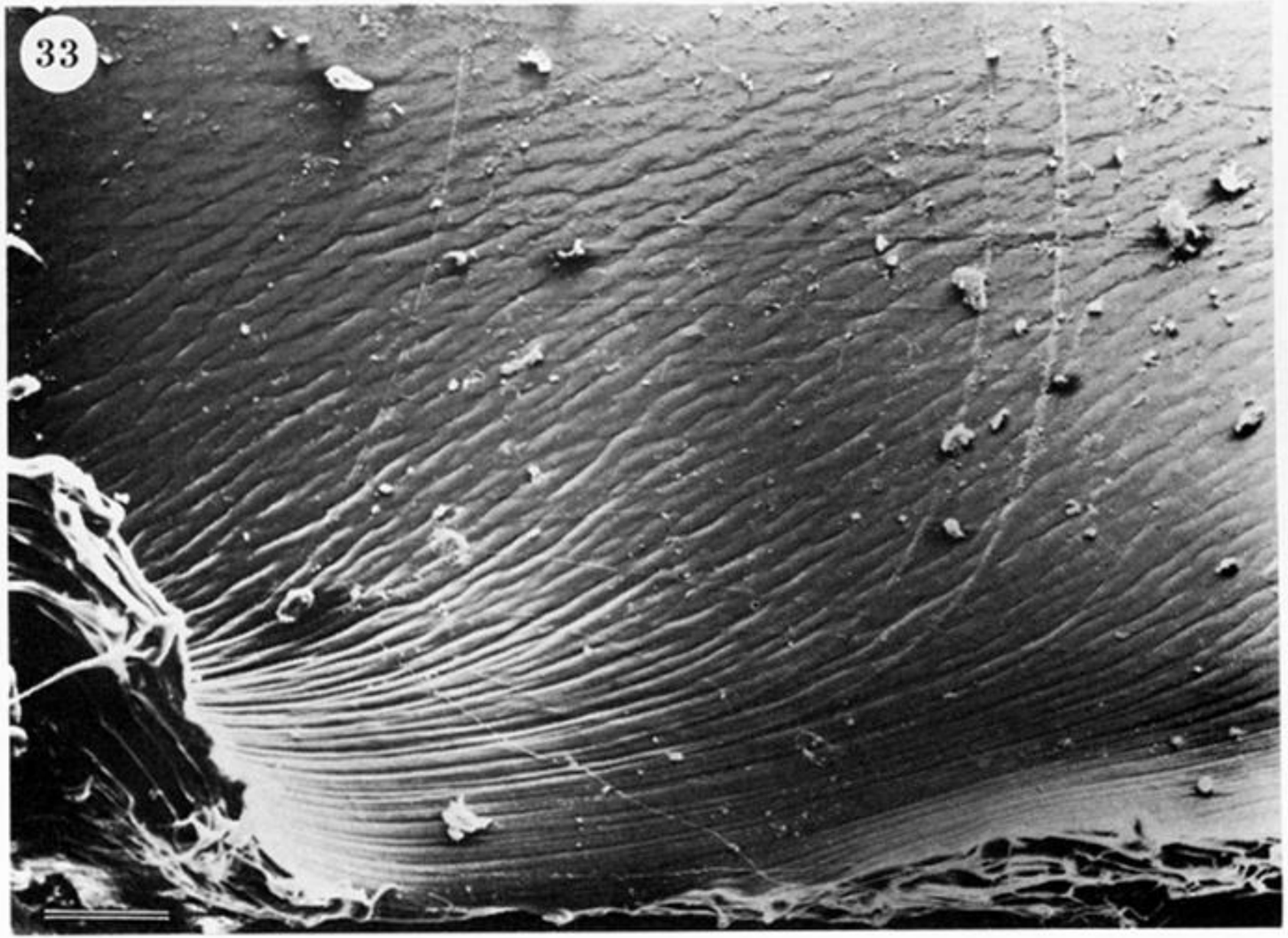

FIGURE 33. Electron micrograph of shear bands at the base of the lip of figure 32*b*. Scale bar represents 100 μm. Potential: 20 kV.

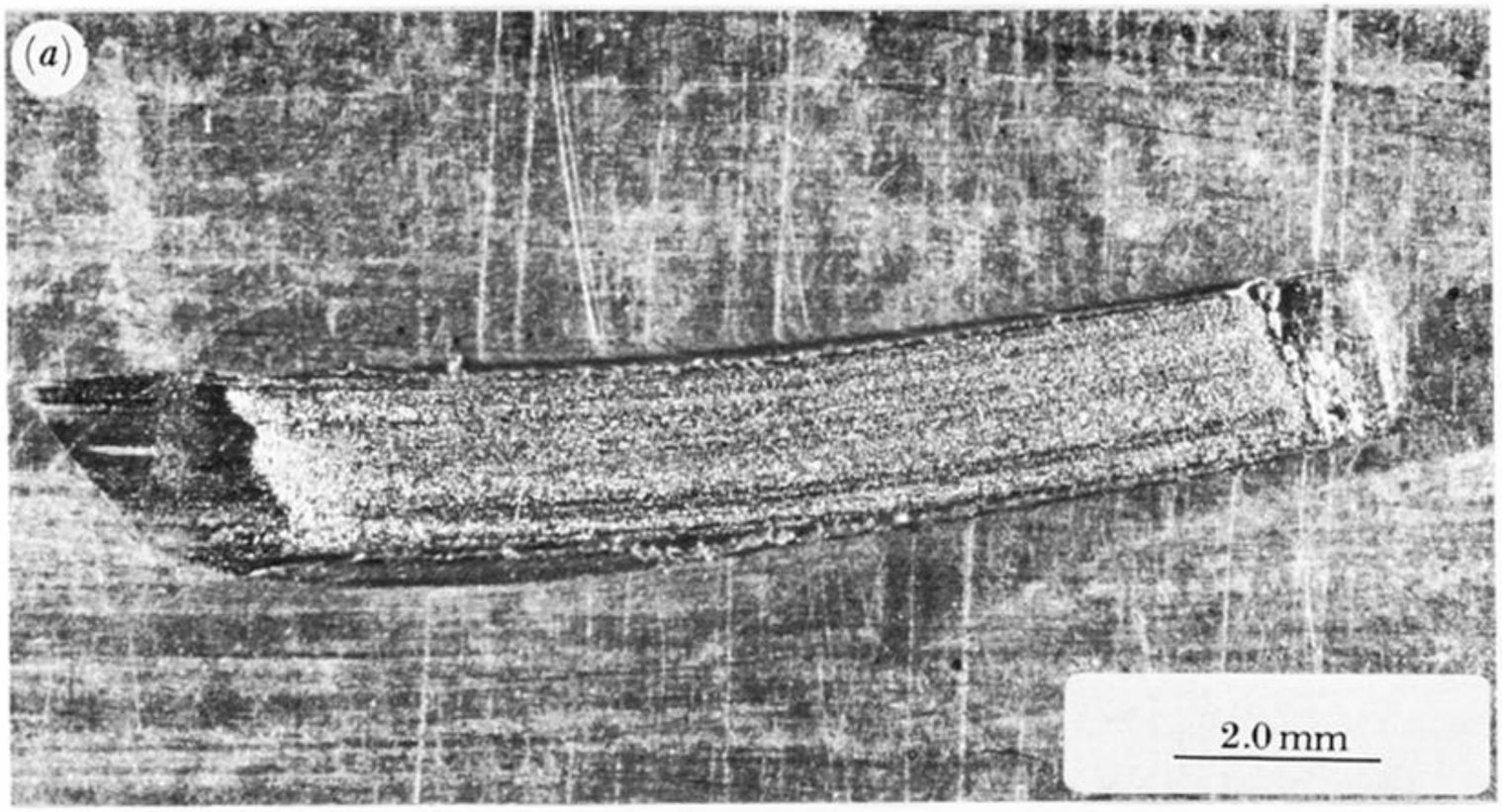
(a)
2.0 mm

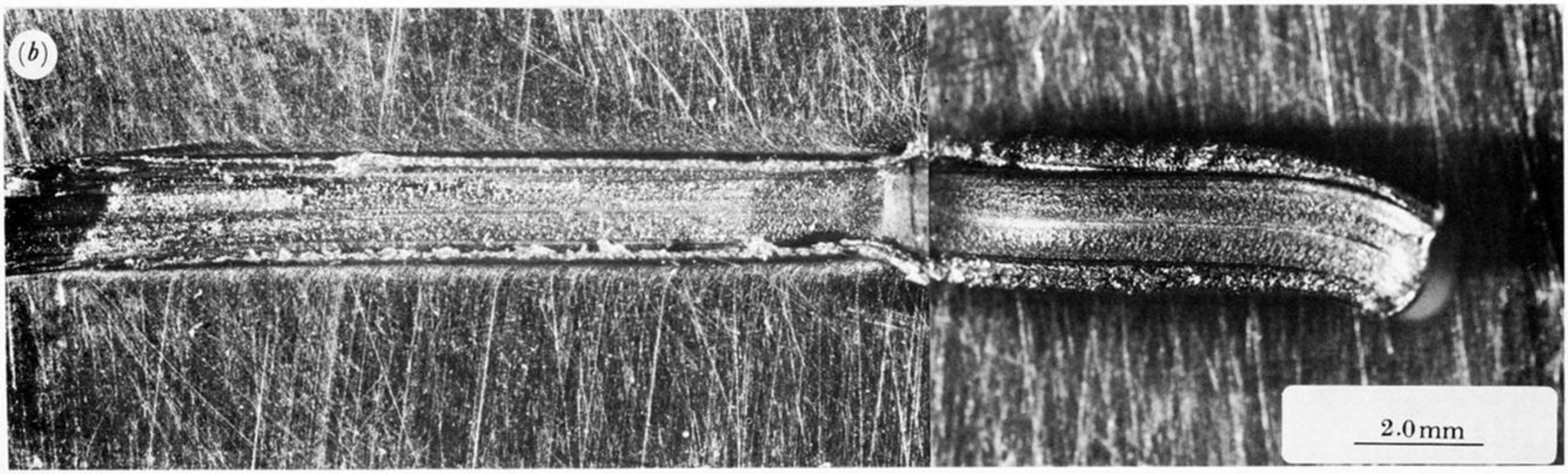
(b)
2.0 mm

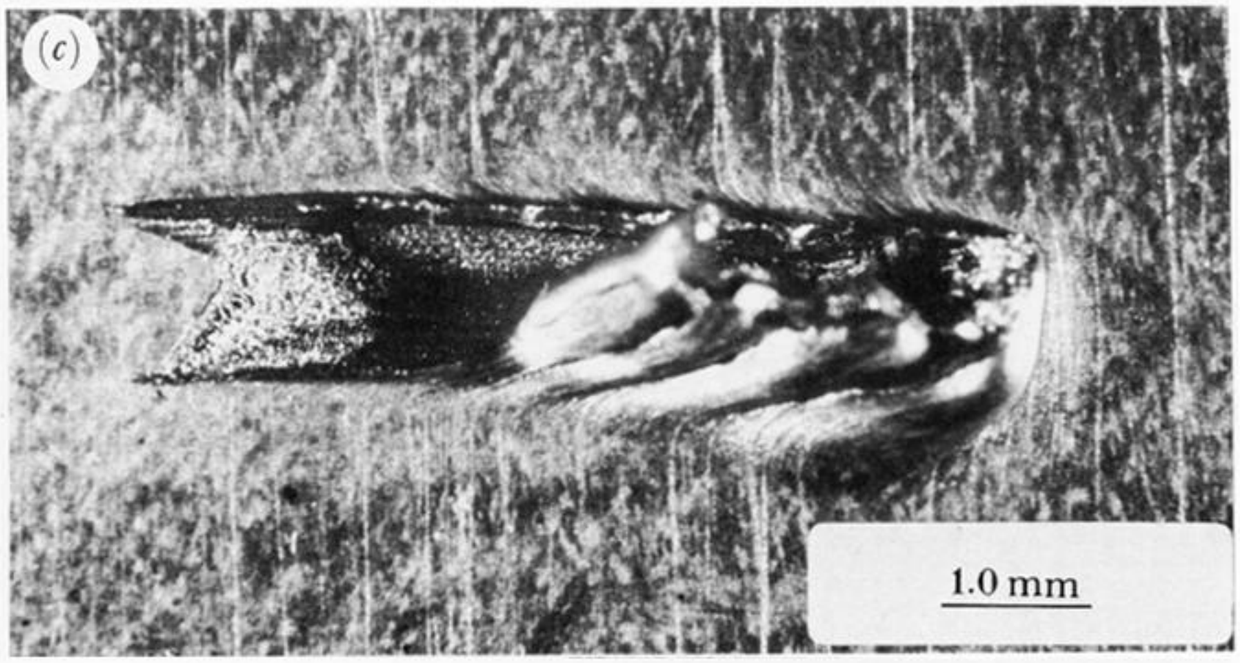
(c)
1.0 mm

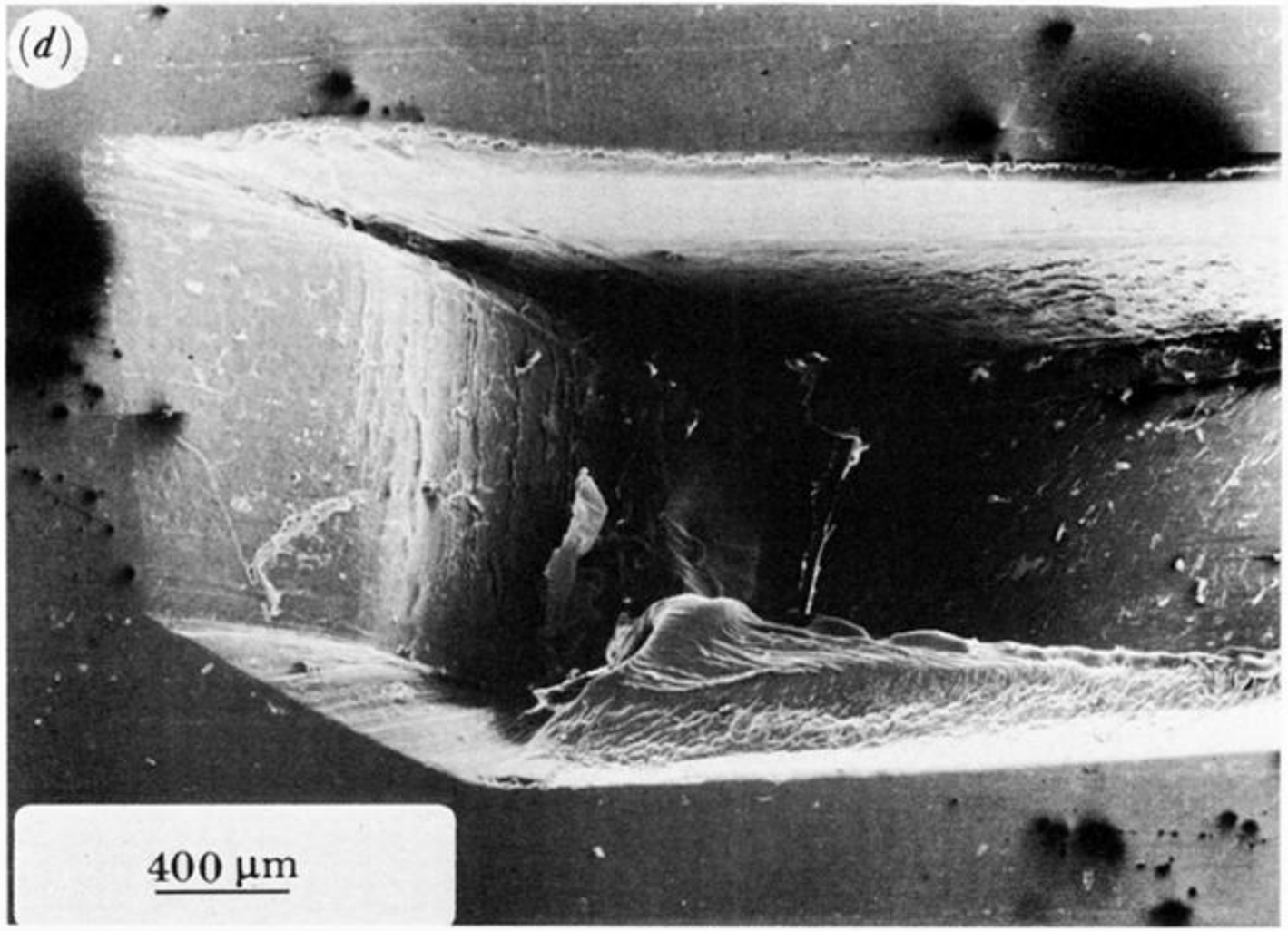

FIGURE 32. (*a*) Optical picture of the damage produced by the impact shown in figure 31. Plate moved from left to right. (*b*) Optical picture of an impact site where the plate rotated in a forwards sense; $v_i = 86$ m s^{-1}, $\alpha = 10°$, $-\gamma = -14°$. (*c*) Optical picture of a cutting-type crater. $v_i = 86$ m s^{-1}, $\alpha = 14°$, $-\gamma = -84°$; $v_r = 66$ m s^{-1}, $\beta = 14°$, $\omega = 2.3$ krad s^{-1}. (*d*) Scanning electron micrograph of a sharp dent. Potential: 20 kV. $v_i = 72$ m s^{-1}, $\alpha = 32°$, $-\gamma = -33°$; $v_r = 59$ m s^{-1}, $\beta = 21°$, $\omega = 6.4$ krad s^{-1}.